Final Draft
of the original manuscript:

Kannan, M.B.; Dietzel, W.; Blawert, C.; Atrens, A.; Lyon, P.:
Stress corrosion cracking of rare-earth-containing magnesium alloys ZE41, QE22 and Elektron 21 (EV31A) compared with AZ80
In: Materials Science and Engineering A (2007) Elsevier

DOI: 10.1016/j.msea.2007.07.070

Stress corrosion cracking of rare-earth-containing magnesium alloys ZE41, QE22, and Elektron 21 (EV31A) compared with AZ80

M. Bobby Kannan[a*], W. Dietzel[a], C. Blawert[a], A. Atrens[b], P. Lyon[c]

[a]*Institute for Materials Research, GKSS-Forschungszentrum Geesthacht GmbH, D-21502 Geesthacht, GERMANY*

[b]*Materials Engineering, University of Queensland, Brisbane Qld, 4072, AUSTRALIA*

[c]*Magnesium Elektron, Manchester M27 8DD, UK*

Abstract

Stress corrosion cracking (SCC) of the high-performance rare-earth containing magnesium alloys ZE41, QE22 and Elektron 21 (EV31A) was studied using slow strain rate tests (SSRT) in air, distilled water and 0.5 wt.% NaCl solution. For comparison, the well known AZ80 alloy was also studied. All the four alloys (AZ80, ZE41, QE22 and EV31A) were susceptible to SCC in 0.5wt.% NaCl solution and distilled water. AZ80 had similar SCC susceptibility in distilled water and 0.5 wt.% NaCl solution. ZE41, QE22 and EV31A had higher susceptibility to SCC in 0.5 wt.% NaCl solution than in distilled water. EV31A had the highest resistance to SCC compared to AZ80, ZE41 and QE22 in both distilled water and 0.5 wt.% NaCl solution. The fractography was consistent with (i) largely transganular SCC (TGSCC) in distilled water for AZ80, ZE41 and QE22 and also for AZ80 in 0.5 wt.% NaCl solution, and (ii) a significant component of intergranular SCC (IGSCC) in 0.5 wt.% NaCl solution for QE22, ZE41 and EV31A. The TGSCC fracture path in AZ80, ZE41 and QE22 is consistent with a mechanism involving hydrogen. In each case, the IGSCC appeared to be associated

* Corresponding author. Tel.: +49 4152 872557; fax: +49 4152 872625

E-mail address: mbobbykannan@yahoo.com (M. Bobby Kannan).

with the second phase particles along grain boundaries. For IGSCC of EV31A and QE22, the fractography was consistent with micro-galvanic acceleration of the corrosion of α-magnesium by the second phase particles, whereas it appeared that the second phase particles had corroded itself in the case of ZE41 in 0.5 wt.% NaCl solution. The study suggests that rare earth elements in magnesium alloys can improve SCC resistance significantly as observed in the case of EV31A. However, the SCC resistance also depends on the other critical alloying elements such as zinc (in ZE41) and silver (in QE22) and the microstructure.

Keywords: Magnesium alloy; Stress corrosion cracking; Rare earth elements

1. Introduction

In recent years, new magnesium alloys have been formulated incorporating rare earth (RE) elements to improve their characteristics for different applications [1-5]. Rare earth addition to magnesium alloys has a significant effect on the creep resistance, which is primarily attributed to the formation of rare earth containing phases along the grain boundary of the alloy [4,5]. Controlled addition of individual rare earth elements in magnesium alloys influence the castability and age hardening response [6].

This paragraph summarises the influence on mechanical properties of individual rare earth elements and combination with zinc and zirconium. Neodymium in dilute amounts in magnesium results in significant increase in hardness and strength after artificial aging [6]. The strengthening is primarily due to precipitates formed within the grains and at the grain boundaries. Neodymium also improves the castability of

magnesium alloys [6]. Magnesium-Gadolinium system is one of the most promising candidates due to the remarkable age-hardening response and very good thermal stability of main strengthening phase up to 250°C [7]. Recently, neodymium in a gadolinium containing magnesium alloy was reported to reduce the solid solubility of gadolinium by shifting the solvus towards lower gadolinium concentrations [8]. This is potentially attractive since this offers the possibility of improving the precipitation hardening response even at a lower concentration of gadolinium, which is expensive. Zinc is often incorporated in magnesium alloys in sufficient quantity to achieve precipitation hardening [6]. Zinc in neodymium and gadolinium containing magnesium alloys delay the onset of over aging of the alloy [9]. Zirconium in rare earth containing magnesium alloys has been shown to improve the mechanical properties due to grain refinement [10]. Drits et al. [11] reported that combined addition of zirconium and neodymium reduces their solid solubility lower than that of the individual solid solubility and thus improve the strength level of magnesium alloys. Good mechanical properties at ambient and also at elevated temperatures was reported for Mg-Nd-Zn-Zr alloy [12,13].

Despite their attractive mechanical properties, the use of magnesium alloys is not fully realized, mainly due to their poor corrosion resistance. Magnesium alloys are well known for their high susceptibility to general and localized corrosion such as pitting and stress corrosion cracking (SCC) [14-19]. A significant amount of work has been carried out to understand the general corrosion behavior of rare earth containing magnesium alloys. Nakatsugawa et al. [20] studied the corrosion behavior of a few rare earth containing magnesium alloys (e.g., WE series containing yttrium and rare earth; and AE series containing aluminium and rare earth) and found that rare earth elements

improve the corrosion resistance of magnesium alloys. Nordlien et al. [21] reported that the rare earth elements improve the passivation behavior of magnesium alloys. Based on the X-ray photo spectroscopy (XPS) analysis of the corrosion product formed in rare earth containing magnesium alloys, Kiryuu [22] suggested that the corrosion product is stabilized by the rare earth elements. Chang et al. [23] reported that neodymium containing magnesium alloy (Mg-3Nd-0.2Zn-0.4Zr) exhibits higher corrosion resistance than the commercial AZ91D alloy. Krishnamurthy et al. [24] suggested that the pseudopassivation in the rapidly solidified Mg-Nd alloys is due to neodymium enrichment at the surface. Lyon et al. [6] reported that gadolinium has a much lower effect upon corrosion than zinc. They further reported that alloys with good corrosion performance were possible by controlling the zinc concentration within the range of 0.2-0.55 % and the gadolinium concentration to less than 1.75 %. Zirconium has a beneficial effect on the corrosion resistance since zirconium co-precipitates with several impurity elements including iron and effectively sinks these particles to the bottom of the melting crucible during melting [10, 23].

A comprehensive critical review on the SCC behavior of magnesium alloys has been carried out by Winzer et al. [17]. In that review, they report that all magnesium alloys are susceptible to SCC to some extent. The SCC susceptibility in magnesium alloys is attributed to two types of mechanisms: (i) anodic dissolution (continuous crack propagation by anodic dissolution at the crack tip, film rupture and tunnelling), and (ii) hydrogen embrittlement (discontinuous crack propagation by a series of mechanical fractures at the crack tip). The AZ series of magnesium alloys containing both aluminium and zinc is considered particularly susceptible in atmosphere and in chloride-containing solution [25]. The SCC susceptibility is reported to increase with

aluminium content with maximum susceptibility occurring at 6% [26]. Other reports state that SCC susceptibility does not vary for aluminium contents between 4% and 9% [27]. Relatively recent work by Miller [28] clearly showed that the most popular alloys, AZ91, AM60 and AS41, were susceptible to SCC in distilled water. Fairman and Bray [29] stated that, although Fe contributes to general corrosion, it has minimal effect on SCC. In contrast, Perryman [30] reported that for Mg-5Al with 0.013% and 0.0019% Fe content, the alloy with the higher iron content was more susceptible to SCC in distilled water.

Literature on the SCC behavior of rare earth containing magnesium alloys is limited. However, even the available literature reports contradictory views. The Winzer et al. [17] review of the SCC behavior of magnesium alloys shows that elements such as neodymium, silver, zirconium, lithium, lead, copper, nickel, tin and thorium had little or no influence on SCC susceptibility. In contrast, Rokhlin [1] reported that neodymium or cadmium addition to Mg-Zn-Zr alloy increased the SCC resistance. In contrast, the ASM Handbook stated that magnesium alloys containing zirconium and other rare earths can have intermediate susceptibility in atmospheric environments [27].

The objective of this work is to characterise the SCC behavior of three high performance rare earth containing magnesium alloys i.e.ZE41, QE22 and Elektron 21 (EV31A). For comparison, the well known AZ80 alloy was also studied. Slow strain rate test (SSRT) method was used for this study.

2. Experimental procedure

The chemical composition of the four magnesium alloys is presented in Table 1 and their thermo-mechanical treatments are given in Table 2. EV31A is the ASTM

designation of the alloy Elektron 21. For microstructural examination using optical microscopy, specimens were prepared by standard metallographic procedures and were etched in a solution containing 3.5 g picric acid, 6.5ml acetic acid, 20ml water and 100ml ethanol. Energy dispersive X-ray (EDX) analysis was carried out for the characterisation of the secondary phase particles.

The SCC susceptibility was studied using slow strain rate test (SSRT) method. Round tensile specimens with gauge dimensions 22 mm (length) x 5 mm (diameter) were used. The tensile samples were ground with SiC paper up to 1200 grit and cleaned with acetone prior to testing. In the SSRT experiments, the tensile samples were tested at two strain rates 10^{-6}/s and 10^{-7}/s in air, or exposed to distilled water or 0.5 wt.% NaCl solution. For comparison, the mechanical properties were measured in air at a strain rate of 10^{-4}/s in a universal testing machine.

The SSRT machine (Fig.1) maintained a constant strain rate by means of an open-loop control system; the average specimen elongation was measured by two linear variable displacement transducers (LVDTs) attached at two opposite sides of the specimen fixtures in parallel with the specimen whilst a geared synchronous motor increased the elongation and thus the load accordingly. The schematic diagram of the SSRT machine is shown in Fig. 1. All values of strain rate given in this paper are nominal ones, based on the elongation measured by a pair of LVDTs. These measurements were used to control, in a feed-back circuit, the crosshead speed of the test machine, to achieve a constant rate of increase in displacement. Here, a uniform deformation over the entire gauge section of the specimen was assumed. The actual strain and hence the actual strain rate at the site of failure, caused by either mechanical rupture or by SCC, could not be measured with the equipment used.

The SCC susceptibility was evaluated using the parameters elongation to failure (ε_f) and ultimate tensile stress (UTS) both measured in an inert atmosphere (air) and in the corrosive environments (distilled water and 0.5 wt. % NaCl solution). After the SSR tests, the fracture surfaces were examined using a scanning electron microscope (SEM).

3. Results

3.1 Microstructure

Fig. 2 a-d shows the optical microstructure of AZ80, ZE41, QE22 and EV31A. The micrograph of AZ80 shows α phase magnesium matrix with clusters of second phase particles particularly at the grain boundaries (Fig.2a). EDX analysis revealed that these are rich in magnesium and aluminium, which corresponds to $Mg_{17}Al_{12}$. Also some aluminium and manganese rich particles were observed, which corresponds to Al_8Mn_5 [31]. The micrograph of ZE41 shows second phase particles along the grain boundaries of the alloy (Fig.2b); in some regions there appears to be a continuous network of the second phase particles along the grain boundary. EDX analysis revealed that these particles are rich in magnesium and zinc with trace amount of rare earths. The micrograph of QE22 shows second phase particles decorated along the grain boundaries and precipitates inside the grain (Fig.2c). EDX analysis further revealed that the grain boundary particles are rich in magnesium, neodymium and silver, whereas the intragranular particles are rich in magnesium and zirconium. In a similar QE22 alloy, Lambri et al.[32] identified coherent hexagonal (Mg-Nd-Ag) and tetragonal (Mg-Nd) precipitates. The micrograph of EV31A shows a high density of fine second phase particles distributed inside the grains in addition to the few coarse precipitates in the grain boundaries (Fig. 2d). Here, the EDX analysis revealed that the grain boundary

particles are rich in magnesium, neodymium and zinc. Apps et al. [33] reported precipitates having a stoichiometric ratio of $Mg_5(Nd_{0.5}Gd_{0.5})$ in magnesium alloys containing neodymium and gadolinium (Mg- 7%Gd-2.25%Nd-0.6%Zr). Dirts et al.[11] suggested binary phases Mg_9Nd, Mg_7Zn_3, MgZn and ternary phases $MgNd_4Zn_5$, $Mg_6Nd_2Zn_7$, $Mg_2Nd_2Zn_9$ in Mg-Zn-Nd alloys containing up to 8 wt.% Zn and 3 wt.% Nd. The fine clusters of particles in the grain (Fig.2d) were found to be rich in magnesium, zinc and zirconium. Ben-Hamu et al. [10] also reported zirconium-rich fine cluster of intergranular particles in Mg-Y-RE-Zr alloy. These authors further reported that the cluster of precipitates does not contain rare earth (neodymium), and expected that these zirconium rich clusters could improve the strength of the alloy by dislocation-obstacle interaction mechanism, although the precipitates visible in Fig. 2d are probably too coarse to affect dislocation interaction.

3.2 Slow strain rate testing

The stress-strain curves of AZ80, ZE41, QE22 and EV31A tested in air, and the apparent stress-strain curves in distilled water and in 0.5 wt.% NaCl solution at two strain rates i.e. 10^{-6}/s and 10^{-7}/s are presented in Fig. 3a- d. Mechanical property data of the four alloys in air are presented in Table 3, which includes comparison data in air at a strain rate of 10^{-4}/s and literature data. The summary of SSRT data of the four alloys tested in air, distilled water and in 0.5 wt.% NaCl solution is shown in Table 4. The mechanical property values reported herein from this study are an average of three test results.

The mechanical property values measured in this study at a strain rate of 10^{-4} /s in air are consistent with the literature data. However the strain to fracture values in air

measured at a strain rate of 10^{-6} /s were significantly higher than those measured in air at a strain state of 10^{-4} /s {i.e. $\varepsilon_f(10^{-6}) > \varepsilon_f(10^{-4})$} for AZ80 and QE22, whereas $\varepsilon_f(10^{-6}) \sim \varepsilon_f(10^{-4})$ for ZE41 and EV31A. This shows the strain rate sensitivity of the alloys.

AZ80 tested at a strain rate of 10^{-6}/s in air exhibited a strain to failure, ε_f, of 19 % and UTS of 350 MPa. At the same strain rate in distilled water, AZ80 showed significantly lower mechanical property values: ε_f = 11 % and UTS = 320 MPa. The mechanical properties were lower when tested in 0.5 wt.% NaCl solution: ε_f = 7 % and UTS = 290 MPa. The mechanical properties were even lower when tested at a lower strain rate ie. 10^{-7}/s: ε_f = 2 % and UTS = 230 MPa in distilled water and ε_f = 2 % and UTS = 220 MPa when tested in 0.5 wt.% NaCl solution (Fig.3a, Table 4).

ZE41 when tested at a strain rate of 10^{-6}/s in air exhibited ε_f = 9 % and UTS = 200 MPa (Fig.3b). At this strain rate, the tests in distilled water showed a slight decrease in the mechanical properties: ε_f = 8 % and UTS = 190 MPa. However, in 0.5 wt.% NaCl solution the mechanical properties were significantly lower: ε_f = 3 % and UTS = 160 MPa. The mechanical properties were the lowest when tested at a strain rate of 10^{-7}/s: ε_f = 5 % and UTS = 160 MPa in distilled water and ε_f = 2 % and UTS = 130 MPa when tested in 0.5 wt.% NaCl solution (Fig.3b, Table 4).

QE22 when tested at a strain rate of 10^{-6}/s in air showed ε_f = 23 % and UTS = 230 MPa (Fig.3c). At the same strain rate, the tests in distilled water showed a significantly lower value of ductility with a small loss in strength: ε_f = 12 % and UTS = 230 MPa. Lower values were measured in 0.5 wt.% NaCl solution: ε_f = 3 % and UTS = 190 MPa. At the lower strain rate of 10^{-7}/s: ε_f = 6 % and UTS = 200 MPa in distilled water; ε_f = 1 % and UTS = 150 MPa when tested in 0.5 wt.% NaCl solution were

observed (Fig.3c). The mechanical property values in 0.5 wt.% NaCl solution were significantly lower than in distilled water (Fig. 3c, Table 4).

EV31A when tested at a strain rate of 10^{-6}/s in air showed ε_f = 6 % and UTS = 270 MPa (Fig.3d). At the same strain rate, the tests in distilled water showed similar values of ductility and strength: ε_f = 6 % and UTS = 250 MPa; whereas the values were somewhat lower in the 0.5 wt.% NaCl solution: ε_f = 4 % and UTS = 230 MPa. At the lower strain rate of 10^{-7}/s, the mechanical properties were similar: ε_f = 6 % and UTS = 240 MPa in distilled water and ε_f = 4 % and UTS = 230 MPa in 0.5 wt.% NaCl solution (Fig. 3d, Table 4).

3.3 Macrographs

The macrographs of typical SSRT samples of all the four alloys after tests in distilled water and in 0.5 wt.% NaCl solution are shown in Fig. 4a-h. In distilled water, AZ80 did not undergo much corrosion; however there were many fine stress corrosion cracks throughout the gauge length (Fig.4a). In the 0.5 wt.% NaCl solution, the amount of corrosion was slightly higher than in distilled water (Fig.4b). The stress corrosion crack propagated along the fine streaks of second phase particles. ZE41 showed significant localized corrosion after the SSRT in 0.5 wt.% NaCl solution, significantly more than after the SSRT in distilled water (Fig.4 c, d). QE22 turned black in colour when tested in distilled water, with a high fraction of general corrosion (Fig.4e). In the 0.5 wt.% NaCl solution, QE22 exhibited significant localized corrosion and general corrosion (Fig.4f). EV31A showed relatively low uniform corrosion in distilled water, however no localized corrosion was observed. (Fig.4g). Similarly, in the 0.5 wt.% NaCl solution, EV31A showed uniform corrosion but no localized attack (Fig.4h).

3.4 Fractography

Typical fracture surfaces of AZ80 after SSRT in air at strain rate of 10^{-6}/s, in distilled water and in 0.5wt.% NaCl solution at a strain rate of 10^{-7}/s are shown in Figs. 5-7. Fig.5a shows an overview of the fracture surface of AZ80 after SSRT in air. Higher magnification shows that the fracture was ductile in nature i.e. dimple rupture due to micro-void coalescence occurred (Fig.5b). Some localized areas showed a brittle appearance; these areas might correspond to fracture associated with β-phase particles. Fig.6a shows an overview of the fracture surface of AZ80 after SSRT in distilled water. The fracture was quite flat over most of the area and there was some shallow cracking at the edge of the sample. Higher magnification of the edge of the fracture surface revealed that the cracking was predominantly transgranular (Fig.6b) with some localized secondary cracking (Fig.6c). However in the centre of the fracture surface the fracture mode was ductile tearing (Fig.6d). Fig.7a shows an overview of the fracture surface of AZ80 after SSRT in 0.5 wt. % NaCl solution. There was random localized attack on the fracture surface. Higher magnification of the circumferential edge of the fracture surface showed significant localized corrosion (Fig.7b). The edge of the fracture surface showed a combined process of brittle fracture, corrosion and dimple rupture (Fig.7c). Similar features were observed in the centre of the fracture surface (Fig.7d). No evidence of corrosion associated with the grain boundaries was found.

Typical fracture surfaces of ZE41 after SSRT in air at a strain rate of 10^{-6}/s, in distilled water and in 0.5wt.% NaCl solution at a strain rate of 10^{-7}/s are shown in Figs. 8-10. Fig. 8a shows an overview of the fracture surface of ZE41 after SSRT in air. Higher magnification showed that the fracture mode was predominantly dimple rupture along the grain boundaries with some fracture across the grains (Figs. 8b,c). In both

fracture modes there was considerable brittle fracture associated with the second phase particles. The fracture surface of ZE41 after SSRT in distilled water showed a generally smooth and undulated appearance, consistent with corrosion along the grain boundaries accelerated by micro-galvanic corrosion of second phase particles that formed a nearly continuous necklace along the grain boundaries (Fig. 9a- c). The grain boundary surfaces themselves appeared predominantly as if they had been chemically polished. There were isolated incidences of grain boundary attack into the plane of the fracture. An overview of the fracture surface of ZE41 after SSRT in 0.5 wt.% NaCl solution showed predominant brittle failure can be seen from Fig. 10a. Higher magnification showed that the fracture surface was consistent with dissolution of the grain boundary precipitates (Fig. 10b,c,d). There were only a few remnants remaining of the second phase particles remaining that were so evident on the fracture surface after SSRT in distilled water (Fig. 9b). The grain boundary surfaces appeared etched. There were also some isolated areas that could be consistent with transgranular brittle fracture (Fig. 10c).

Typical fracture surfaces of QE22 after SSRT in air at a strain rate of 10^{-6}/s, in distilled water and in 0.5wt.% NaCl solution at a strain rate of 10^{-7}/s are shown in Figs. 11-13. Fig.11a depicts an overview of the fracture surface of QE22 after SSRT in air. Higher magnification showed that the fracture surface was consistent with a mixed-mode fracture having features associated with both dimple rupture and brittle fracture (Fig. 11b, c). It is expected that the brittle fracture features were associated with the second phase particles. QE22 after SSRT in distilled water showed a mixed mode of fracture (Fig 12a-d). The edge of the fracture surface showed some typical transgranular cleavage (Fig. 12b) and in other areas showed mixed transgranular and intergranular

fracture (Fig. 12c). Some intergranular cracking was also observed in the centre of the fracture surface (Fig. 12d). The fracture of QE22 after SSRT in 0.5 wt.% NaCl solution showed a high surface coverage of corrosion product (Fig. 13a). Nevertheless, it was evident that there had been significant corrosion along grain boundaries (Fig. 13b). There were features consistent with corrosion of α phase leaving behind the second phase particles (Fig.13c). Other features were consistent with fracture of the second phase particles (Fig.13d). The fractography was consistent with a mixed intergranular and transgranular mode with intergranular failure being predominant. The α-phase that was visible had an appearance consistent with having been corroded.

Typical fracture surfaces of EV31A after SSRT test in air at a strain rate of 10^{-6}/s, in distilled water and in 0.5wt.% NaCl solution at a strain rate of 10^{-7}/s are shown in Fig 14-16. Fig.14a shows an overview of the fracture surface of EV31A alloy after SSRT in air. Higher magnification showed a jumbled transgranular fracture surface containing (i) flat facets that may be associated with brittle fracture of a second phase particles, (ii) areas of dimple rupture and (iii) flat areas with some evidence of ductility (Fig.14b). The fracture surface of EV31A after SSRT in distilled water, showed similar fracture features containing ductile features as well as transgranular cracking (Fig. 15a-d). For EV31A after SSRT in 0.5 wt.% NaCl solution, the fracture mode was of mixed intergranular and transgranular nature (Fig. 16a-d). Fig. 16c shows clearly the intergranular nature of the fracture. Many features were consistent with the appearance of corrosion along grain boundaries. Other features were consistent with the corrosion of the grain on both sides of second phase particles extending a considerable distance along several grain boundaries, also with features consistent with the brittle fracture of this second phase particles. Considerable corrosion was observed on most of the

surfaces that appear consistent with grain surfaces, in some cases the appearance was consistent with a transgranular cracking (Fig.16d).

4. Discussion

In order to quantify the SCC susceptibility of the alloys, the SCC susceptibility indices (I_{SCC}) were calculated based on a particular mechanical property value measured in an SSRT test in corrosive environment compared to its corresponding value in an inert environment. Here, distilled water and 0.5 wt% NaCl solution were considered as the corrosive and air as the inert environment. In order to quantify the chloride induced SCC, the ratio between the mechanical properties in 0.5 wt.% NaCl solution / distilled water was calculated. A low I_{SCC} index corresponds to high SCC susceptibility, and when the I_{SCC} index approaches unity this means that there is no effect due to the test environment or in other words the alloy is highly resistant to SCC in the particular test environment.

The SCC susceptibility indices for AZ80, ZE41, QE22 and EV31A are presented in Tables 5 and 6. At a strain rate of 10^{-6}/s, AZ80 and QE22 showed higher SCC susceptibility in distilled water than for ZE41 and EV31A. In 0.5wt. % NaCl solution, the SCC susceptibility further increased for AZ80 and QE22; the SCC susceptibility for QE22 was higher than that of AZ80; ZE41 showed an SCC susceptibility similar to that of AZ80; and EV31A exhibited I_{SCC} indices of 0.7 for ε_f and 0.85 for UTS, showing an SCC resistance higher than AZ80, ZE41 and QE22. The I_{SCC} (0.5 wt.% NaCl/ distilled water) showed that the chloride induced SCC was high in QE22 and relatively low for EV31A.

At a strain rate of 10^{-7}/s in distilled water the SCC susceptibility was much higher for AZ80, ZE41 and QE22 (Table 6). Similar to the SCC susceptibility at a strain rate of 10^{-6}/s, AZ80 and QE22 showed higher SCC susceptibility than ZE41 and EV31A. In the 0.5 wt. % NaCl solution, the SCC susceptibility indices were low (~ 0.1) for AZ80, ZE41 and QE22 corresponding to the high SCC susceptibilities of these alloys. In contrast, EV31A showed a higher SCC resistance than that of AZ80, ZE41 and QE22. For the chloride induced SCC, the effect was much higher in QE22 and ZE41 than in AZ80 and EV31A.

At a strain rate of 10^{-6}/s the SCC index related to ductility gave significantly lower values than the index related to strength. This indicates that the index related to ductility provides a more sensitive indication of the SCC susceptibility. At the lower strain rate of 10^{-7}/s the loss in strength was also significant for AZ80, ZE41 and QE22 showing high a SCC susceptibility. This shows that a strain rate of 10^{-7}/s is more sensitive in determining the SCC susceptibility of magnesium alloys.

Assuming, that Iscc(distilled water/air) corresponds to hydrogen embrittlement of the alloy and that Iscc(0.5wt.% NaCl solution/distilled water) corresponds to chloride induced SCC, the following points can be made. QE22 shows similar hydrogen embrittlement susceptibility as that of AZ80. On the other hand, EV31A shows the least hydrogen embrittlement susceptibility, followed by ZE41. The chloride induced SCC was much higher for QE22 and for ZE41 than for AZ80. EV31A also showed slightly higher chloride induced SCC than AZ80. However, the overall SCC susceptibility was much lower for EV31A than for AZ80, ZE41 and QE22.

The micrographs of the failed tensile samples show that QE22 and ZE41 have undergone more corrosion than AZ80. EV31A showed the highest resistance to corrosion of all four alloys. In AZ80, the corrosion was preferentially along the streak of β-precipitates and was much more prominent in the chloride containing solution. The corrosion along the precipitates could be expected because these precipitates are reported to be noble compared to that of the magnesium matrix [31]. The volta potential of β precipitates ($Mg_{17}Al_{12}$) was reported to be 152mV positive than the matrix [31]. In ZE41, the corrosion attack is higher than that of AZ80. Even though zirconium is present in ZE41, which is reported to be beneficial for corrosion resistance by reducing the iron content [10, 23], the zinc content (has negative effect on magnesium corrosion) [27] is quite high resulting in high corrosion. Moreover, it should be noted that the presences of rare earth elements has not improved the corrosion resistance of ZE41, even though it is often reported that rare earth addition to magnesium improves the corrosion resistance [20-24]. In QE22 alloy, even though neodymium is present which is reported to increase the corrosion resistance of the alloy [23, 34], the presence of silver had a very significant effect in promoting towards galvanic corrosion. Silver has a very high noble potential compared to magnesium [35] and hence can form micro-galvanic cells for the high corrosion attack. The corrosion attack was evident even in distilled water and was high in the chloride containing solution. In EV31A, the corrosion attack was minimum, probably the mixed oxide of the rare earth elements have protected the alloy surface from any corrosion attack. Ben-Hamu et al. [10] reported that the oxide film (Mg-Me-O where Me is zirconium and neodymium) is more stable than the $Mg(OH)_2$ that magnesium produces in aqueous solution.

The fracture modes of all the four alloys tested in distilled water and 0.5 wt.% NaCl solution are given in Table 7. In distilled water, AZ80 failed in TGSCC mode; a considerable amount of IGSCC was observed in ZE41 and QE22; EV31A revealed predominantly ductile features with some evidence of transgranular cracks. In 0.5 wt.% NaCl solution, AZ80 predominantly failed in TGSCC mode; ZE41, QE22 and EV31A showed a mixed mode of failure i.e. IGSCC and TGSCC. Many authors have stated that magnesium and its alloys mostly undergo TGSCC. Others claim that IGSCC is dominant for certain conditions. In this study, it is seen that the fine grained AZ80 underwent TGSCC and the relatively larger grains in ZE41, QE22 and EV31A underwent mixed-mode failure i.e. IGSCC and TGSCC. This is in agreement with Stampella et al. [36] who reported that the crack morphology was determined by the grain size and that for fine grained magnesium SCC was exclusively transgranular (TG) whereas for larger grained magnesium SCC was mixed TG and intergranular (IG). It is suggested that the continuous grain boundary precipitates observed in some part of the microstructure in the rare earth containing alloys (i.e., ZE41, QE22 and EV31A) would have accelerated the electrochemical corrosion along the grain boundaries causing IGSCC. Pardue et al. [37] also suggested that IGSCC is continuous and completely electrochemical and that TGSCC is discontinuous and involves alternating mechanical and electrochemical process. In fact, TGSCC is mostly related to hydrogen induced cracking [38, 39]. Stampella et al. [36] suggested that atomic hydrogen in solid solution of magnesium facilitates cleavage fracture. Based on the fracture surface analysis in this study, it is suggested that the TGSCC fracture path observed in AZ80, ZE41, and QE22 in distilled water is consistent with a mechanism involving hydrogen. In each case, the IGSCC appeared in chloride containing solution to be associated with corrosion induced

by the second phase particles along grain boundaries. For IGSCC of EV31A and QE22 the fractography was consistent with micro-galvanic acceleration of the corrosion of α-magnesium by the second phase particles whereas it appeared that the second phase particles had themselves corroded in the case of ZE41 in chloride containing solution.

The study suggests that rare earth elements in magnesium alloys can improve the SCC resistance significantly as observed in the case of EV31A. However, the SCC resistance also depends on the other critical alloying elements. For example, in the case of ZE41 and QE22, the presence of zinc and silver in considerable amount made these alloys less corrosion resistant and more susceptible to SCC even though they contained significant amounts of rare earth elements. Positive effects of rare earth elements are expected if the passive film formation and density is enhanced.

5. Conclusions

The SCC tendency of the four magnesium alloys under test can be summarised as follows, based on the SSRT in distilled water and in 0.5 wt. % NaCl solution:

- Each alloy (AZ80, ZE41, QE22 and EV31A) was susceptible to SCC in 0.5 wt.% NaCl solution and in distilled water.
- AZ80 had similar susceptibility in distilled water and in 0.5 wt.% NaCl solution.
- ZE41, QE22 and EV31A had a higher SCC susceptibility in 0.5 wt.% NaCl solution than in distilled water
- Tests at a lower stain rate (10^{-7}/s) indicated greater SCC susceptibilities of the alloys and greater difference in SCC susceptibilities between the alloys.

- EV31A had the highest resistance to SCC in both distilled water and 0.5 wt.% NaCl solution.
- The transganular SCC (TGSCC) fracture in AZ80, ZE41, QE22 in distilled water and in AZ80 in 0.5 wt.% NaCl solution was consistent with a mechanism involving hydrogen.
- The intergranular SCC (IGSCC) in ZE41, QE22 and EV31A in 0.5 wt.% NaCl solution was associated with the second phase particles along grain boundaries.
- Rare earth elements can improve the SCC resistance of magnesium alloy e.g. EV31A; however significant concentration of zinc (e.g. ZE41) and silver (e.g. QE22) reduces the SCC resistance.

Acknowledgements

The authors gratefully acknowledge the technical support extended by Mr. V. Heitman and Mr. V. Kree during the course of this work. One of the authors (MBK) expresses his sincere thanks for the financial support through the German Helmholtz-DAAD Postdoctoral programme.

References

[1] L.L. Rokhlin, in: Taylor and Francis (Eds.), Magnesium Alloys Containing Rare Earth Metals, London, 2003.

[2] I. Anthony, S. Kamado, Y. Kojima, Mater. Trans. 42 (2001) 1206.

[3] Q. Li, Q. Wang, Y. Wang, X. Zeng, W. Ding, J. Alloys Compds. 427 (2007) 115.

[4] J. F. Nie, X. Gao, S.M. Zhu, Scripta Mater. 53 (2005) 1049.

[5] C. Sanchez, C. Nussbaum, P. Azavant, H. Octor, Mater. Sci. Eng. A 221(1996) 48.

[6] P. Lyon, T.Wilks, I. Syed, in: N.R. Neelameggham, H.I. Kaplan, B.R. Powell (Eds.), The Influence of Alloying Elements and Heat Treatment Upon the Properties of Elektron 21 (EV31A) alloy, Magnesium Technology 2005, Warrendale, PA, 2005, 303.

[7] P. Vostry, B. Smola, I. Stulikova, F. von Buch, B.L. Mordike, Phys. Status Solidi A 175 (1999) 491.

[8] Y. Negishi, T. Nishimura, M.Kiryuu, S. Kamado, Y.Kojima, R. Ninomiya, J Japan Inst. Light Metals, 45 (1995) 57.

[9] L. Gill, G.W. Lorimer, P. Lyon, Microstructure and Property Relationships of Mg-RE-Zn-Zr Alloys, DGM International Conference on Magnesium Alloys and their Applications, Germany, 2003.

[10] G. Ben-Hamu, d. Eliezer, K.S.Shin, S. Cohen, J. Alloys Compds. (2006), doi:10.1016/j.jallcom.2006.05.075.

[11] M.E. Drits, E.M.Padezhnova, L.S. Guzei, Russ Metall. 1 (1978) 195.

[12] D. Thomas-Whittington, V. Srivastava, G.W. Greenwood, H. Jones, Z. Metallkd. 97 (2006) 156.

[13] R. Wilson, C.J. Bettles, B.C. Muddle, J.F. Nie, Mater. Sci. Forum 419-422 (2003) 267.

[14] G.L. Song, A. Atrens, Adv. Eng. Mater. 1 (1999) 11.

[15] G.L. Song, A. Atrens, Adv. Eng. Mater. 5 (2003) 837

[16] E. Ghali, W. Dietzel, K.U. Kainer, J. Mater. Eng. Performance 13 (2004) 7.

[17] N. Winzer, A. Atrens, G. Song, E. Ghali, W. Dietzel, K.U. Kainer, N. Hort, C. Blawert, Adv. Eng. Mater. 7 (2005) 659.

[18] M. Bobby Kannan, W. Dietzel, C. Blawert, S. Riekehr, M. Kocak, Mater. Sci. Eng. A, 444 (2007) 220.

[19] N. Winzer, A. Atrens, W. Dietzel, G. Song, K.U. Kainer, Comparison of the Linearly Increasing Stress Test and the Constant Extension Rate Test in the Evaluation of Transgranular Stress Corrosion Cracking of Magnesium, Mater. Sci. Eng. A, accepted for publication March 2007.

[20] I. Nakatsugawa, S. Kamado, Y. Kojima, R. Ninomiya, K. Kubota, Corros. Rev. 16 (1998) 139.

[21] J. H. Nordlien, K. Nisancioglu, S. Ono, N. Masuko, J. Electrochem. Soc. 144 (1997) 461.

[22] M. Kiryuu, H. Okumura, S. Kamado, Y. Kojima, R. Ninomiya, I. Nakatsugawa, J. Jpn. Inst. Light Met. 46 (1996) 39.

[23] J. Chang, X. Guo, P. Fu, L. Peng, W. Ding, Electrochemica Acta (2006), doi:10.1016/j.electacta.2006.09.069.

[24] S. Krishnamurthy, M. Khobaib, E. Robertson, F.H. Froes, Mater. Sci. Eng. 99 (1988) 507.

[25] R.S. Busk, Magnesium Products Design M. Dekker, USA, 1986, 256.

[26] M.A. Pelensky, A. Gallacio, Stress Corrosion Testing, STP425, ASTM 1967,107.

[27] ASM Specialty Handbook: Magnesium and Magnesium Alloys, ASM International, USA, 1999, 195.

[28] W.K. Miller, Mat Res Soc Symp Proc. 125 (1988) 253.

[29] L. Fairman, H.J. Bray, Corros. Sci. 11, 1971, 533

[30] E.C. W. Perryman, J. Inst. Met. 78 (1951), 621.

[31] F. Andreatta, I. Apachitei, A.A. Kodenstov, J. Dzwonczyk, J. Duszczyk, Electrochemica Acta 51 (2006) 3551.

[32] O.A. Lambri, W. Riehemann, Script Mater. 52 (2005) 93.

[33] P.J.Apps, H. Karimzadeh, J.F. King, G.W. Lorimer, Scripta Mater. 48 (2003) 475.

[34] C. Chen, M. Wang, D. Wang, R. Jin, Y. Liu, J. Alloys Compds (2006), doi:10.1016/j.jallcom.2006.08.057.

[35] Denny A. Jones, Principles and Prevention of Corrosion, 2nd Edition, Prentice Hall, NJ, 1996, 44.

[36] R.S. Stampella, R.P.M. Procter, V. Ashworth, Corros. Sci. 24 (1984) 325.

[37] W.M Pardue, F.H. Beck, M.G. Fontana, Trans. American Soc. Met. 54 (1961) 539.

[38] A. Atrens, N. Winzer, G.L. Song, W. Dietzel, C. Blawert, Adv. Eng. Mater. 8 (2006) 749.

[39] N. Winzer, A. Atrens, W. Dietzel, G. Song, K.U. Kainer, Evaluation of the Delayed Hydride Cracking Mechanism for Transgranular Stress Corrosion Cracking of Magnesium Alloys, Mater. Sci. Eng. A, accepted for publication March 2007.

Table 1 Chemical composition of AZ80, ZE41, QE22 and EV31A

Alloy	Al	Zn	Mn	Ag	Nd	Gd	Zr	Fe	TRE	Mg
AZ80	8.59	0.45	0.16	-	-	-	-	0.003	-	Bal.
ZE41	-	4.13	-	-	-	-	0.70	0.003	1.18	Bal.
QE22	-	-	-	2.23	2.03	-	0.64	-	2.09	Bal.
EV31A	-	0.48	-	-	2.85	1.32	0.50	-	-	Bal.

Table 2 Thermo-mechanical treatments for AZ80, ZE41, QE22 and EV31A

Alloy	Thermo-mechanical treatment
AZ80	T5 – Stress relieved for 8 h at 385°C and then aged for 16 h at 180°C.
ZE41	T5 – Stress relieved for 2 h at 330°C and then aged for 16 h at 180°C.
QE22	T6 – Solution treated for 8 h at 520°C followed by hot water quenching and then aged for 16 h at 200°C.
EV31A	T6 – Solution treat for 8 h at 520°C followed by hot water quenching and then aged for 16 h at 200°C.

Table 3 Summary of mechanical property values of AZ80, ZE41, QE22 and EV31A

Alloy	Strain rate (s^{-1})	ε_f (%)	0.2 % Proof stress (MPa)	UTS (MPa)
AZ80	Typical*	7	275	380
	Min*	6	205	310
	10^{-4}	11	220	350
	10^{-6}	19	220	350
ZE41	Typical	5	150	220
	Min	3	140	200
	10^{-4}	6	130	190
	10^{-6}	9	125	200
QE22	Typical	4	200	270
	Min	2	180	240
	10^{-4}	11	165	250
	10^{-6}	23	165	230
EV31A	Typical	7	175	290
	Min	2	150	250
	10^{-4}	7	170	280
	10^{-6}	6	170	270

Note: * Min = minimum, Typical = typical values [6]

Table 4 Summary of SSRT results of AZ80, ZE41, QE22 and EV31A

Alloy	Strain rate s^{-1}	ε_f (%)			UTS (MPa)		
		Air	DW*	NaCl*	Air	DW*	NaCl*
AZ80	10^{-6}	19	11	7	350	320	290
	10^{-7}	-	2	2	-	230	220
ZE41	10^{-6}	9	8	3	200	190	160
	10^{-7}	-	5	2	-	160	130
QE22	10^{-6}	23	12	3	230	230	190
	10^{-7}	-	6	1	-	200	150
EV31A	10^{-6}	6	6	4	270	250	230
	10^{-7}	-	6	4	-	240	230

Note: * DW= Distilled water, NaCl = 0.5 wt.% NaCl solution

Table 5 The I_{SCC} susceptibility indices for AZ80, ZE41, QE22 and EV31A, tested at 10^{-6}/s strain rate.

Alloy	I_{SCC} (distilled water/air)		I_{SCC} (0.5 wt.% NaCl/air)		I_{SCC} (0.5 wt.% NaCl /distilled water)	
	ε_f	UTS	ε_f	UTS	ε_f	UTS
AZ80	0.55	0.91	0.35	0.83	0.63	0.91
ZE41	0.85	0.95	0.35	0.80	0.41	0.84
QE22	0.53	0.98	0.12	0.82	0.23	0.83
EV31A	0.98	0.93	0.70	0.85	0.71	0.92

Table 6 The I_{SCC} susceptibility indices for AZ80, ZE41, QE22 and EV31A, tested at 10^{-7}/s strain rate.

Alloy	I_{SCC} (distilled water/air)		I_{SCC} (0.5 wt.% NaCl/air)		I_{SCC} (0.5 wt.% NaCl /distilled water)	
	ε_f	UTS	ε_f	UTS	ε_f	UTS
AZ80	0.11	0.65	0.09	0.62	0.86	0.95
ZE41	0.59	0.83	0.17	0.66	0.28	0.79
QE22	0.28	0.84	0.05	0.65	0.17	0.77
EV31A	0.97	0.89	0.67	0.85	0.69	0.95

Table 7 The fracture modes of AZ80, ZE41, QE22 and EV31A in distilled water and 0.5 wt.% NaCl solution.

Alloy	Fracture mode	
	Distilled water	0.5 wt.% NaCl
AZ80	TGSCC	TGSCC
ZE41	TGSCC/IGSCC	IGSCC/TGSCC
QE22	TGSCC/IGSCC	IGSCC/TGSCC
EV31A	Ductile/ TGSCC	IGSCC/TGSCC

Note: TGSCC – Transgranular stress corrosion cracking; IGSCC – Intergranular stress corrosion cracking

Figure Captions

Fig. 1 Schematic diagram of slow strain rate test (SSRT) apparatus

Fig. 2 Optical micrographs (a) AZ80, (b) ZE41 (c) QE22 and (d) EV31A.

Fig. 3 Stress-strain plot of : (a) AZ80, (b) ZE41, (c) QE22 and (d) EV31A tested in air, distilled water and 0.5 wt.% NaCl solution.

Fig. 4 Macrographs of failed SSRT samples: in distilled water (a) AZ80, (c) ZE41 (e) QE22 and (f) EV31A; in 0.5 wt.% NaCl solution (b) AZ80, (d) ZE41 (f) QE22 and (h) EV31A.

Fig.5 Fracture surfaces of AZ80 failed in air at 10^{-6}/s strain rate: (a) overview and (b) shows dimple rupture.

Fig. 6 Fracture surfaces of AZ80 failed in distilled water at 10^{-7}/s strain rate: (a) overview, (b) circumferential edge shows predominantly transgranular fracture and (c) shows localized secondary cracking; (d) the centre of the fracture surface reveals ductile tearing.

Fig. 7 Fracture surfaces of AZ80 failed in 0.5 wt.% NaCl solution at 10^{-7}/s strain rate: (a) overview, (b circumferential edge shows localized corrosion and (c) shows mix-mode failure; (d) the centre of the fracture surface reveals mix-mode failure.

Fig. 8 Fracture surfaces of ZE41 failed in air at 10^{-6}/s strain rate: (a) overview (b) shows dimple rupture along the grain boundaries.

Fig. 9 Fracture surfaces of ZE41 failed in distilled water at 10^{-7}/s strain rate: (a) overview, (b) and (c) shows corrosion along the grain boundaries.

Fig. 10 Fracture surfaces of ZE41 failed in 0.5 wt.% NaCl solution at 10^{-7}/s strain rate: (a) overview, (b), (c) and (d) shows predominant grain boundary corrosion.

Fig. 11 Fracture surfaces of QE22 failed in air at 10^{-6}/s strain rate: (a) overview, (b) and (c) shows dimple rupture and brittle fracture.

Fig. 12 Fracture surfaces of QE22 failed in distilled water at 10^{-7}/s strain rate: (a) overview (b) circumferential edge shows typical transgranular cleavage, (c) shows mix-mode failure; (d) the centre of the fracture surface shows intergranular cracking.

Fig. 13 Fracture surfaces of QE22 failed in 0.5 wt.% NaCl solution at 10^{-7}/s strain rate: (a) overview (b),(c) and (d) shows mix-mode failure.

Fig. 14 Fracture surfaces of EV31A failed air at 10^{-6}/s strain rate: (a) overview (b) shows jumbled transgranular fracture.

Fig. 15 Fracture surfaces of EV31A failed in distilled water at 10^{-7}/s strain rate: (a) overview, (b), (c) and (d) shows ductile features as well as transgranular cracking.

Fig. 16 Fracture surfaces of EV31A failed in 0.5 wt.% NaCl solution at 10^{-7}/s strain rate: (a) overview, (b) (c) and (d) shows mix-mode failure.

Figure 1
Click here to download high resolution image

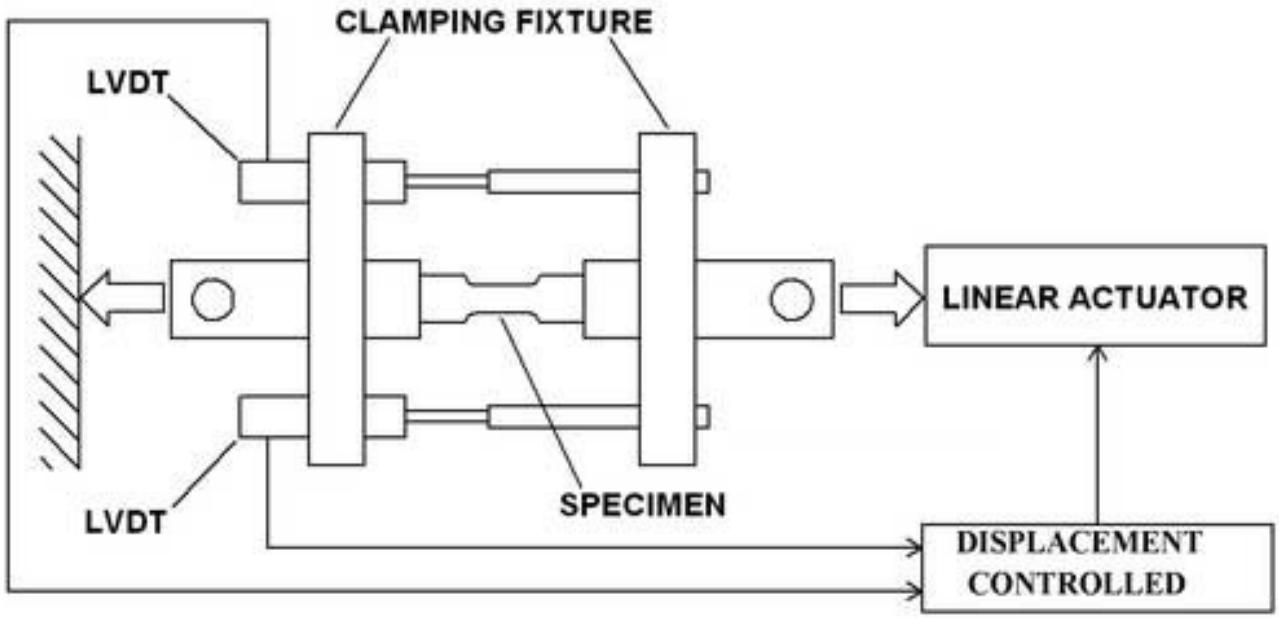

Figure 2a
Click here to download high resolution image

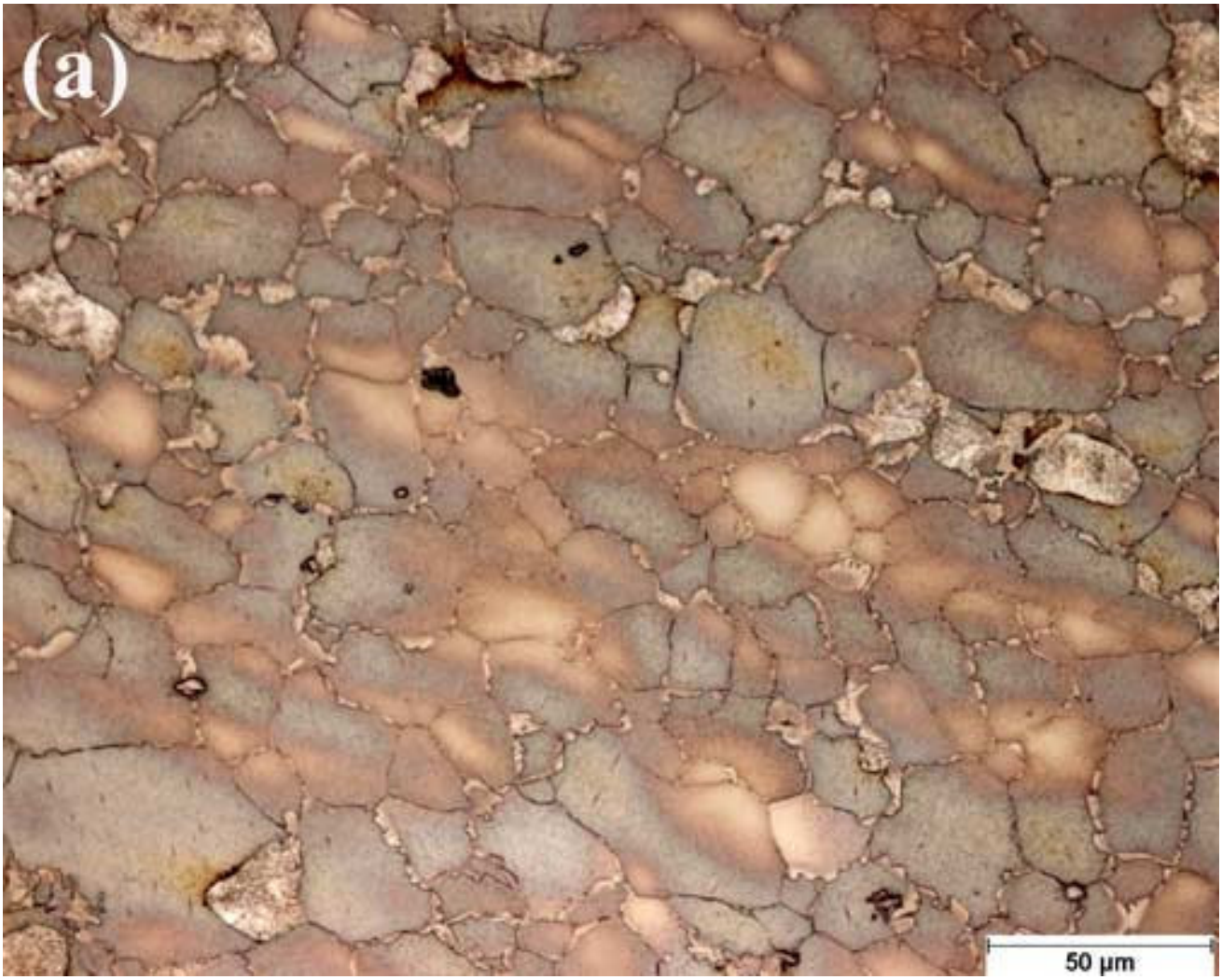

Figure 2b
Click here to download high resolution image

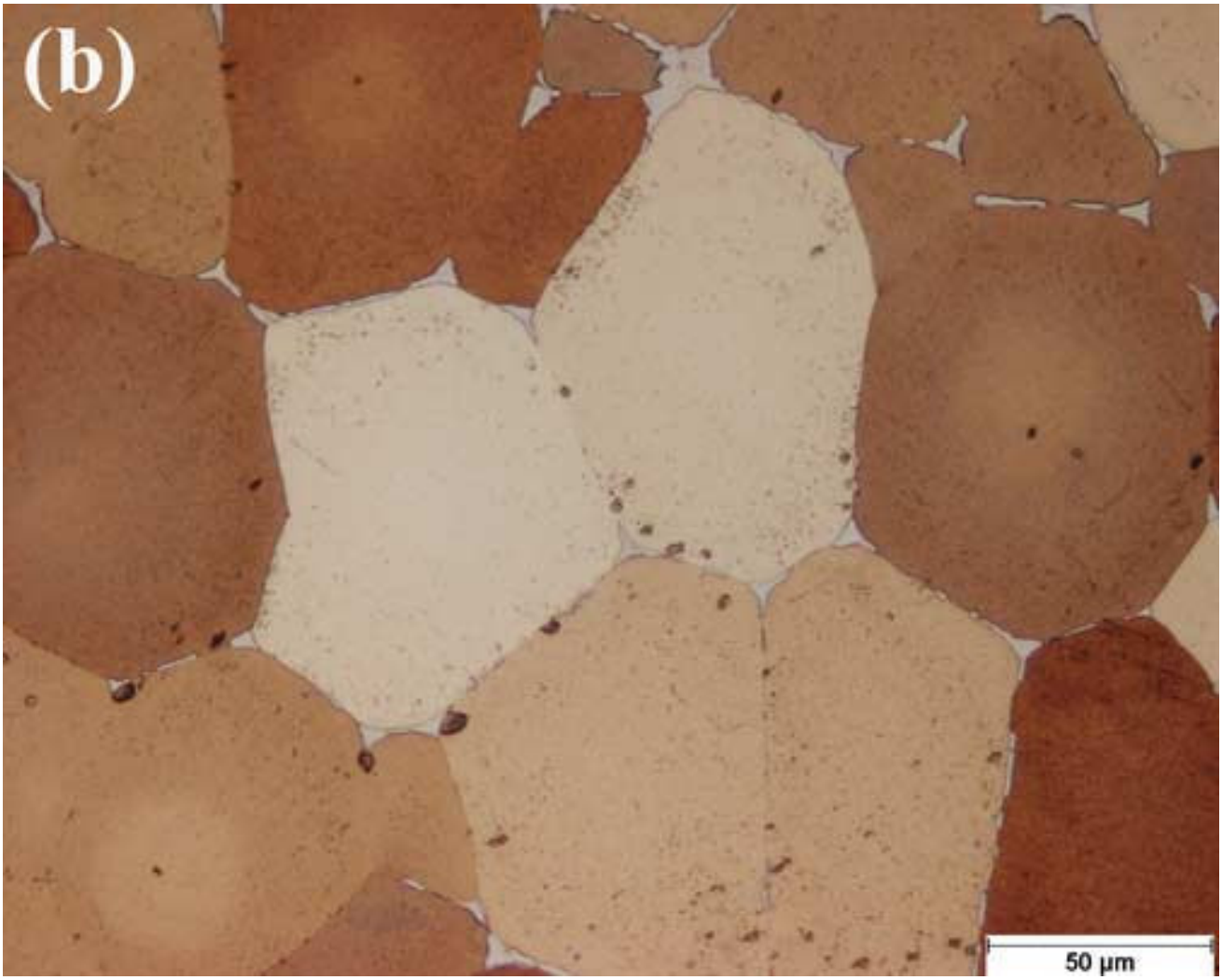

Figure 2c
Click here to download high resolution image

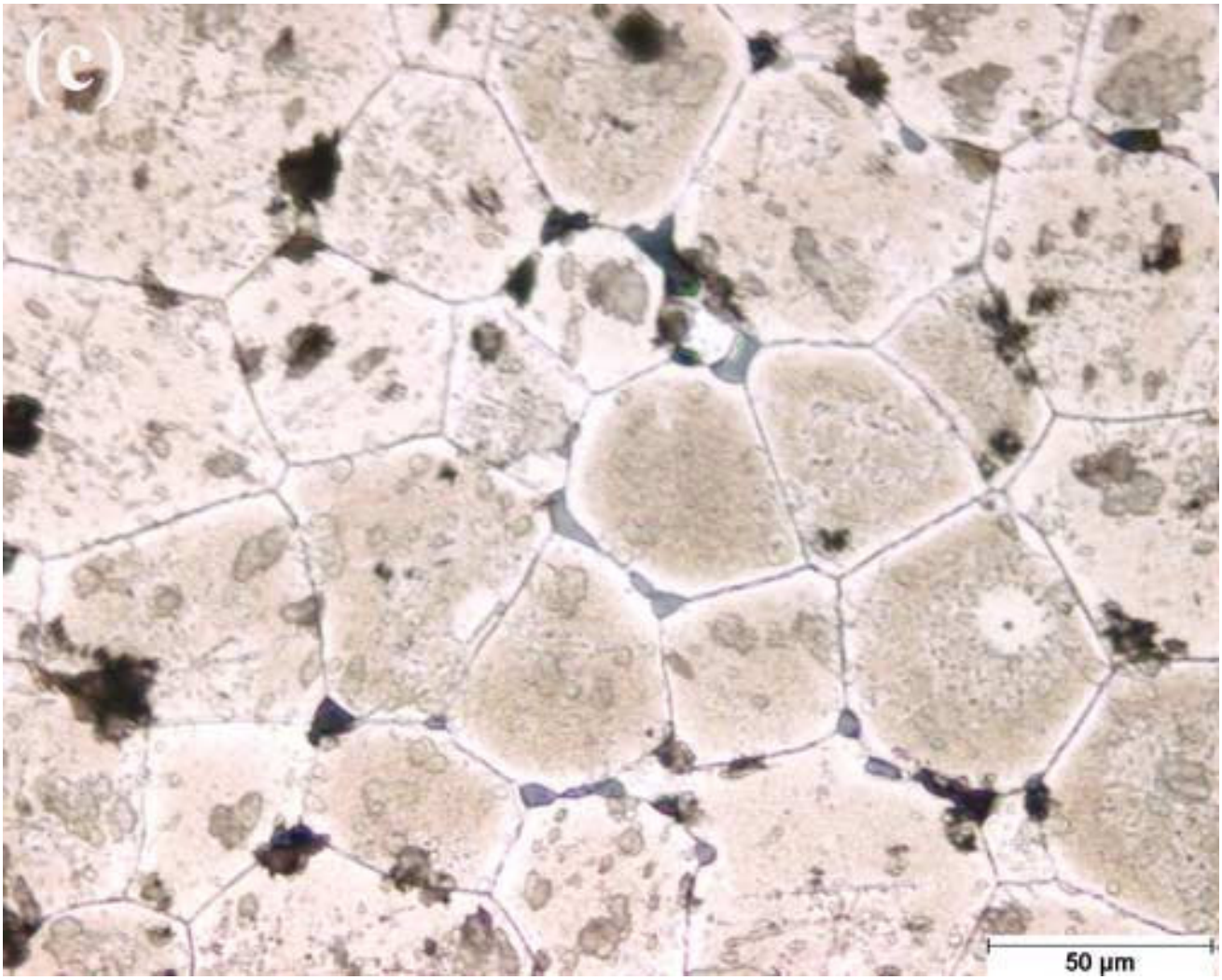

Figure 2d
Click here to download high resolution image

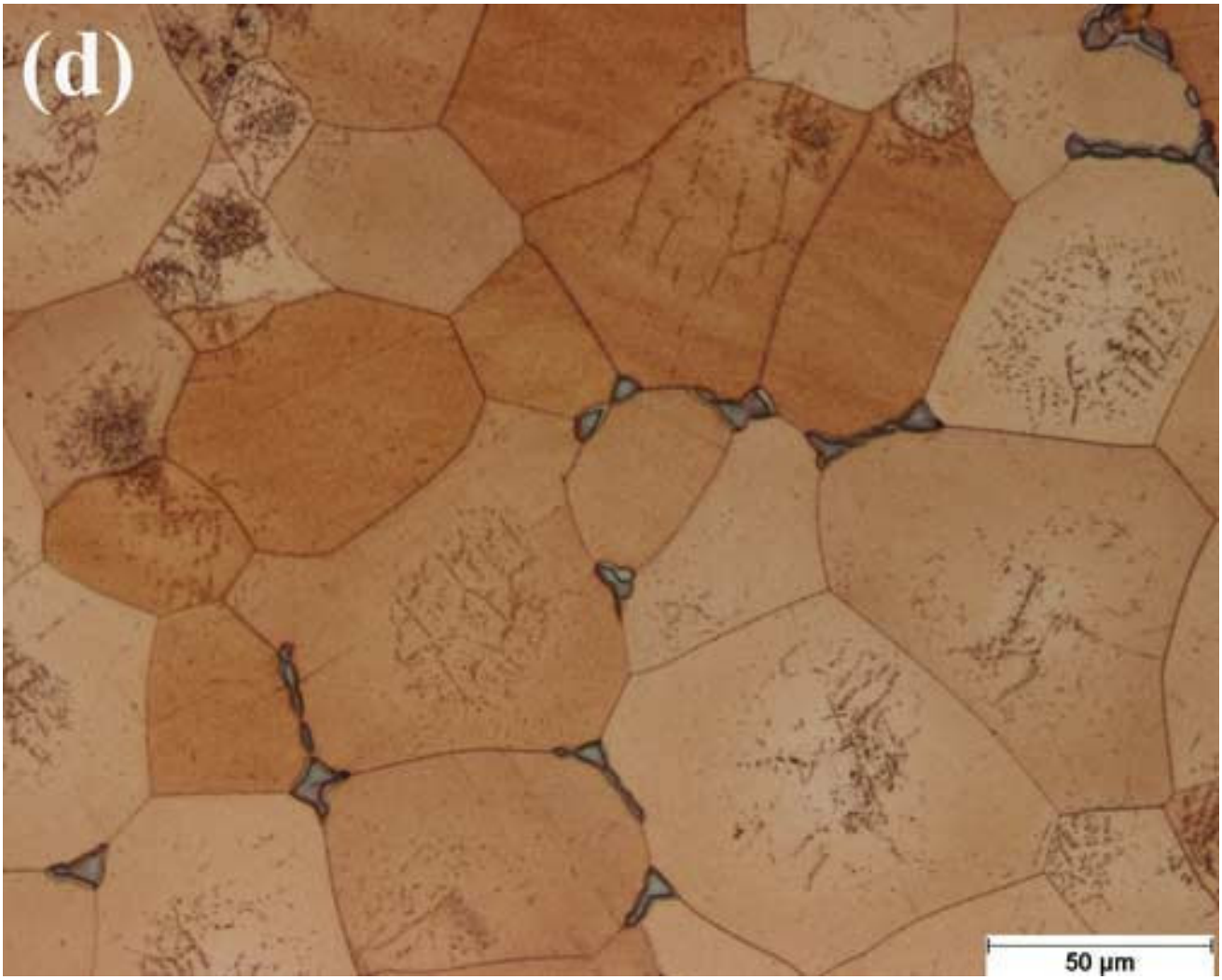

Figure 3a
Click here to download high resolution image

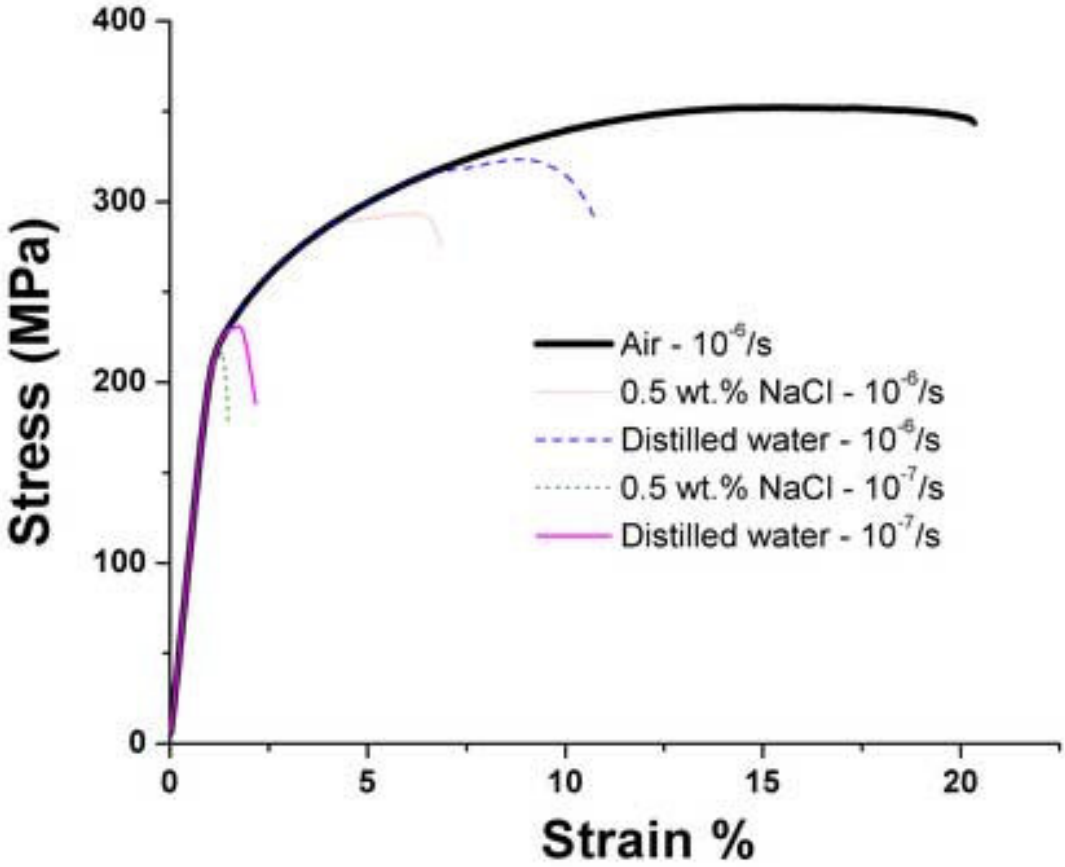

Figure 3b
Click here to download high resolution image

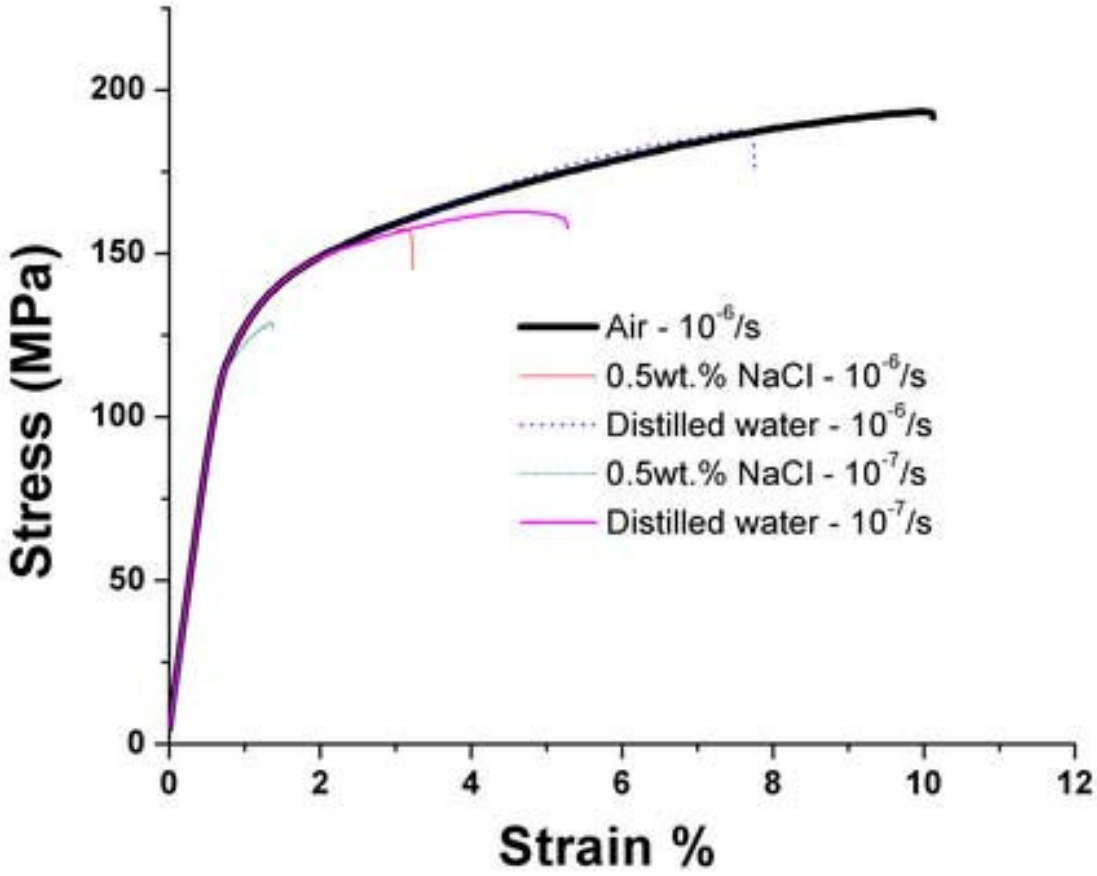

Figure 3c
Click here to download high resolution image

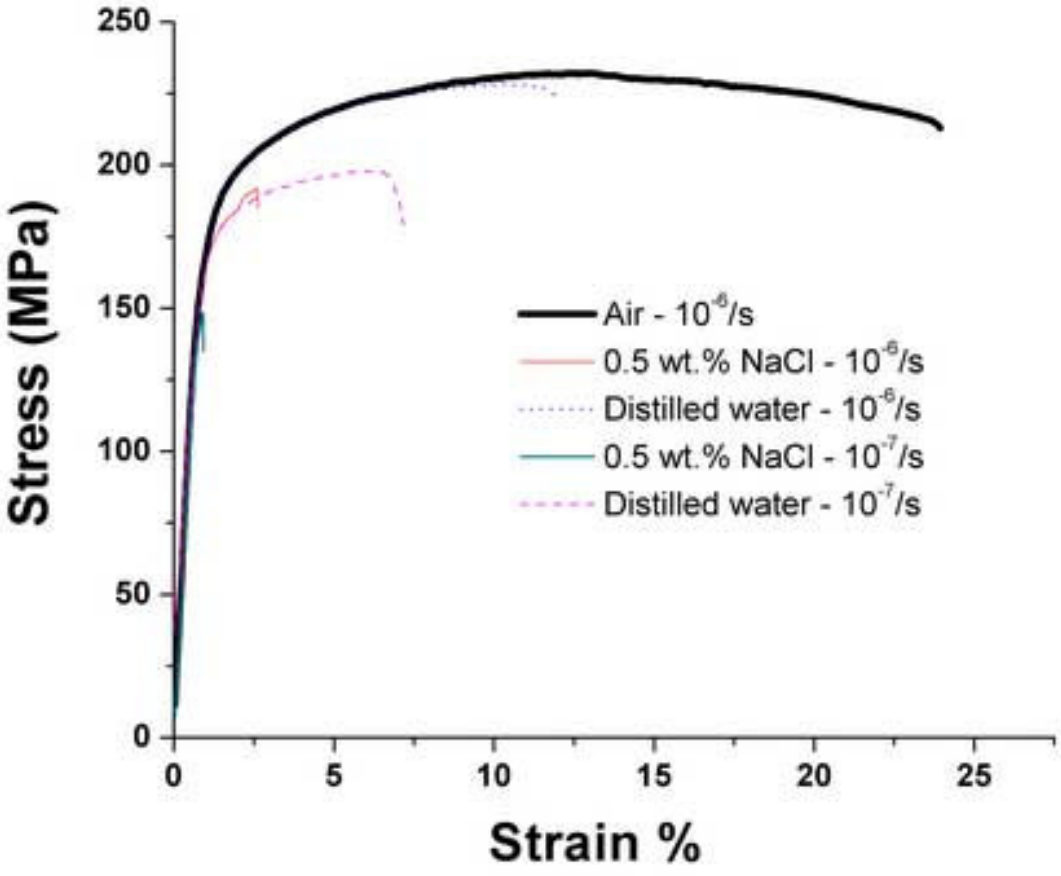

Figure 3d
Click here to download high resolution image

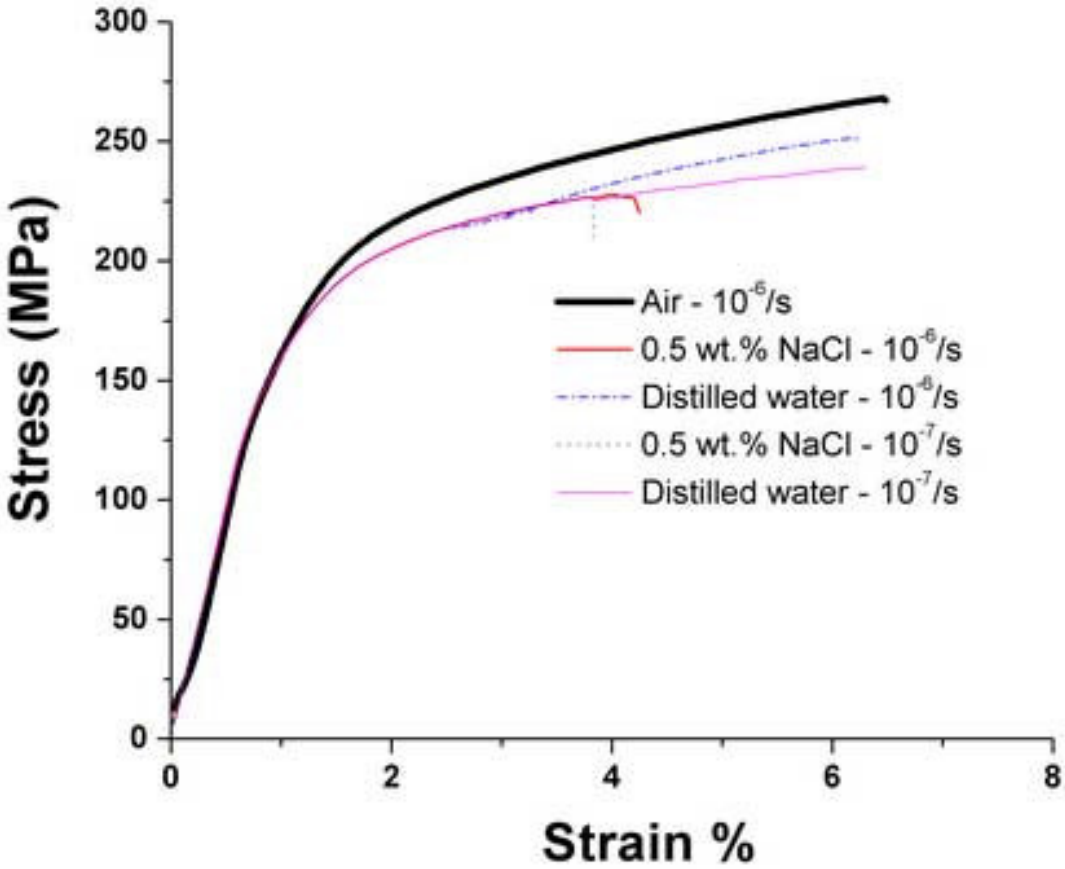

Figure 4a
Click here to download high resolution image

Figure 4b
Click here to download high resolution image

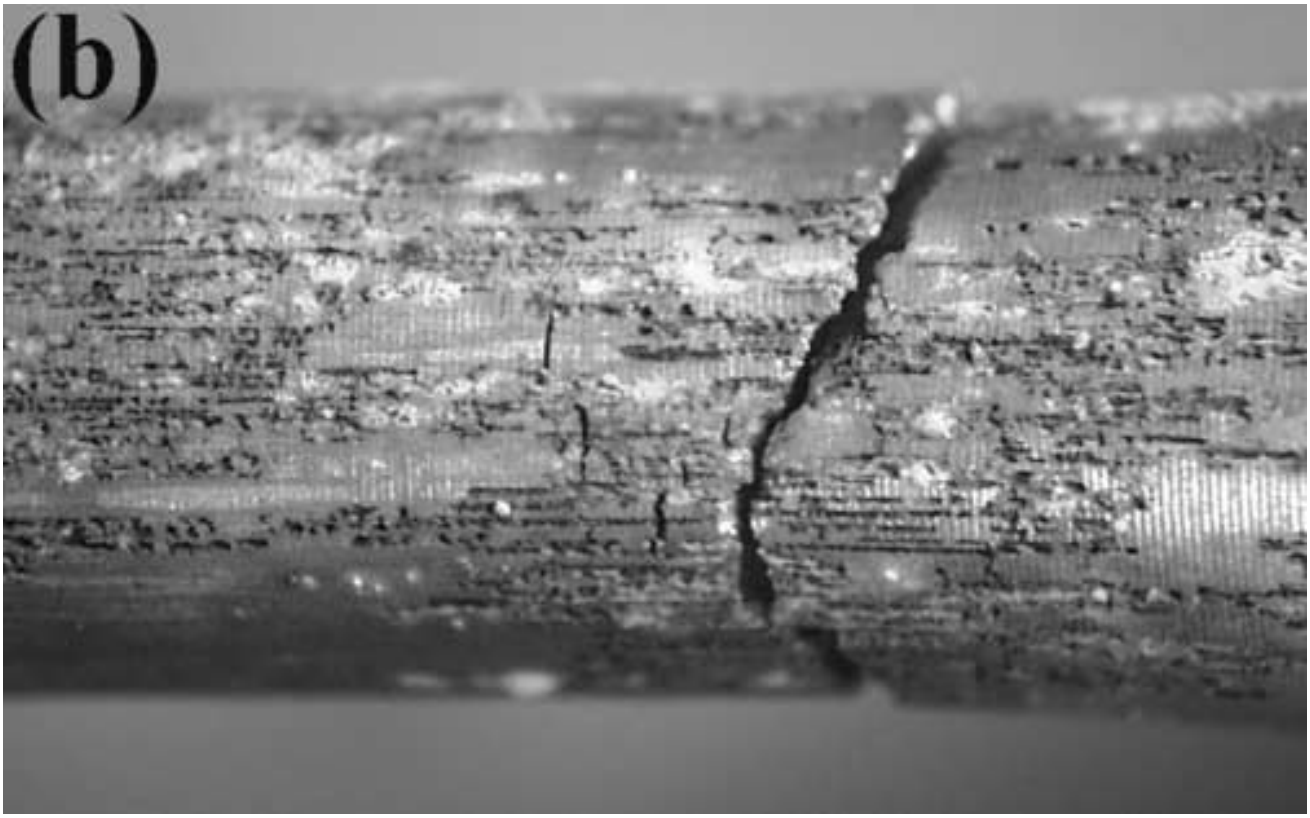

Figure 4c
Click here to download high resolution image

Figure 4d
Click here to download high resolution image

Figure 4e
Click here to download high resolution image

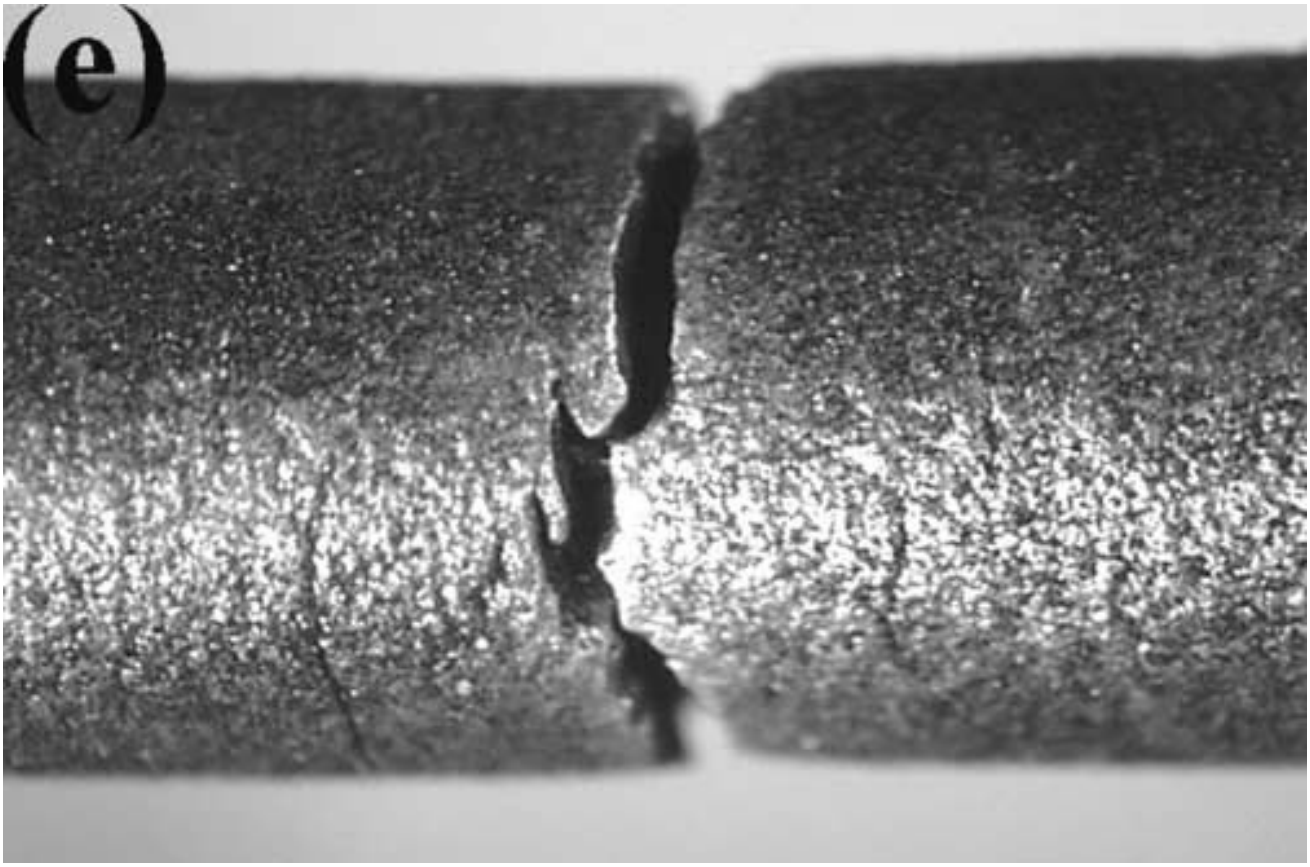

Figure 4f
Click here to download high resolution image

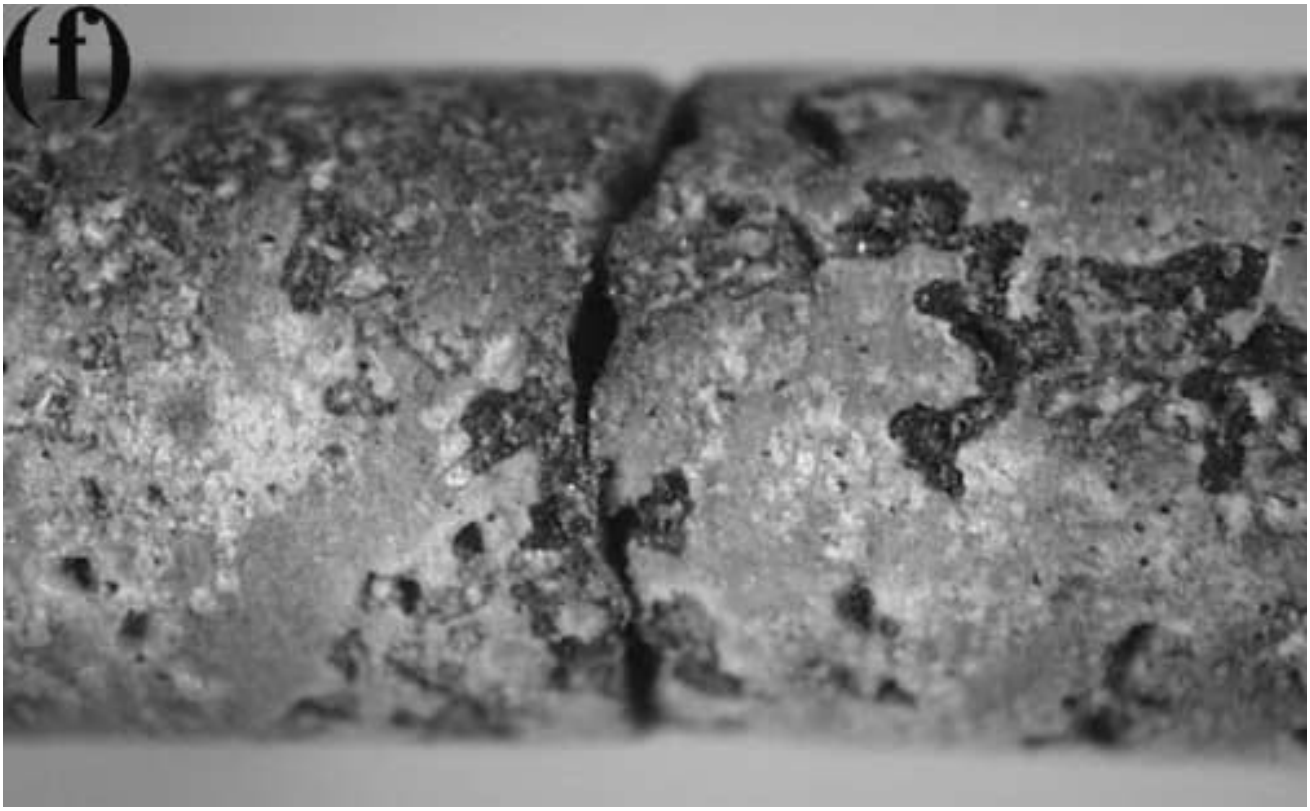

Figure 4g
Click here to download high resolution image

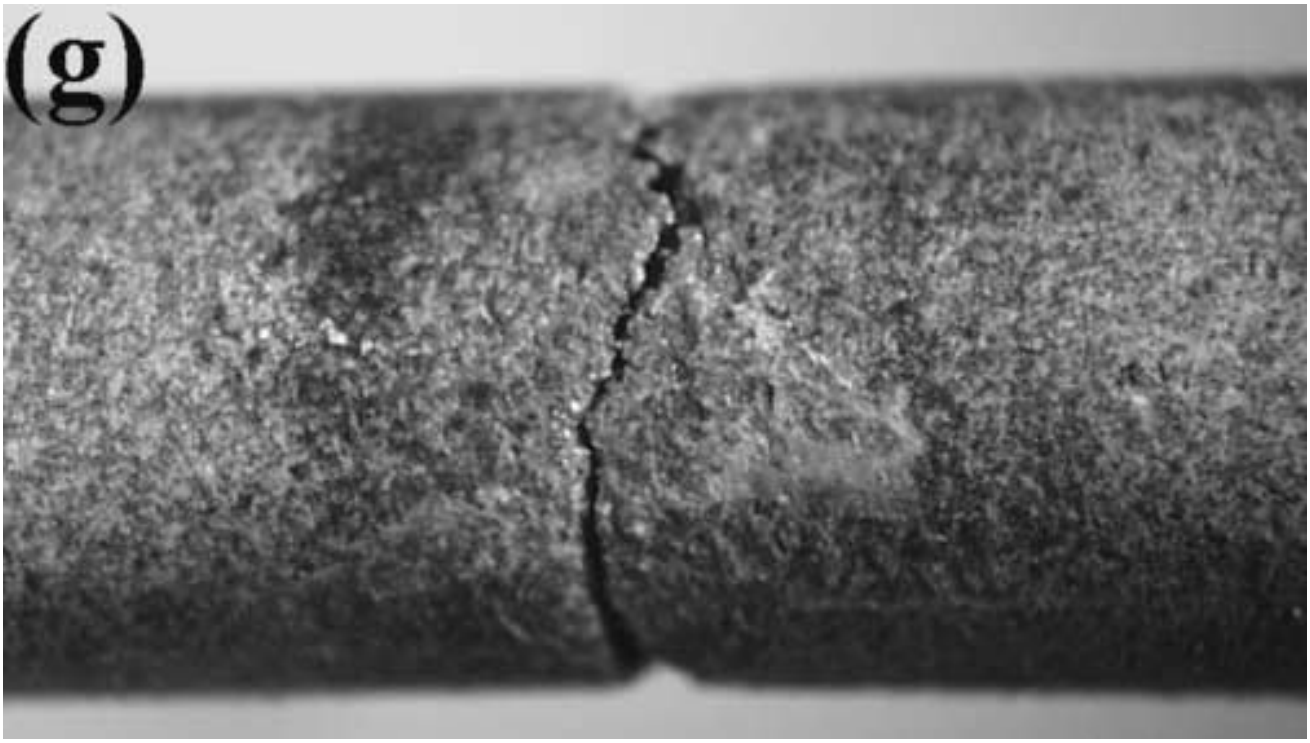

Figure 4h
Click here to download high resolution image

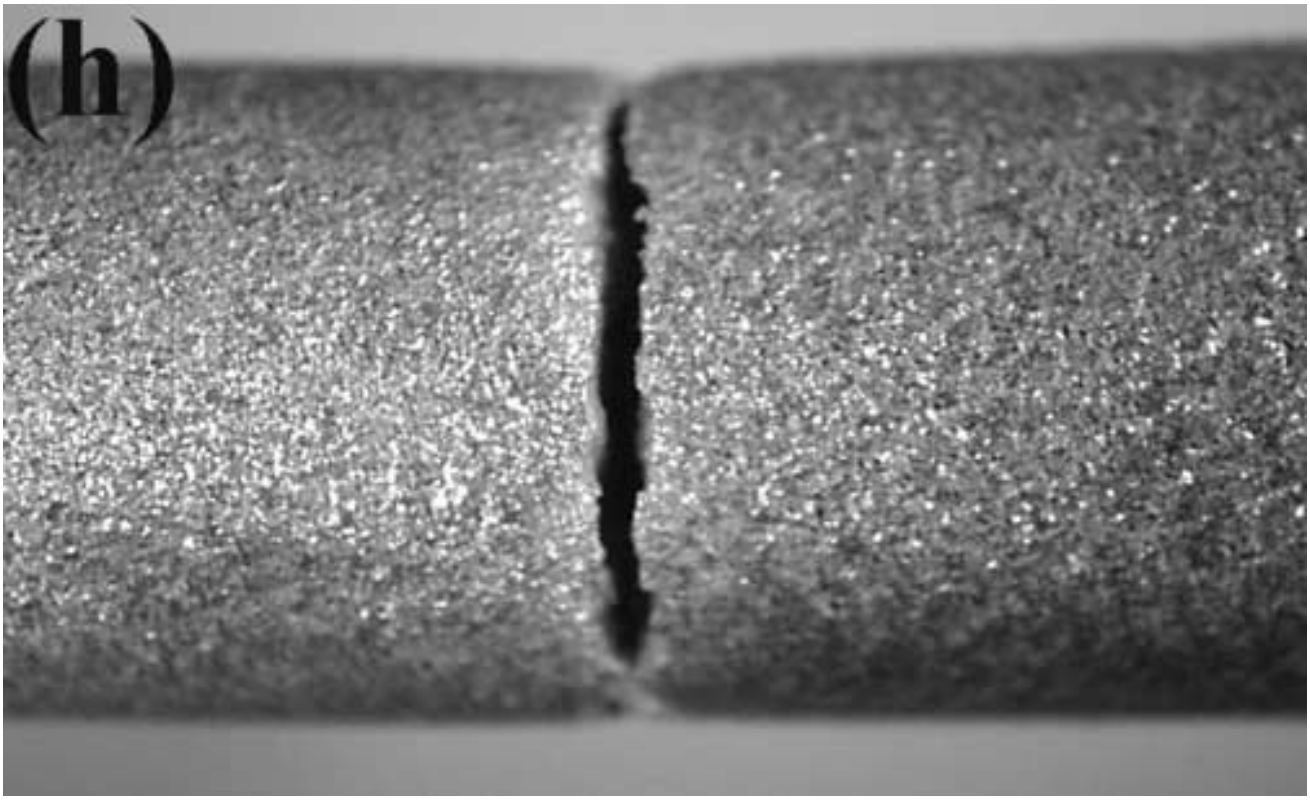

Figure 5a
Click here to download high resolution image

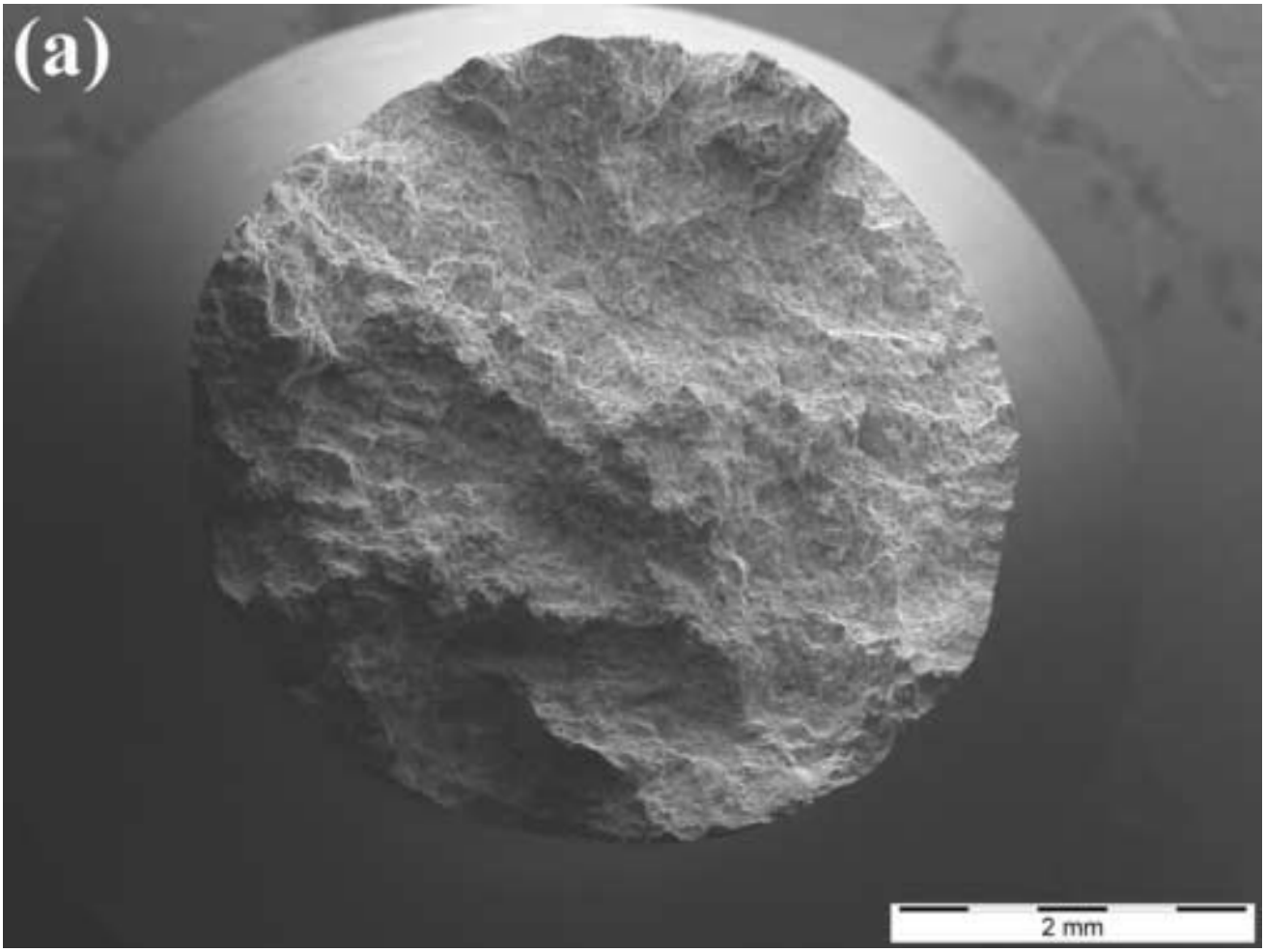

Figure 5b
Click here to download high resolution image

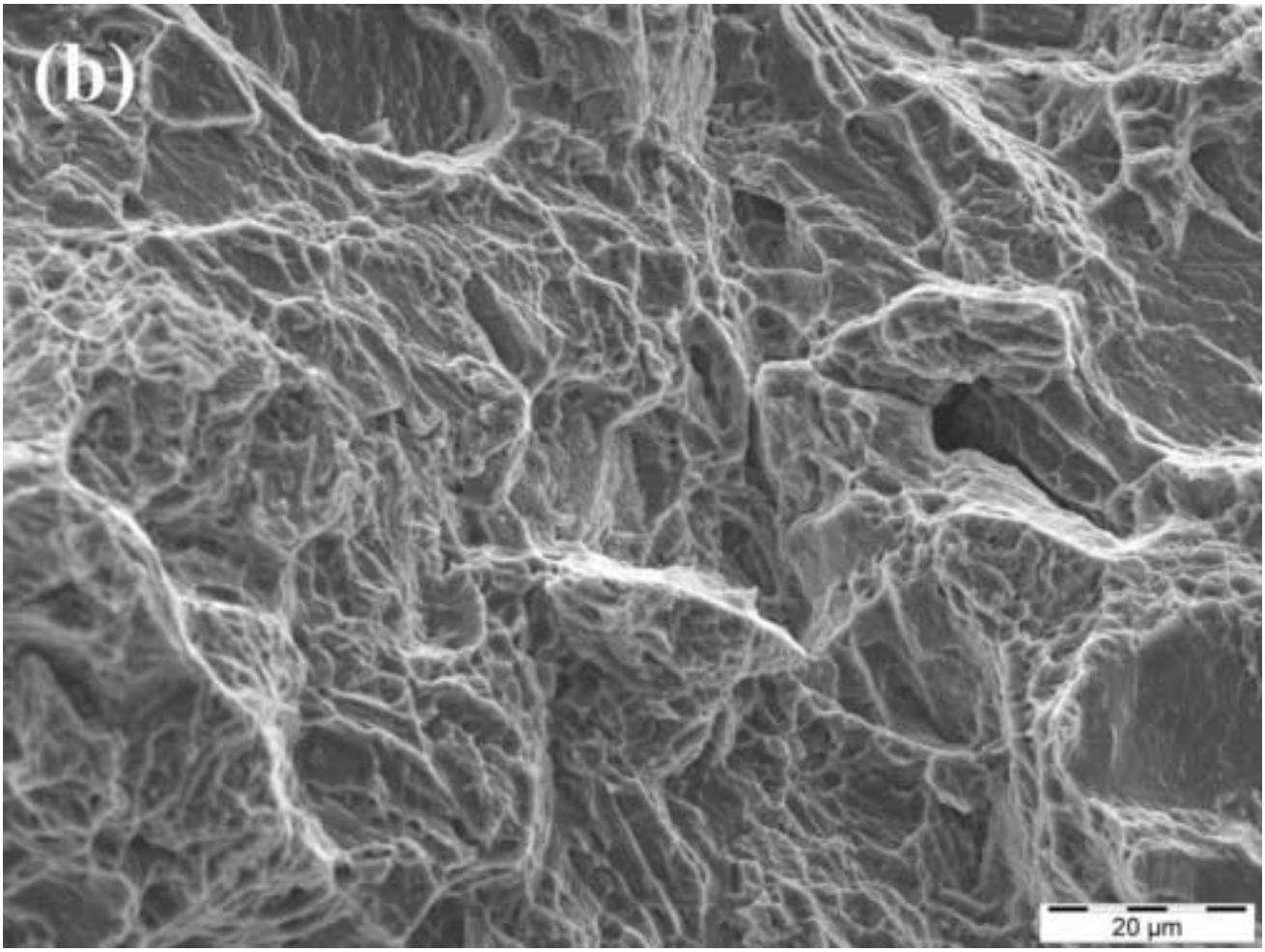

Figure 6a
Click here to download high resolution image

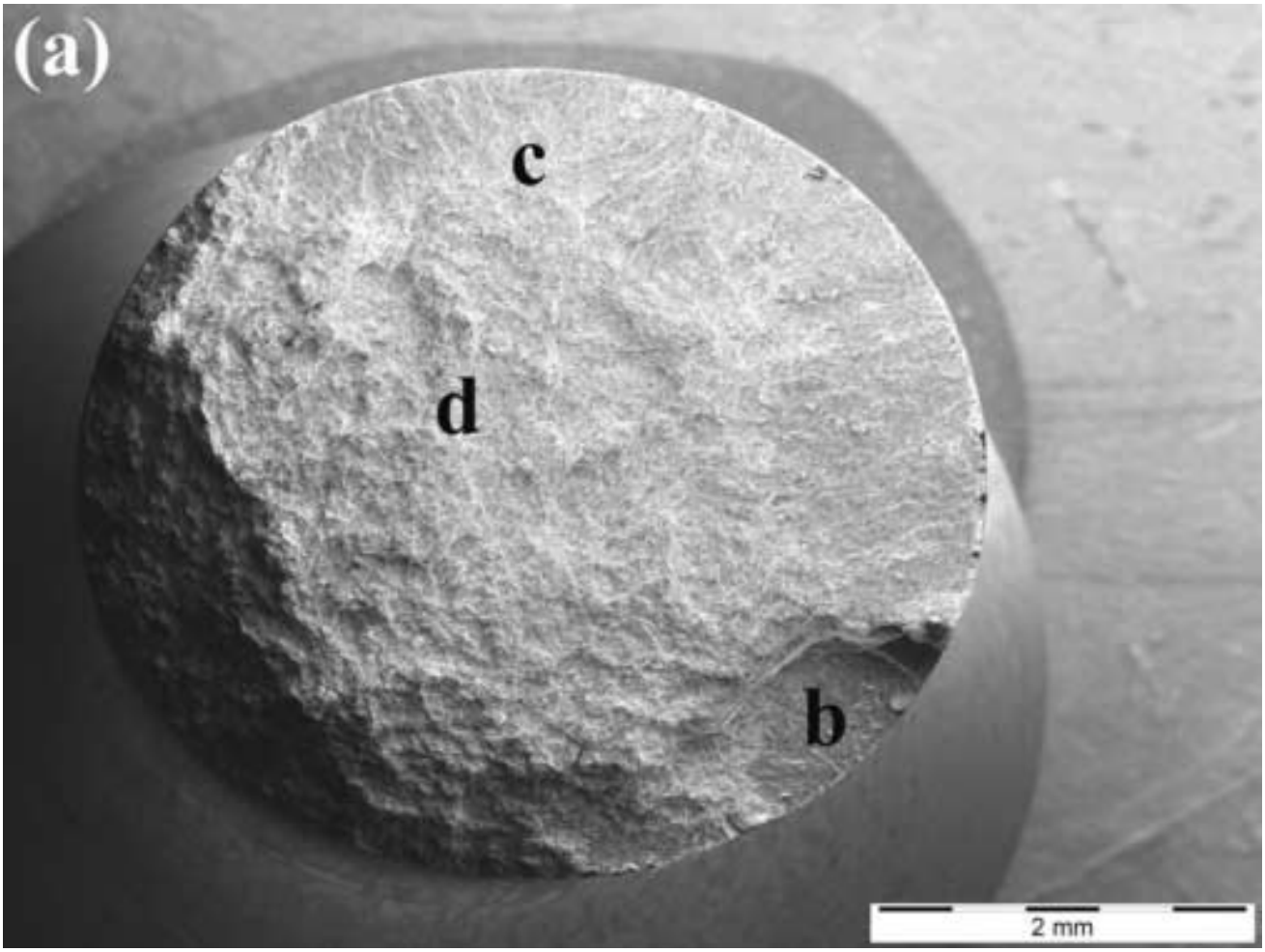

Figure 6b
Click here to download high resolution image

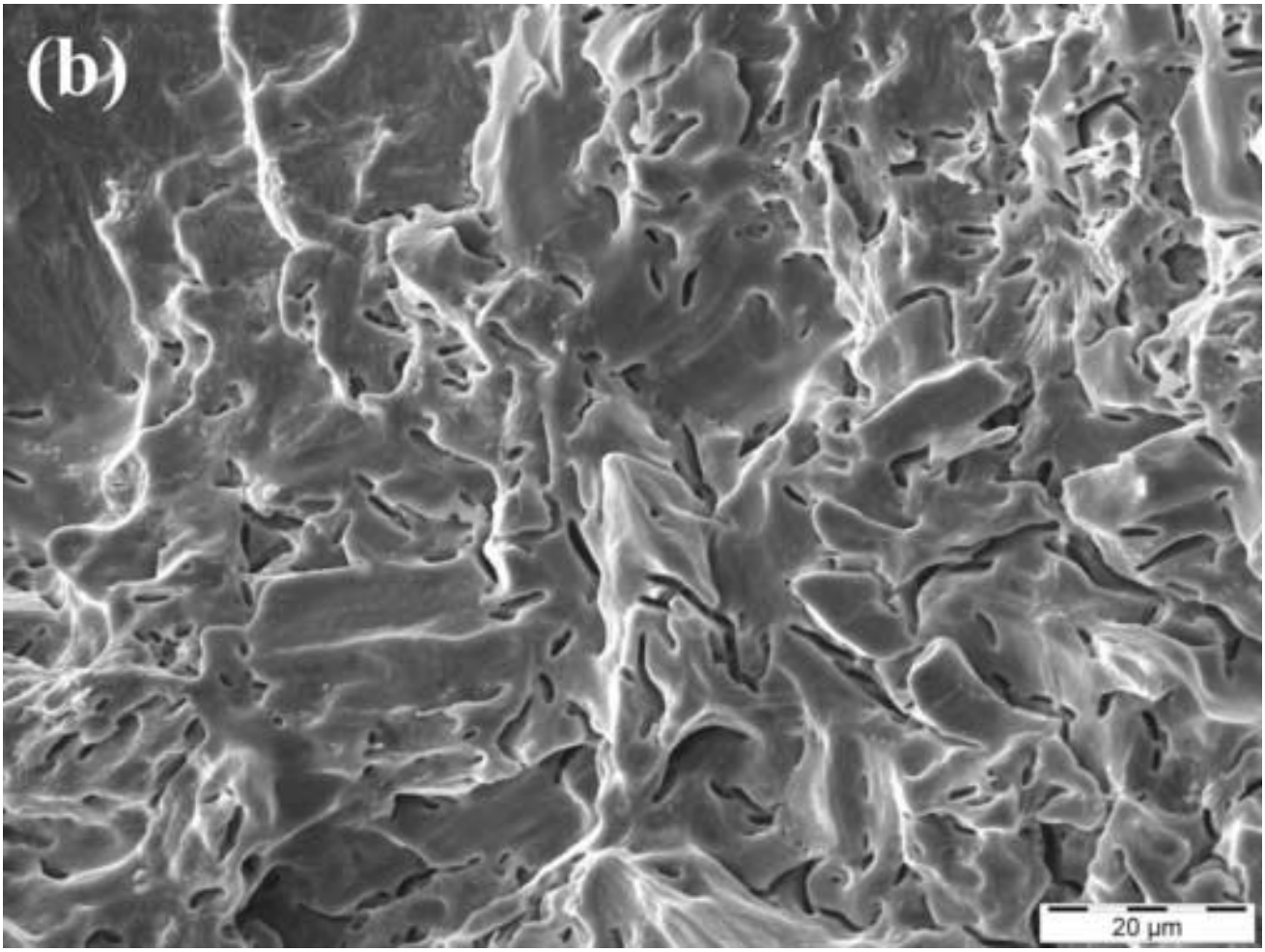

Figure 6c
Click here to download high resolution image

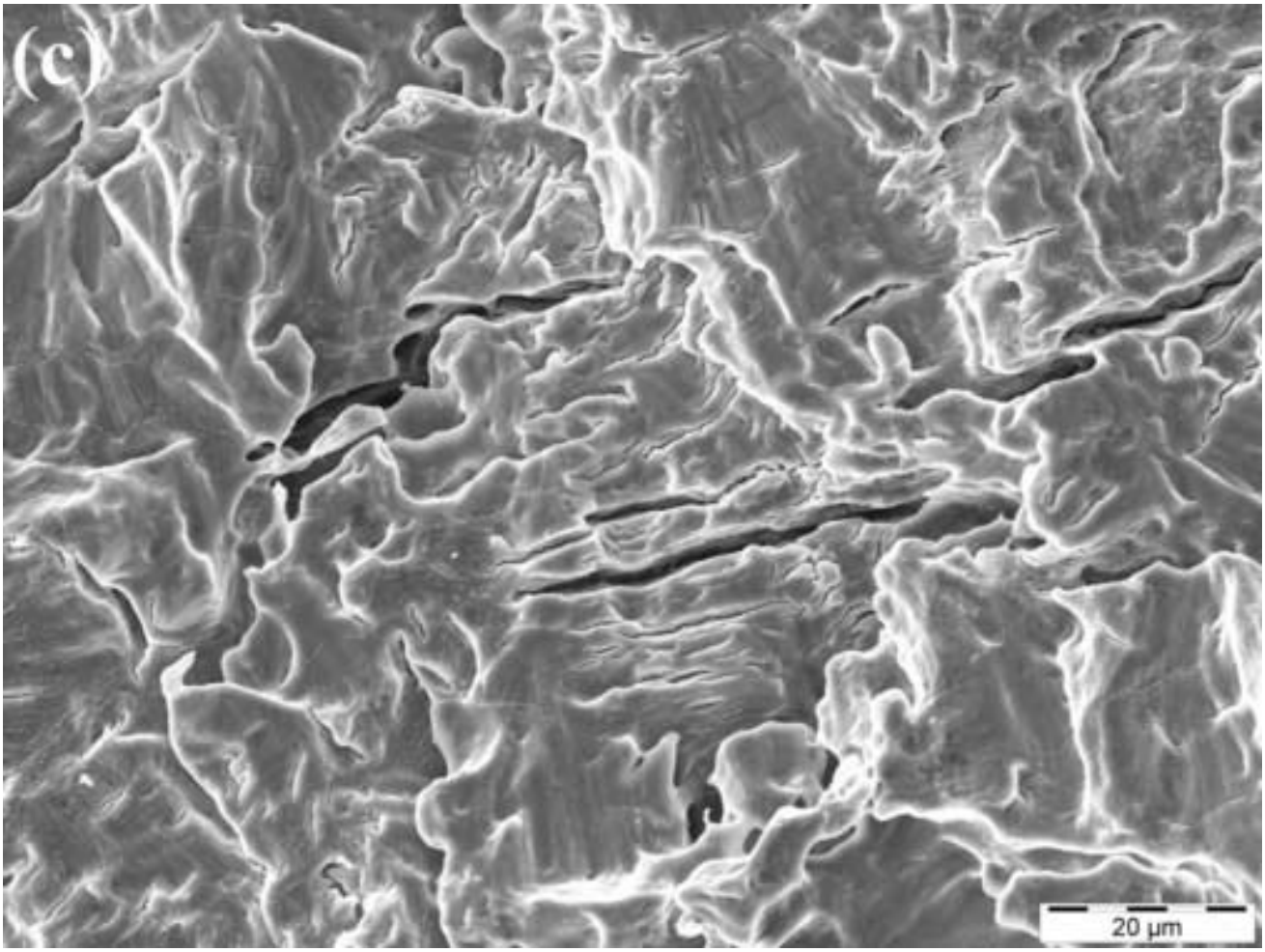

Figure 6d
Click here to download high resolution image

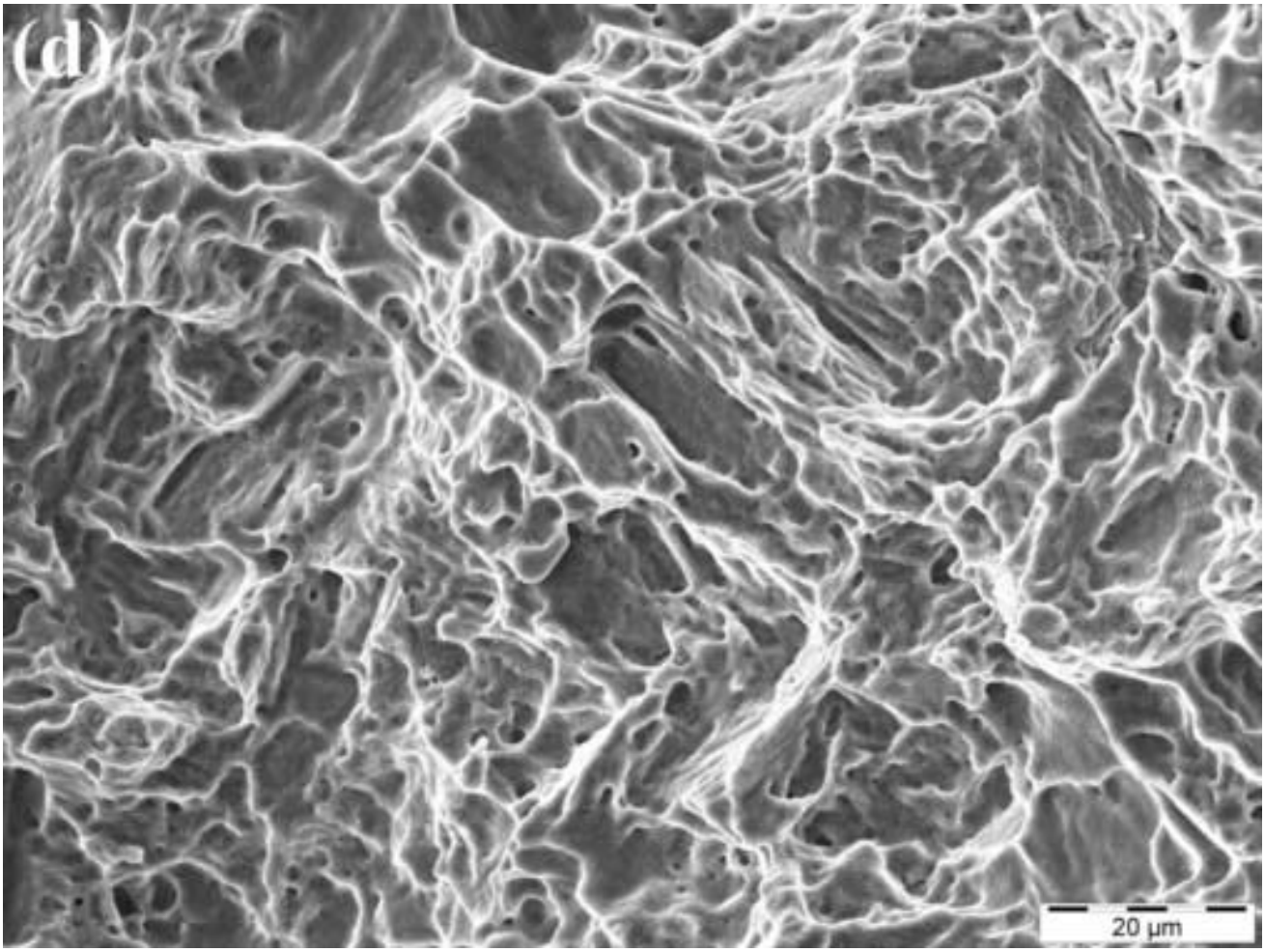

Figure 7a
Click here to download high resolution image

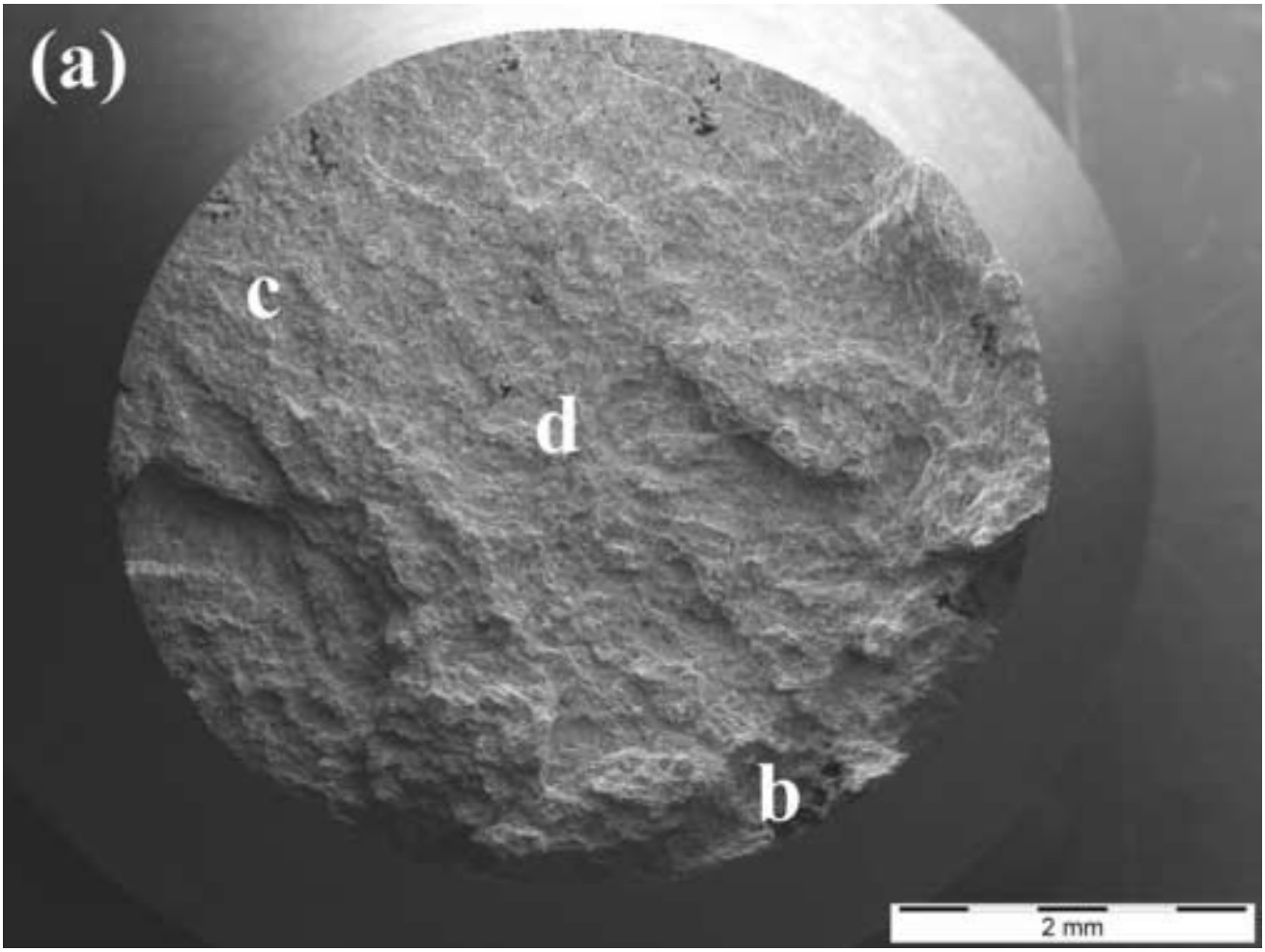

Figure 7b
Click here to download high resolution image

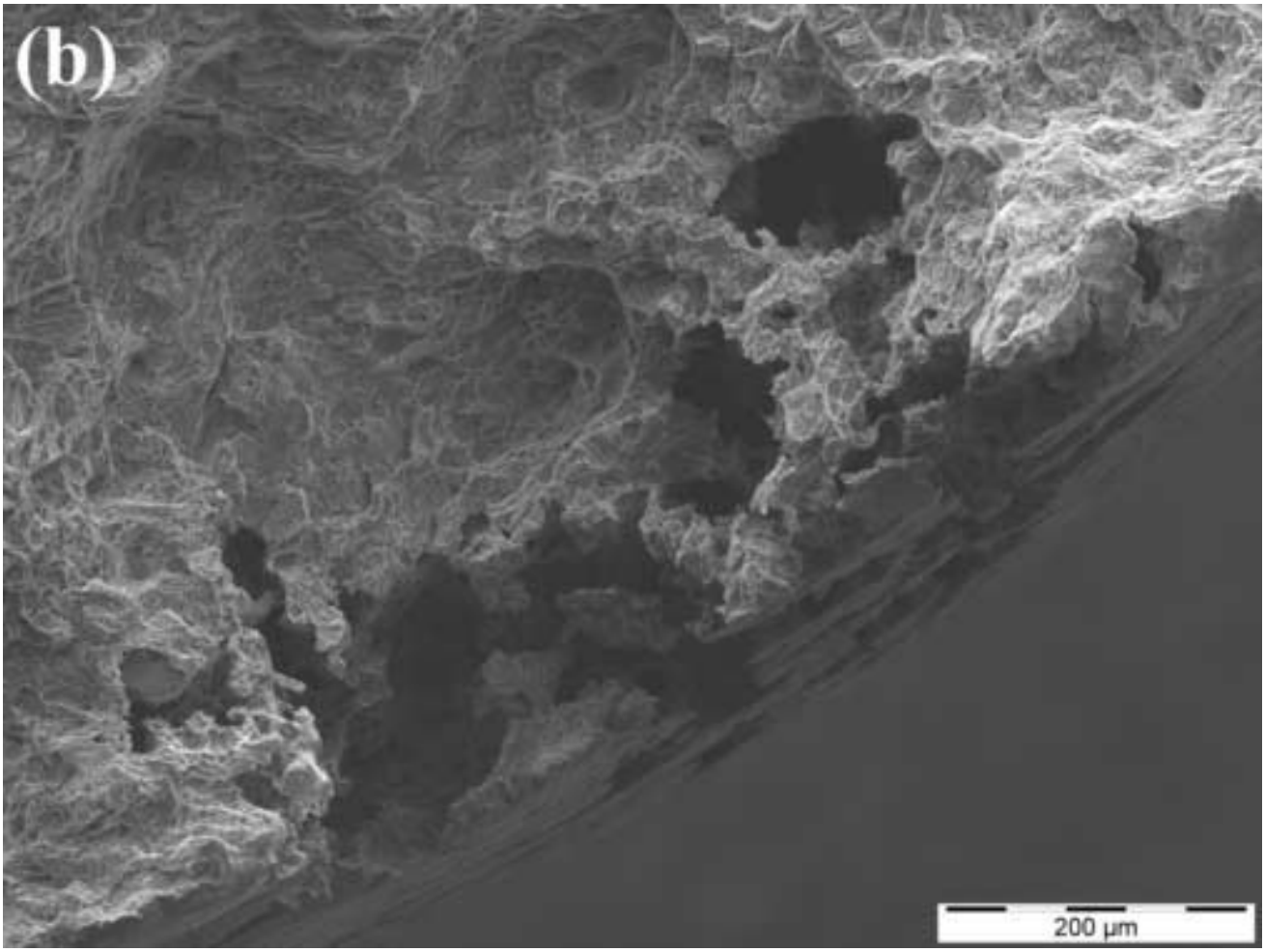

Figure 7c
Click here to download high resolution image

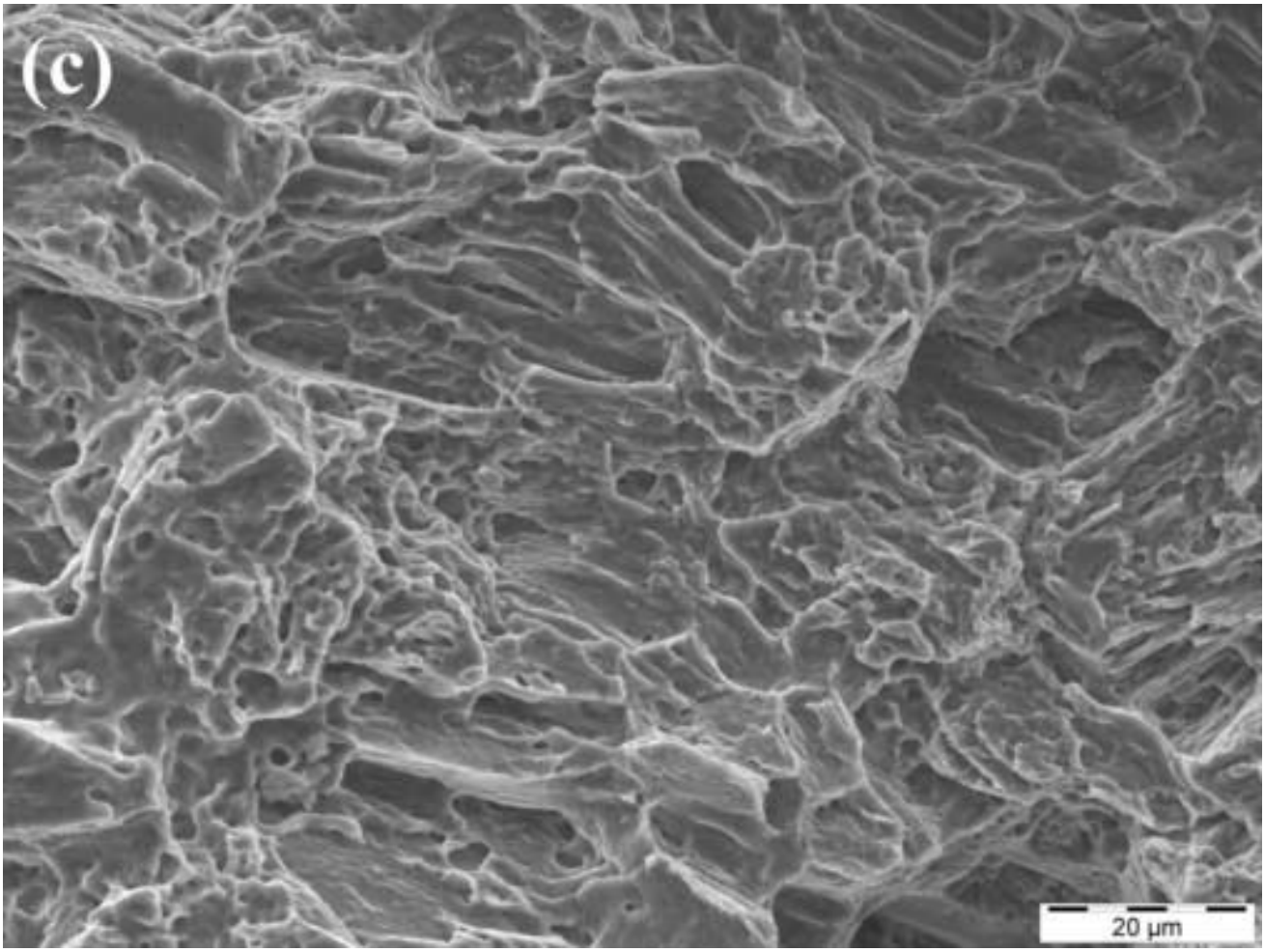

Figure 7d
Click here to download high resolution image

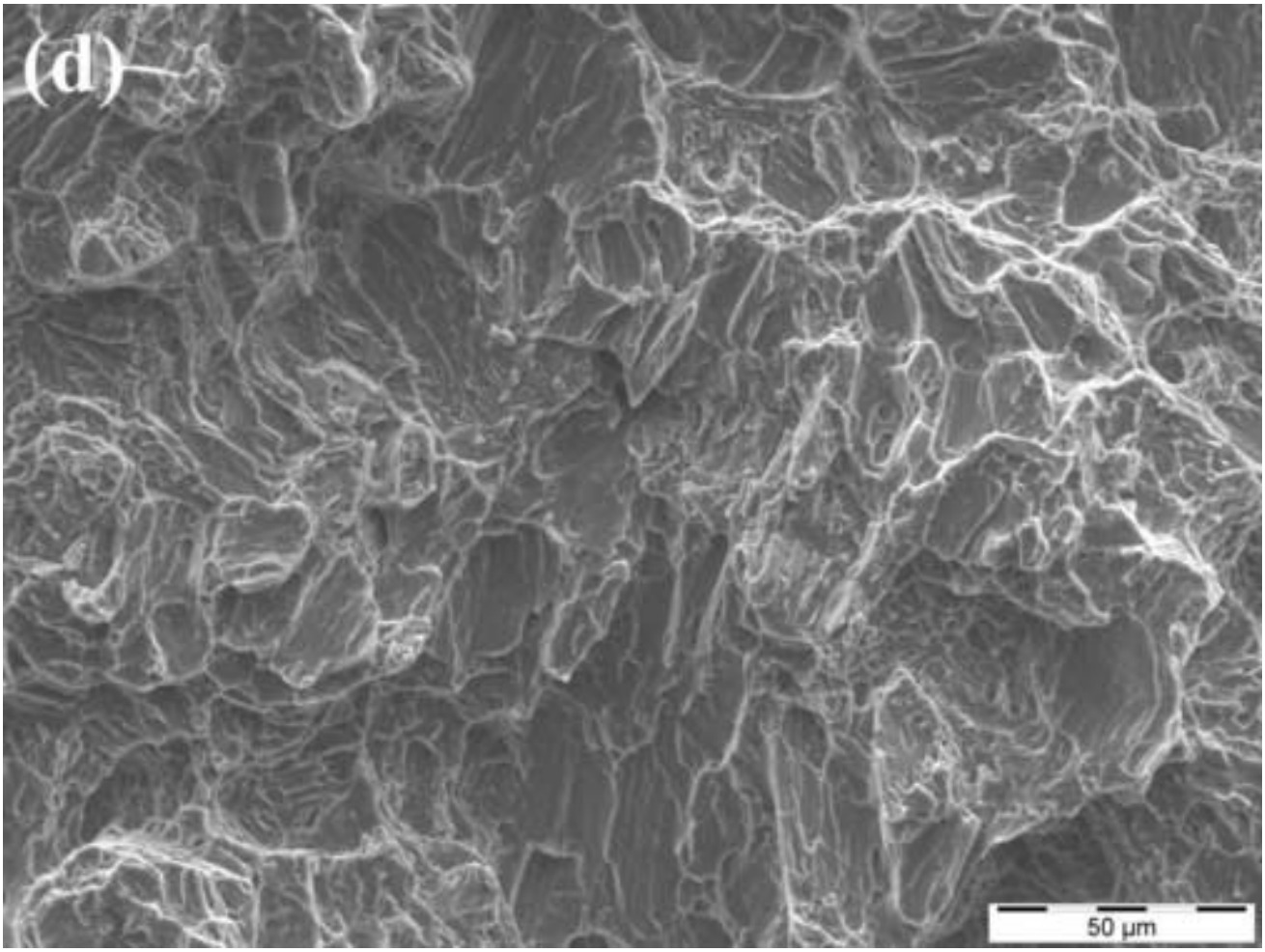

Figure 8a
Click here to download high resolution image

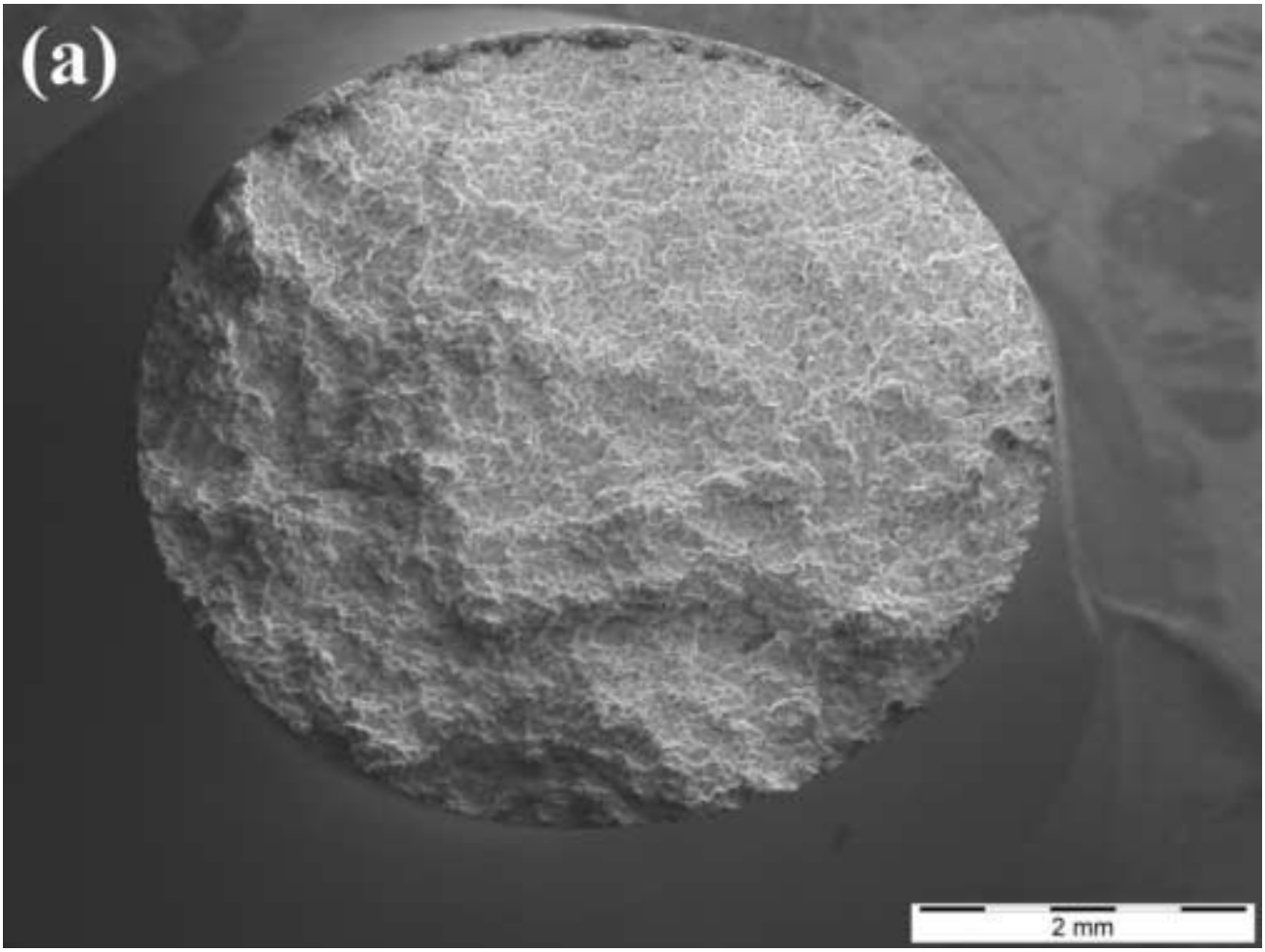

Figure 8b
Click here to download high resolution image

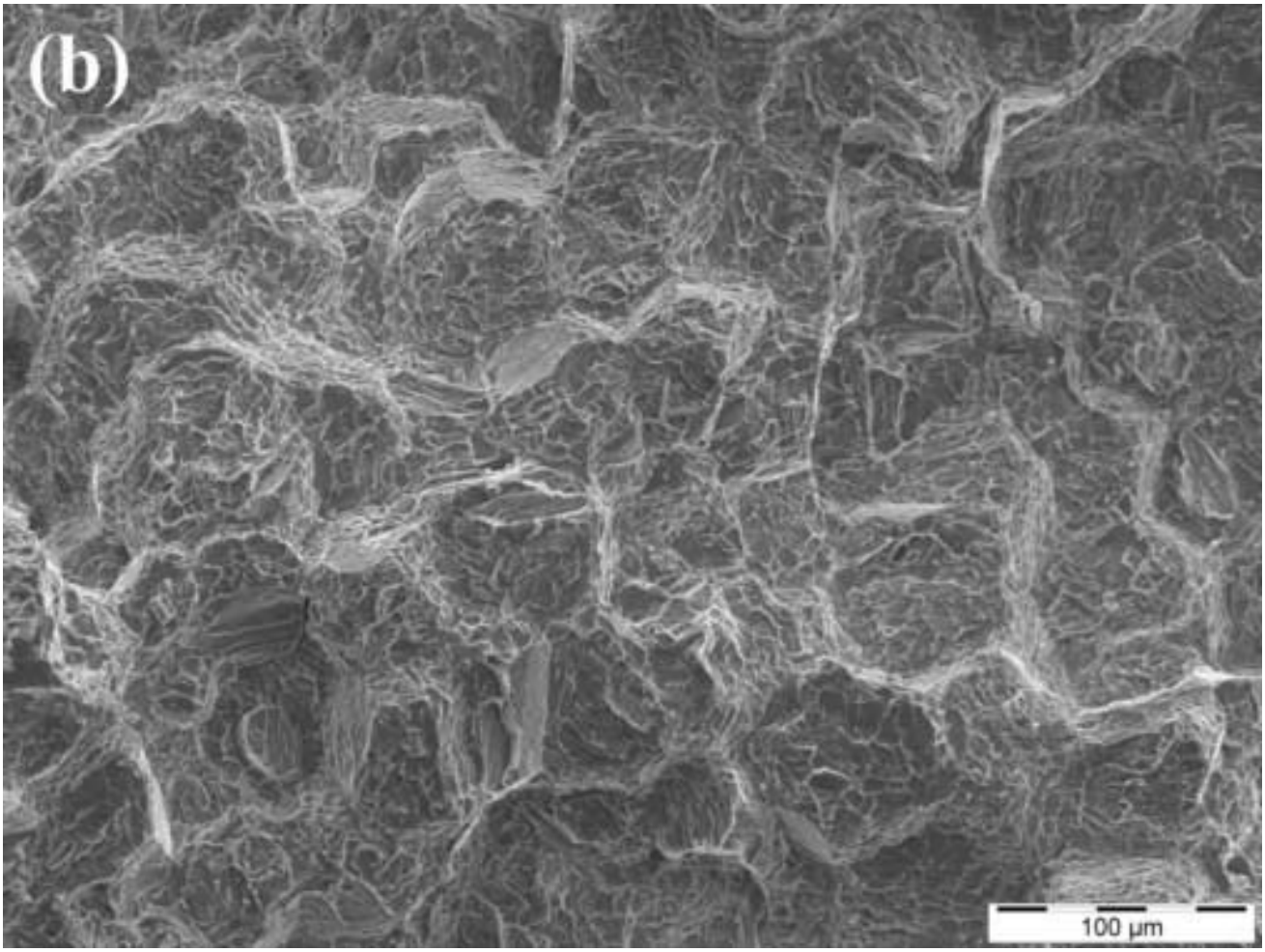

Figure 8c
Click here to download high resolution image

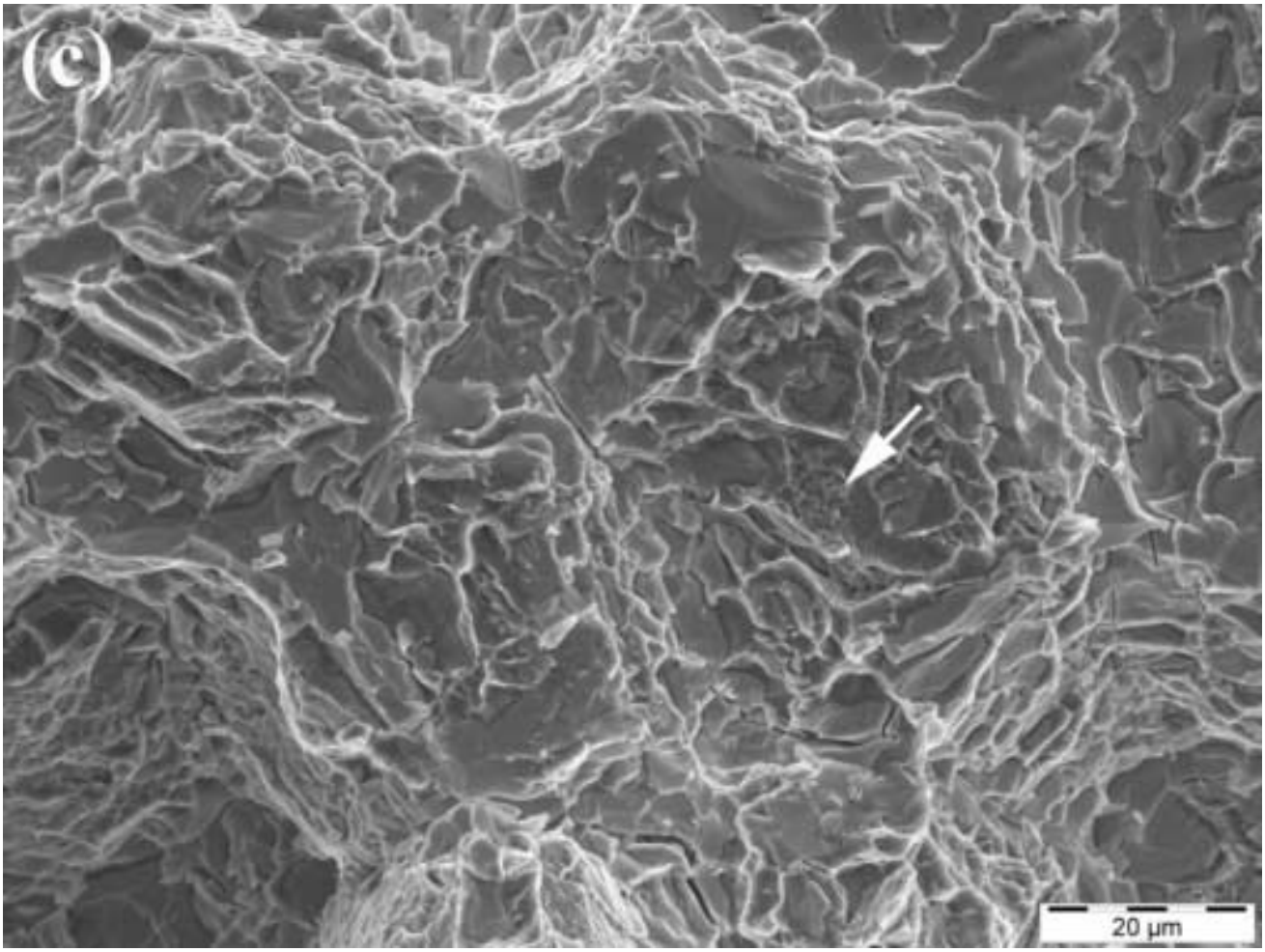

Figure 9a
Click here to download high resolution image

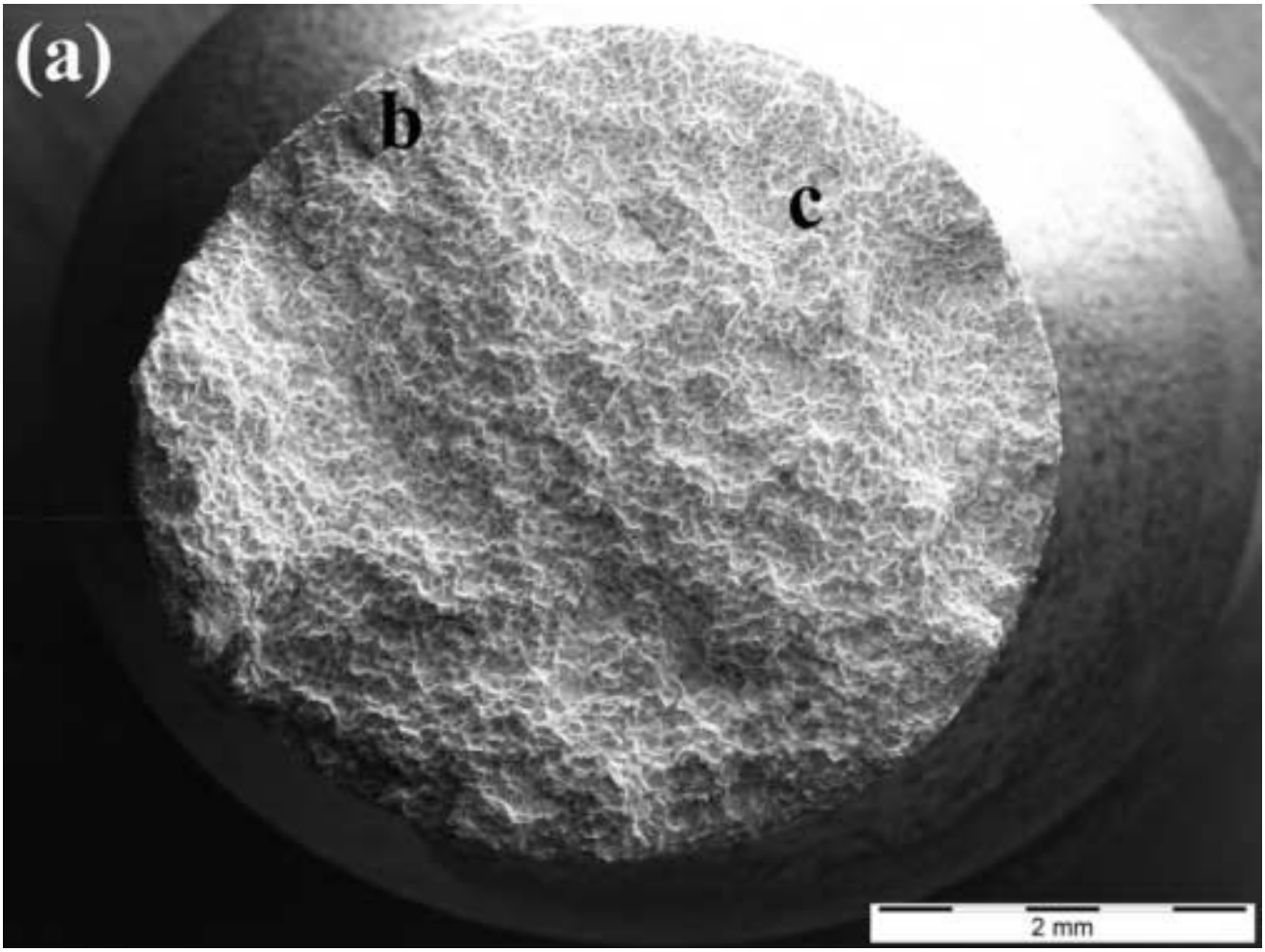

Figure 9b
Click here to download high resolution image

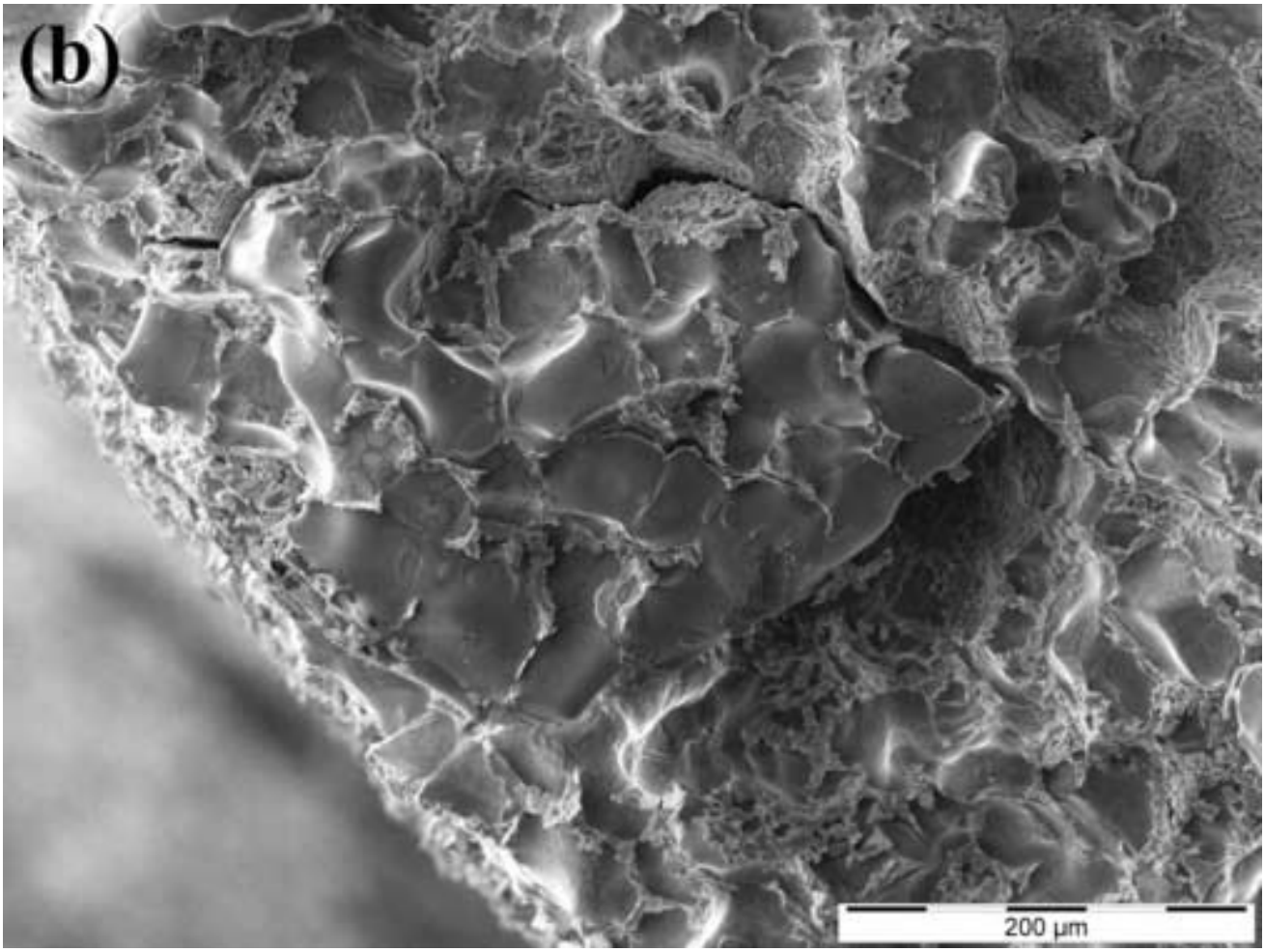

Figure 9c
Click here to download high resolution image

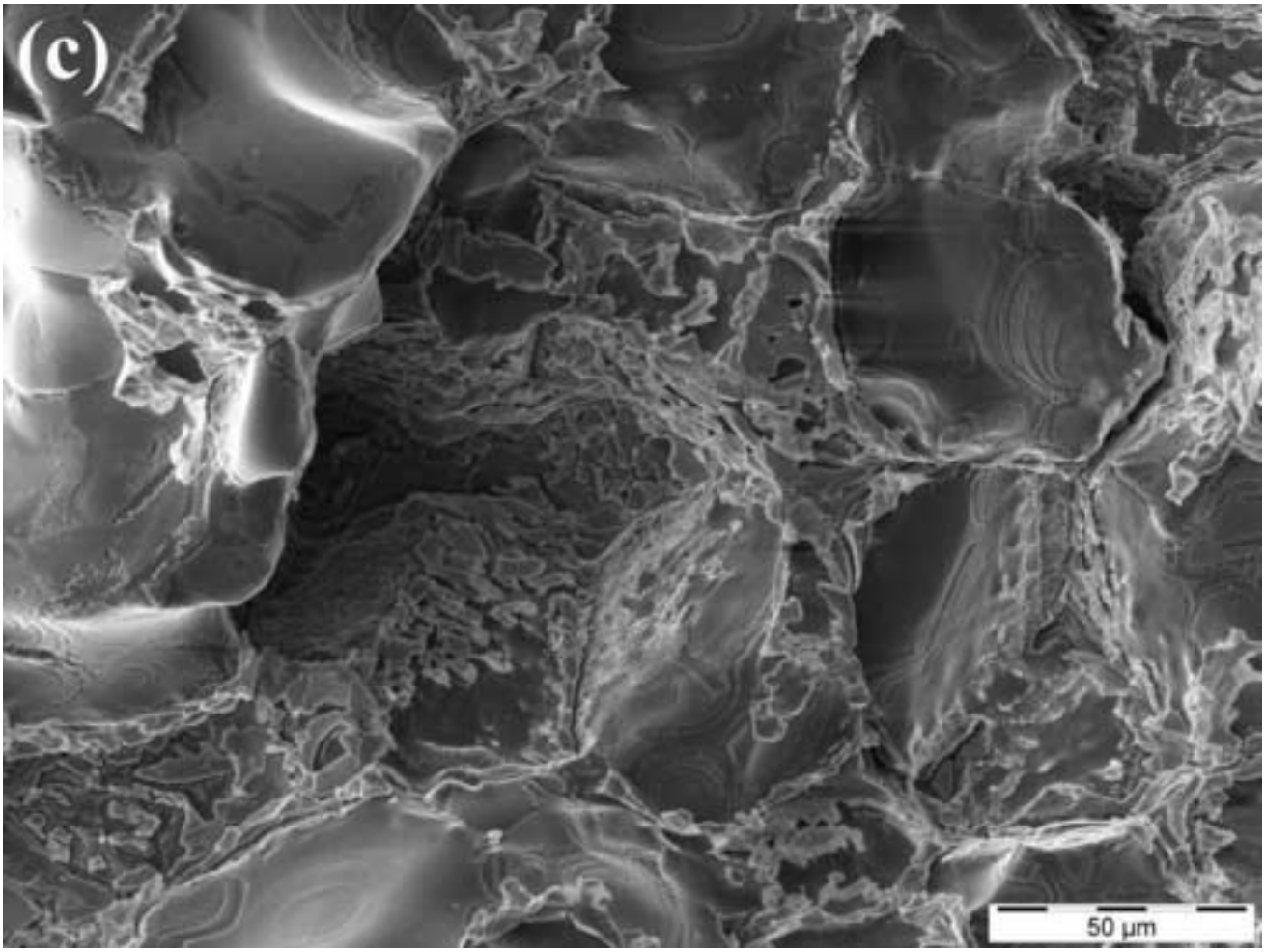

Figure 10a
Click here to download high resolution image

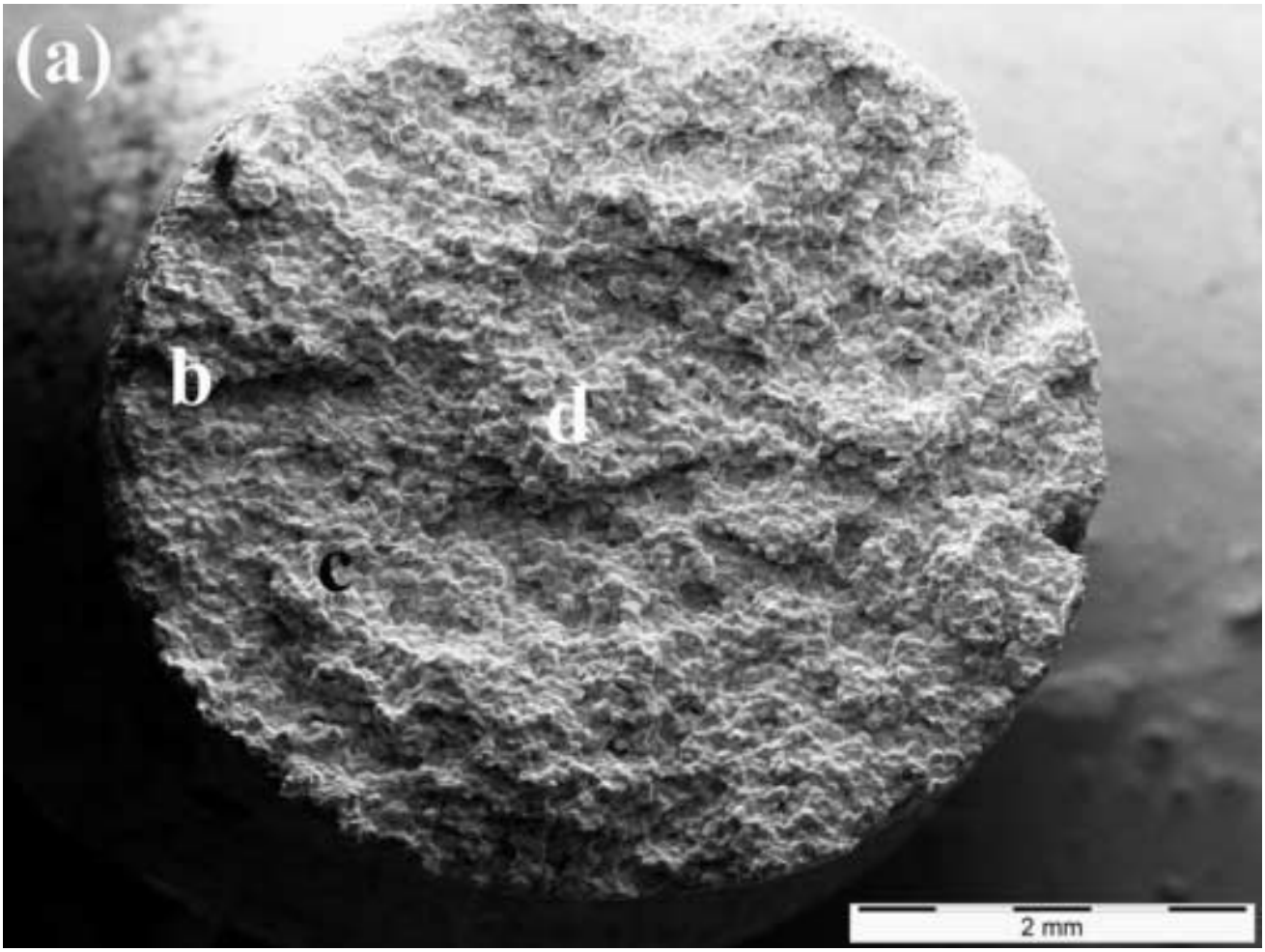

Figure 10b
Click here to download high resolution image

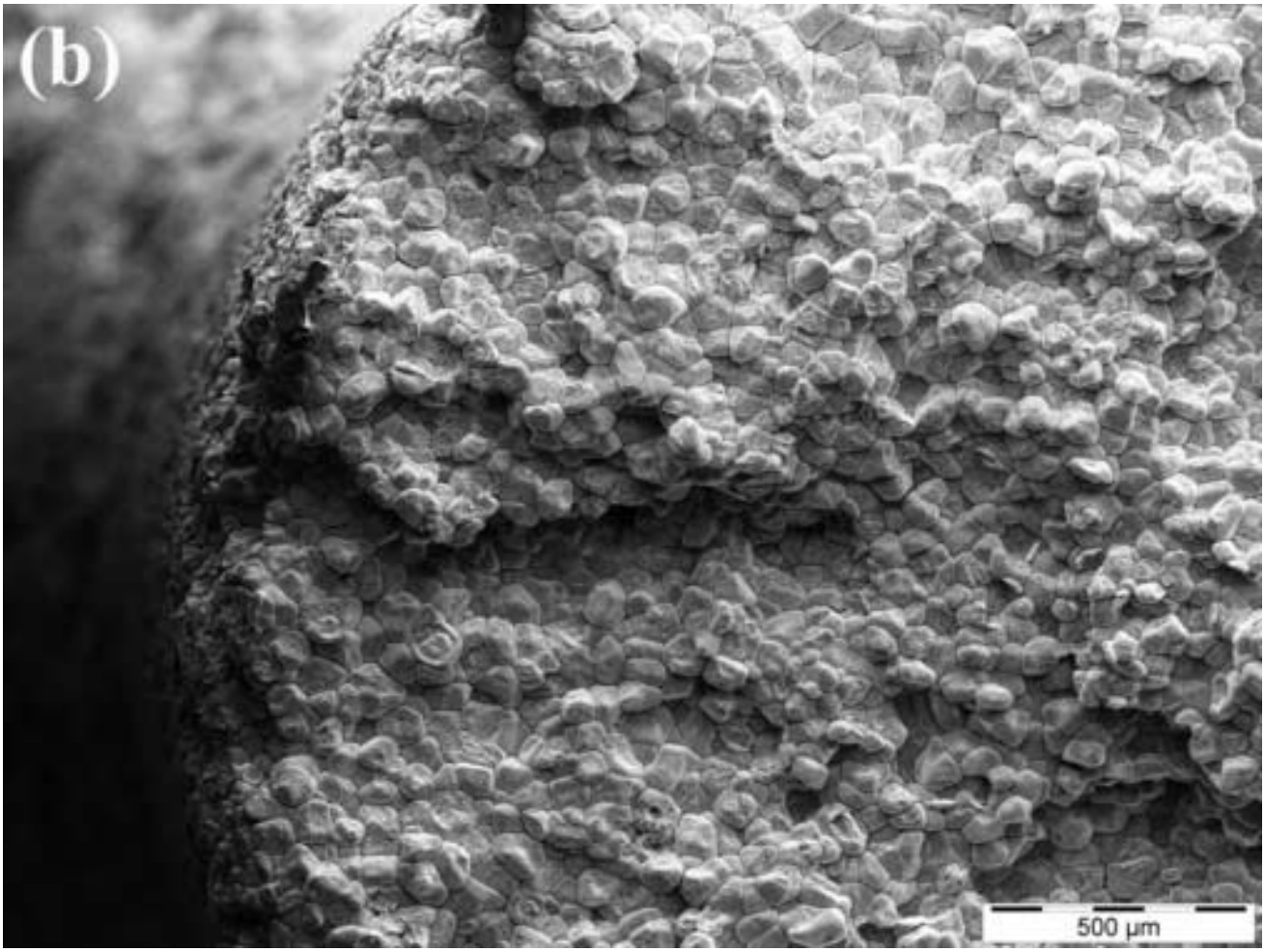

Figure 10c
Click here to download high resolution image

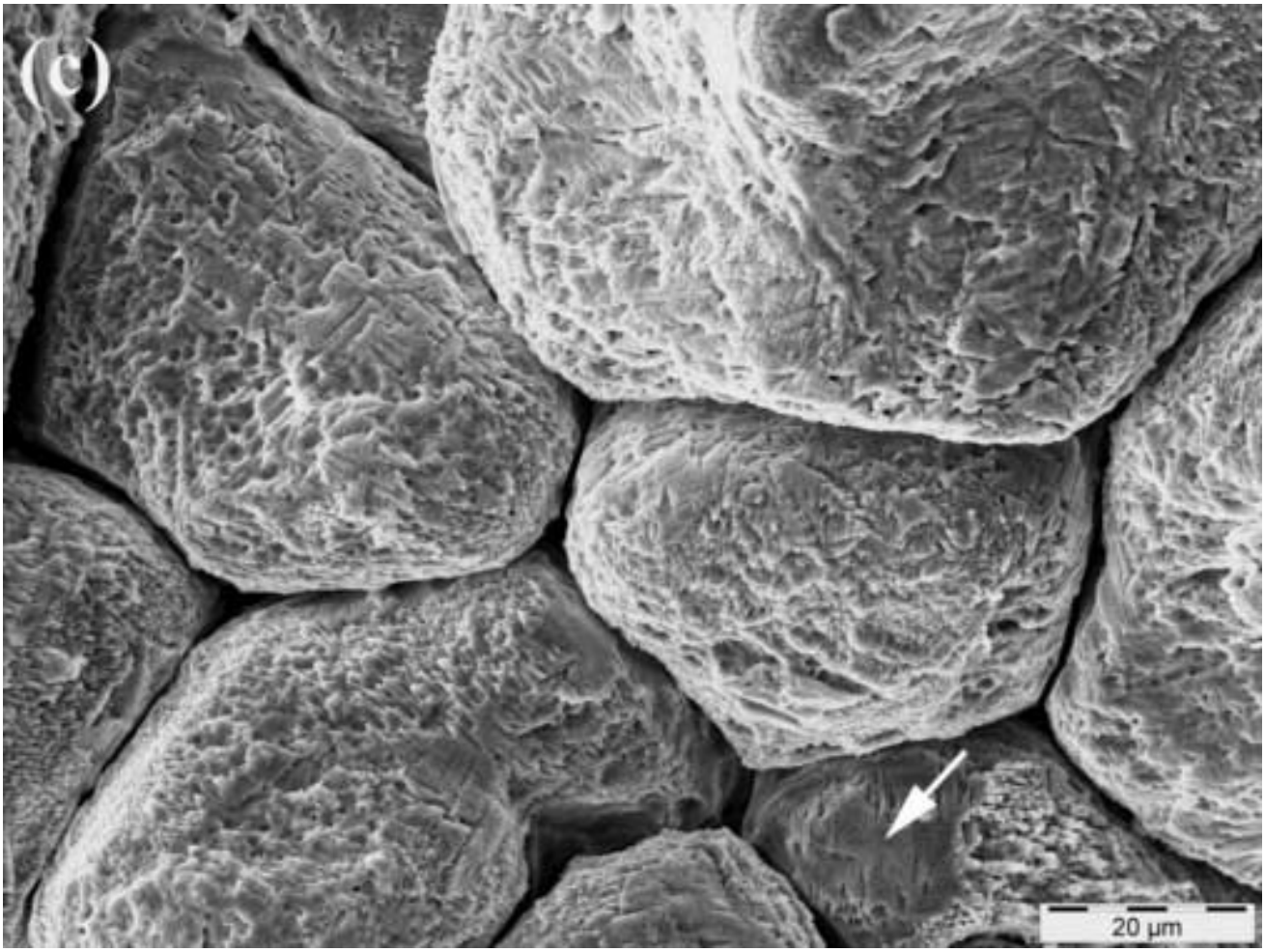

Figure 10d
Click here to download high resolution image

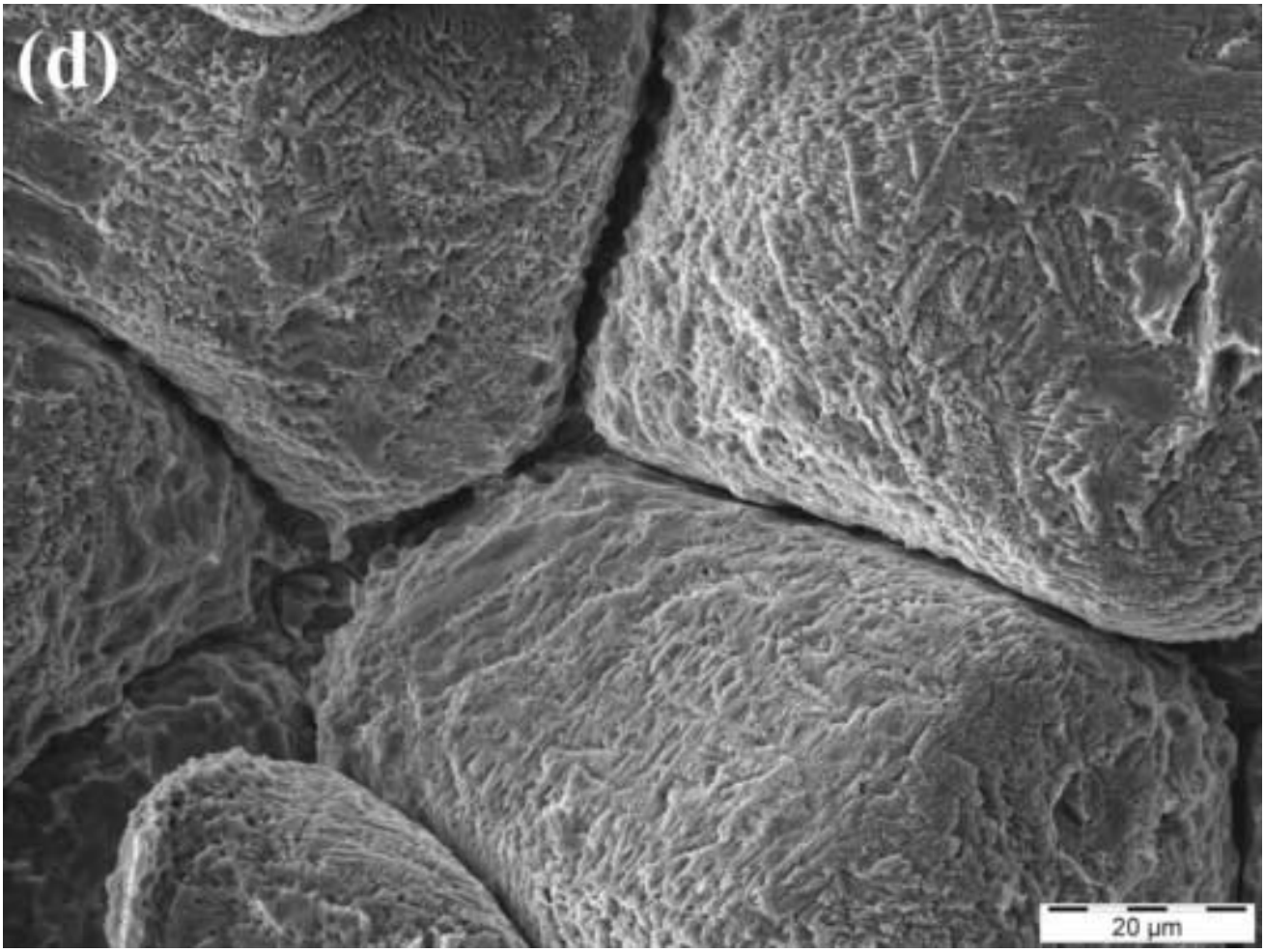

Figure 11a
Click here to download high resolution image

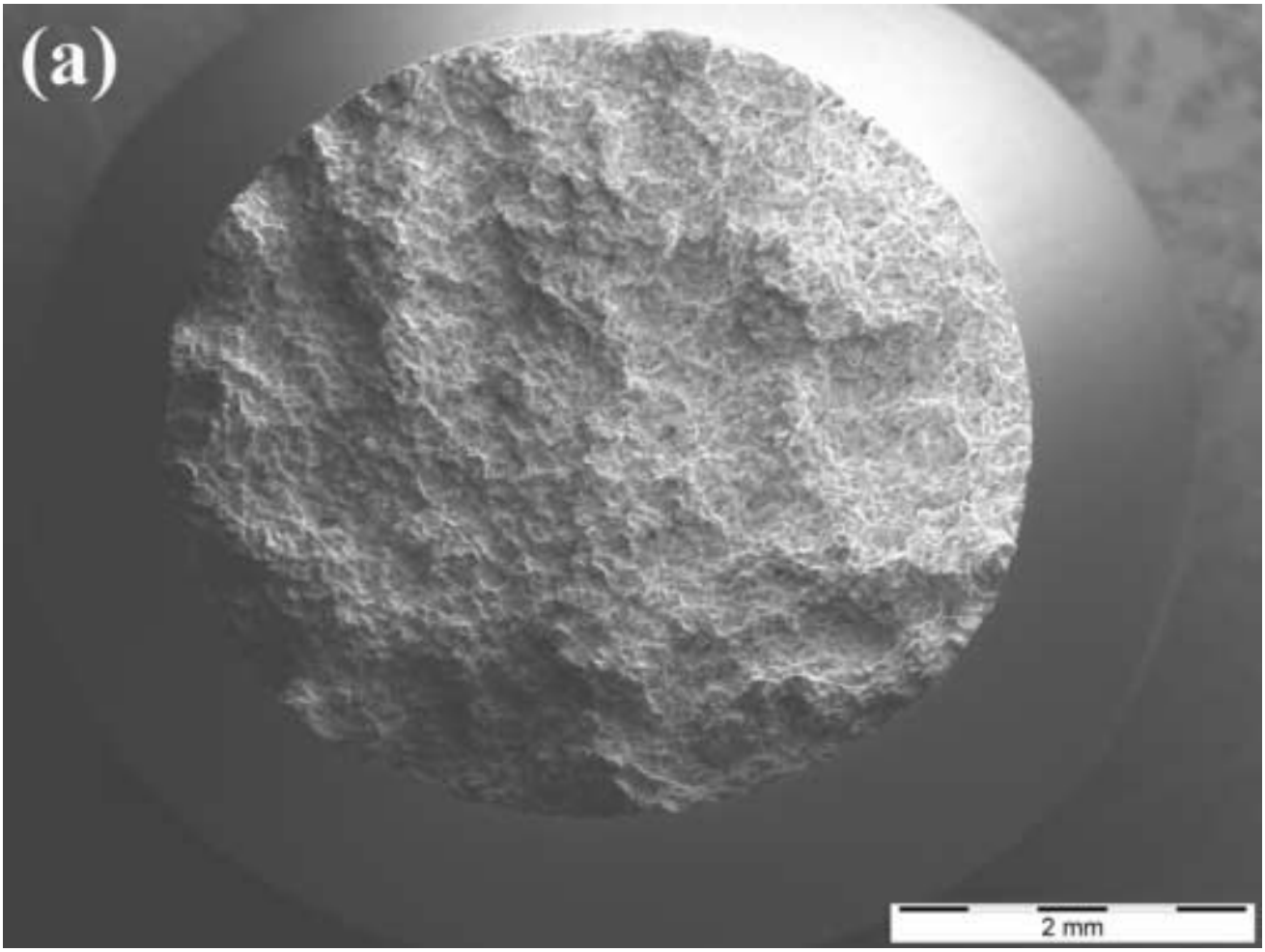

Figure 11b
Click here to download high resolution image

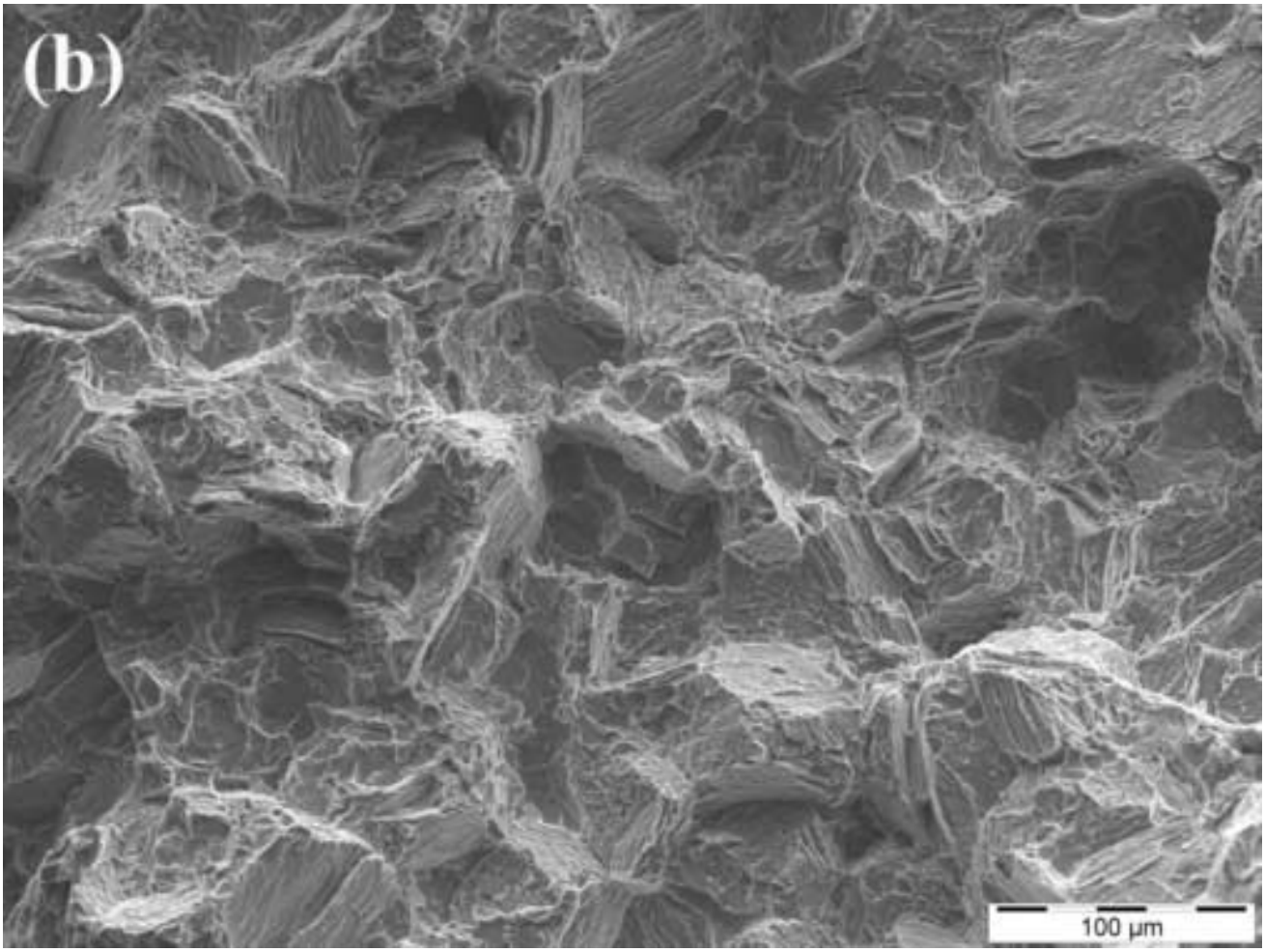

Figure 11c
Click here to download high resolution image

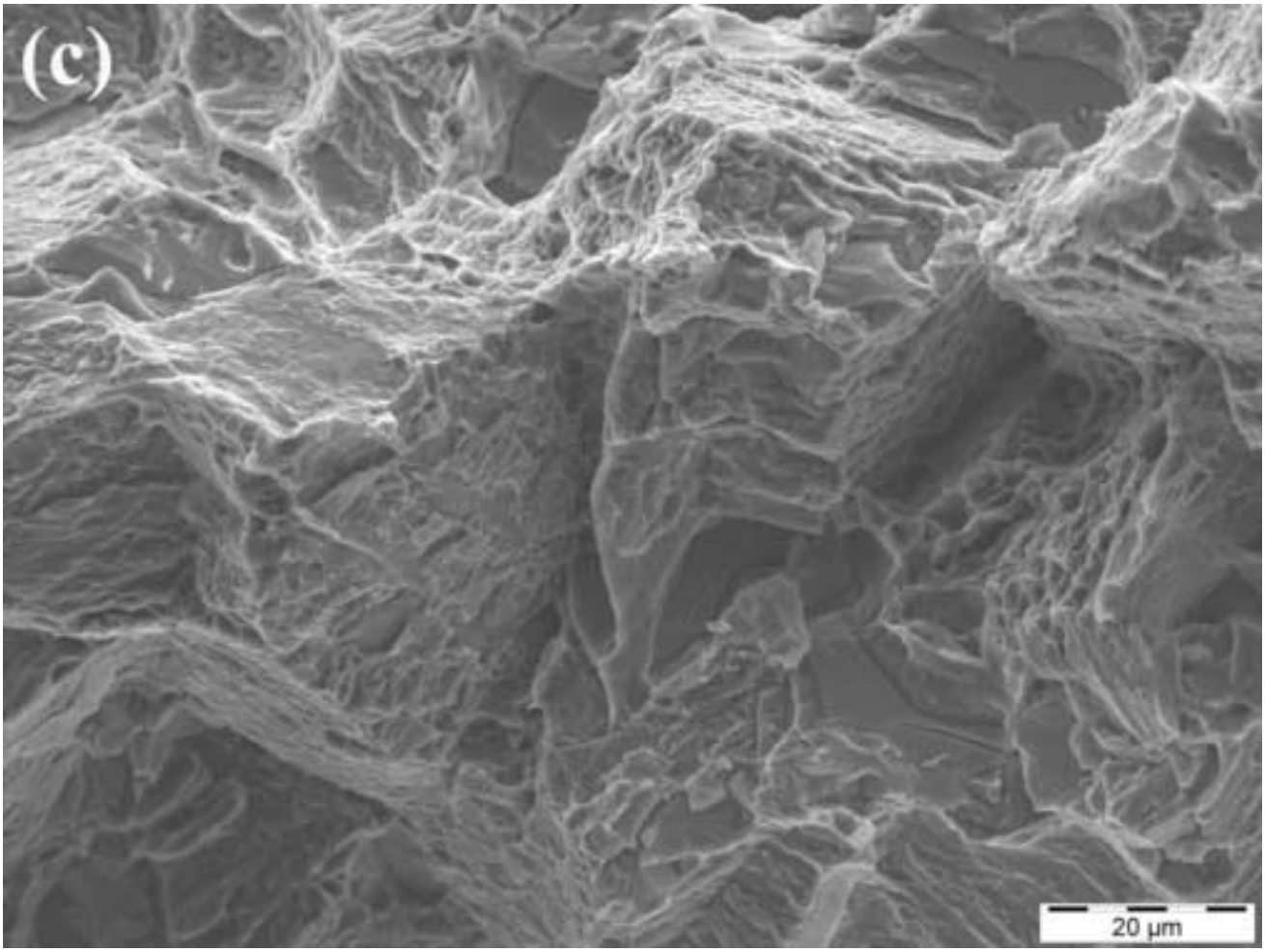

Figure 12a
Click here to download high resolution image

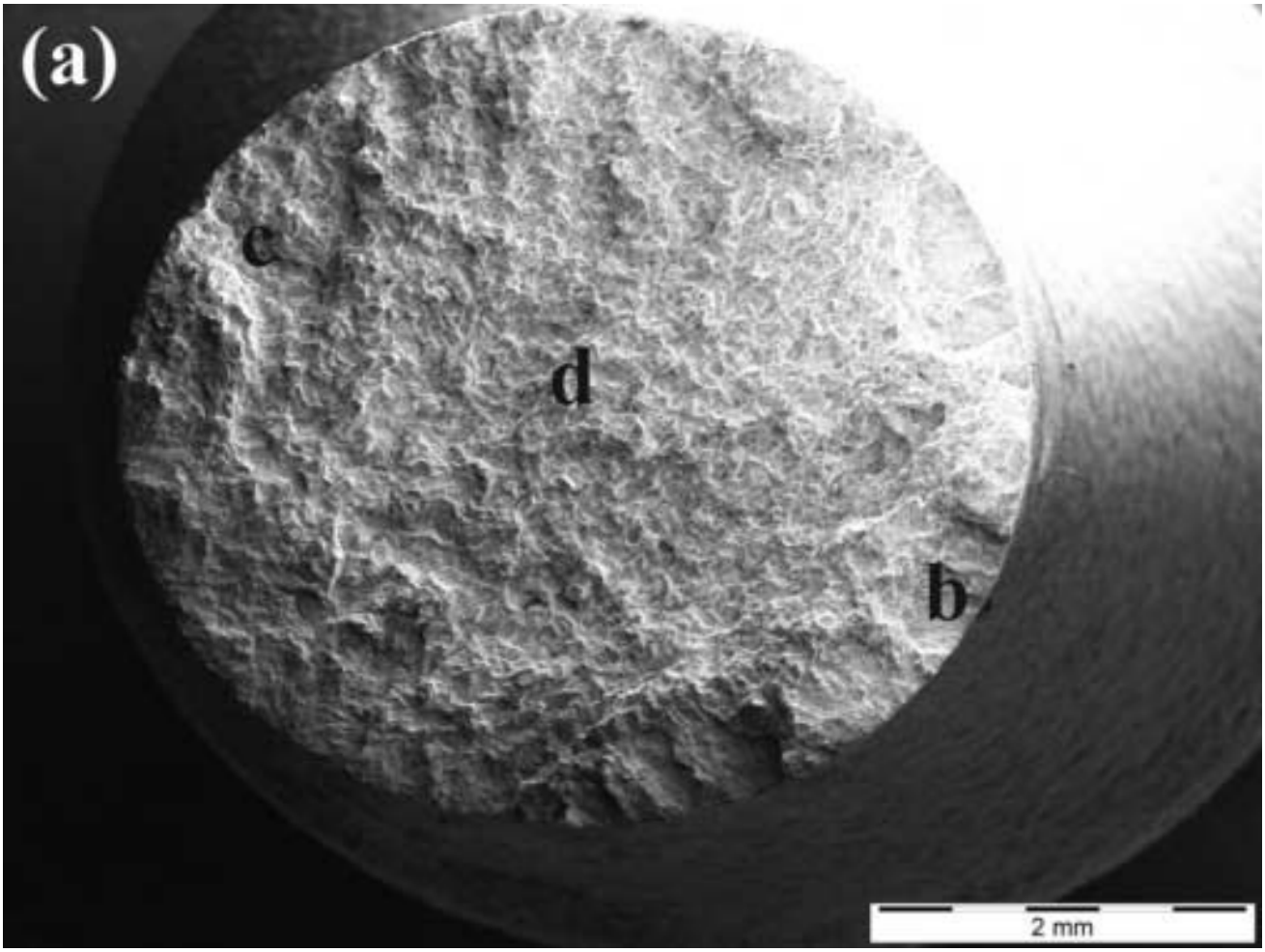

Figure 12b
Click here to download high resolution image

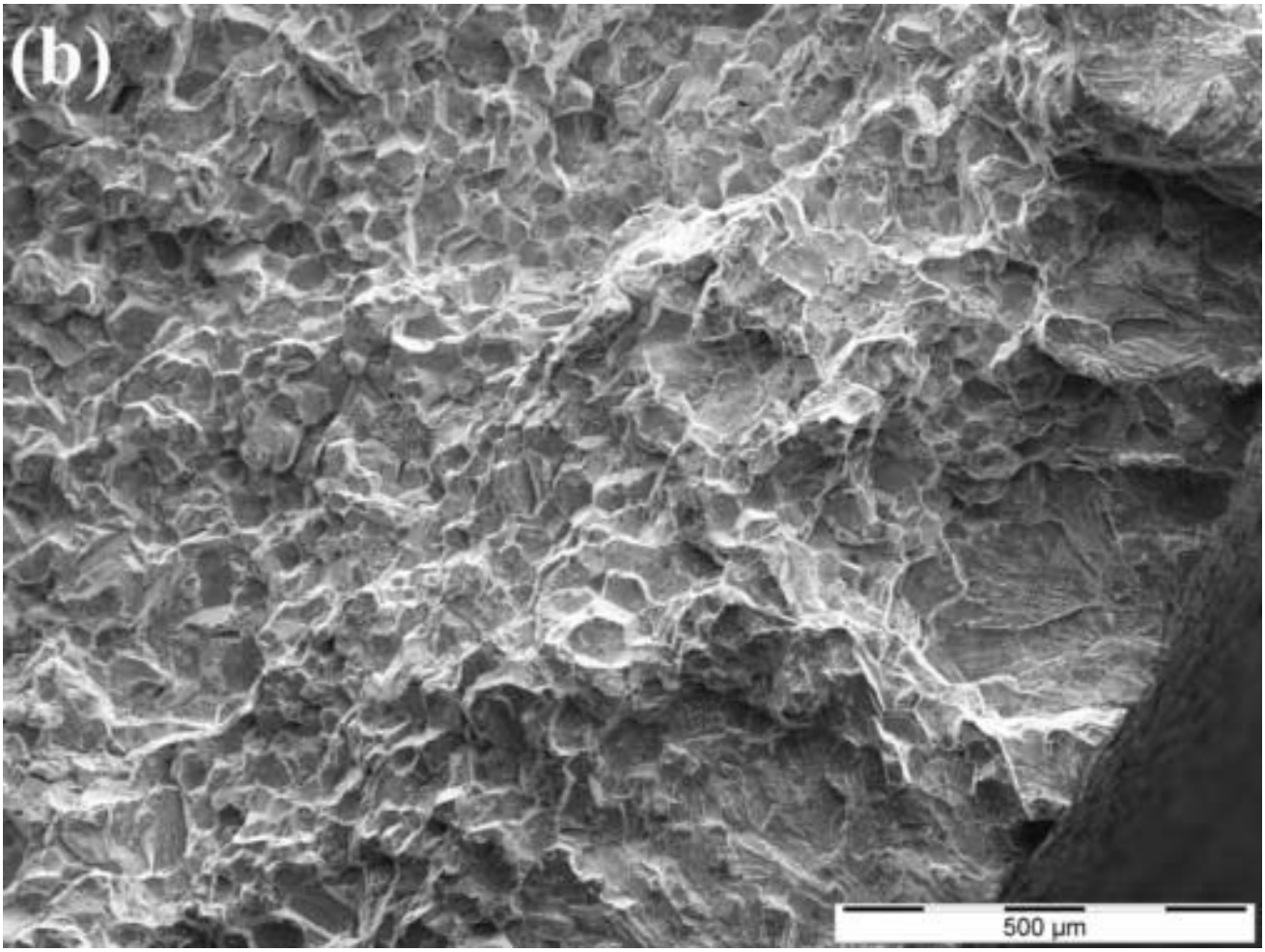

Figure 12c
Click here to download high resolution image

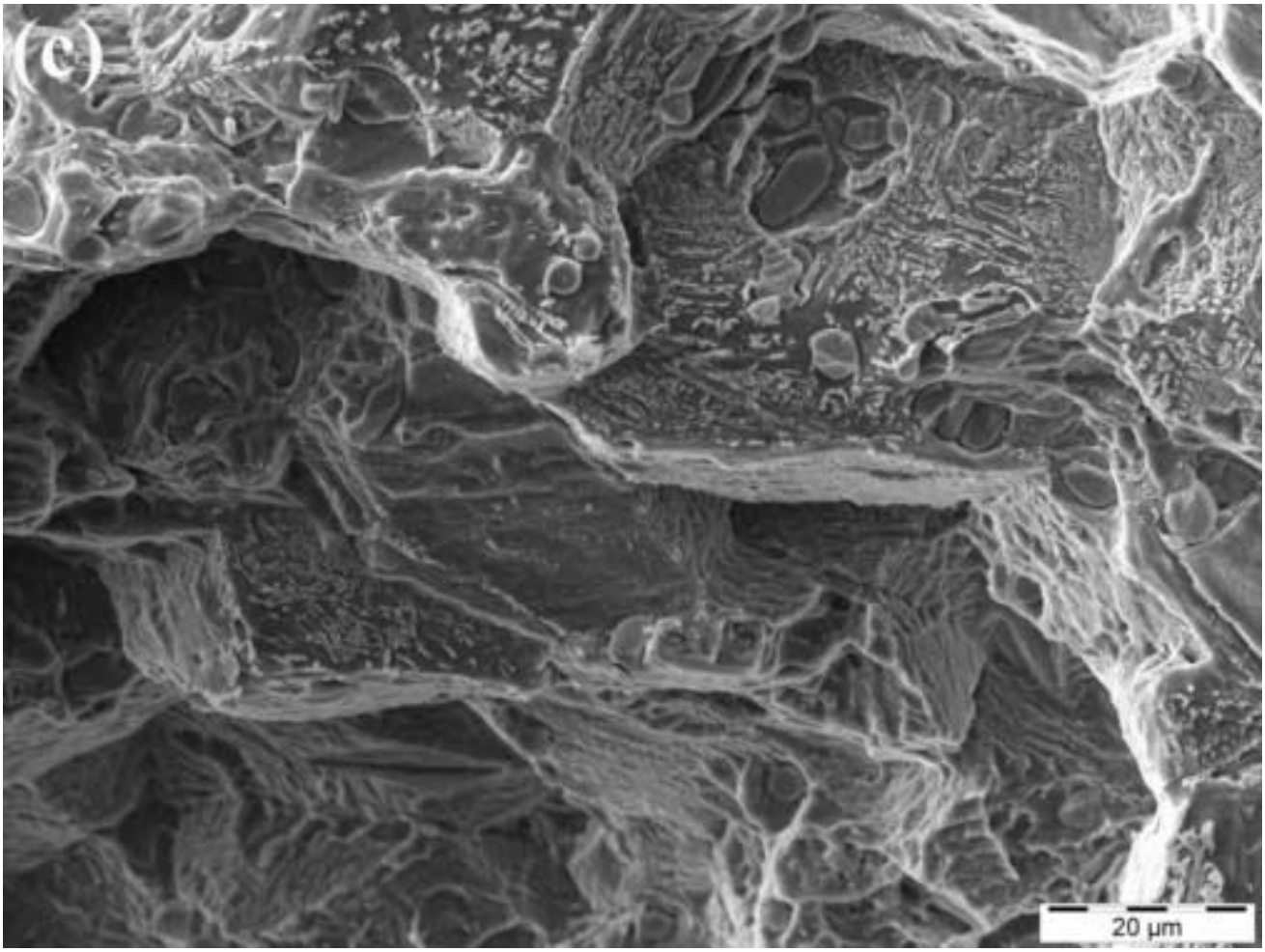

Figure 12d
Click here to download high resolution image

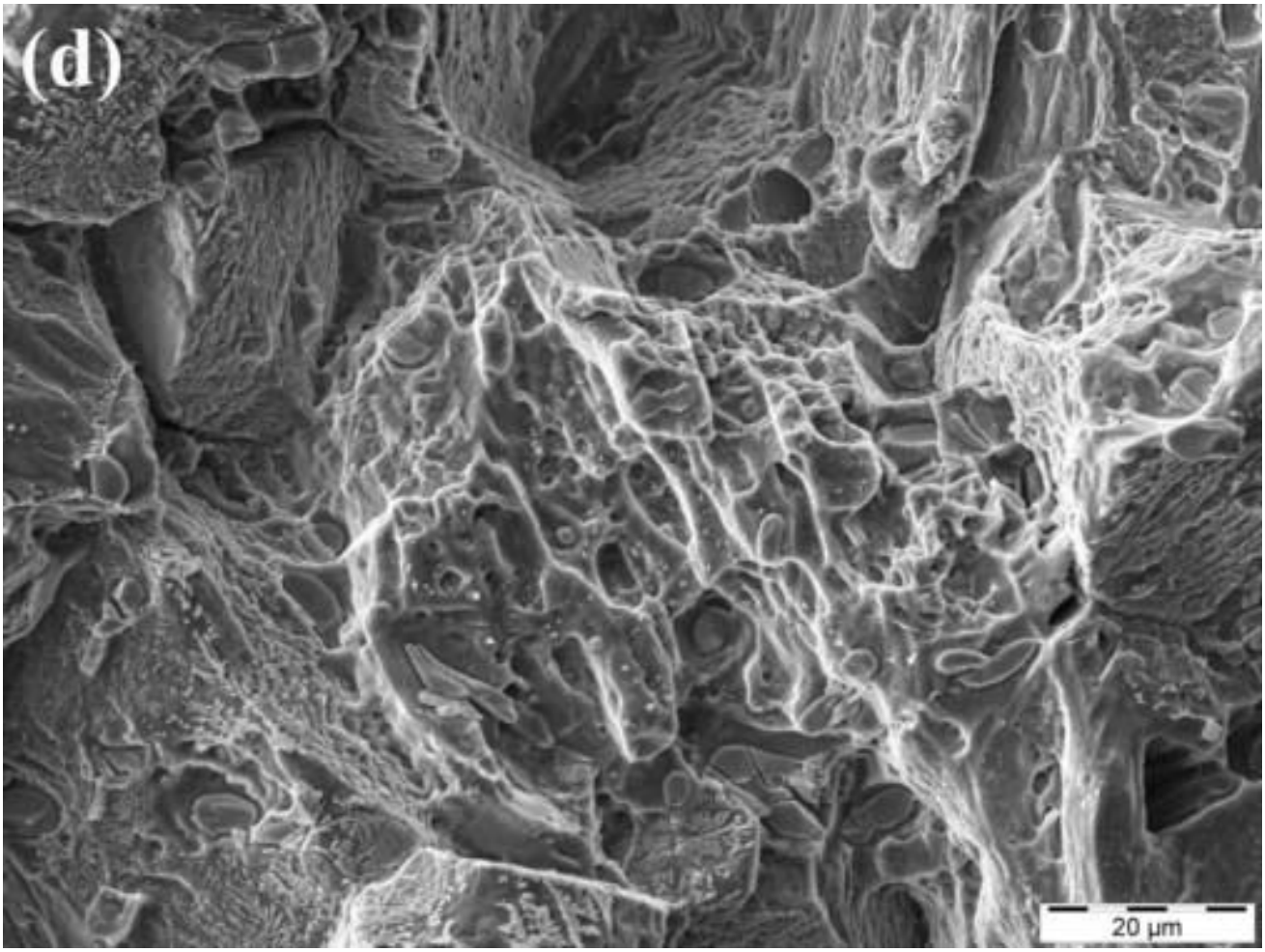

Figure 13a
Click here to download high resolution image

Figure 13b
Click here to download high resolution image

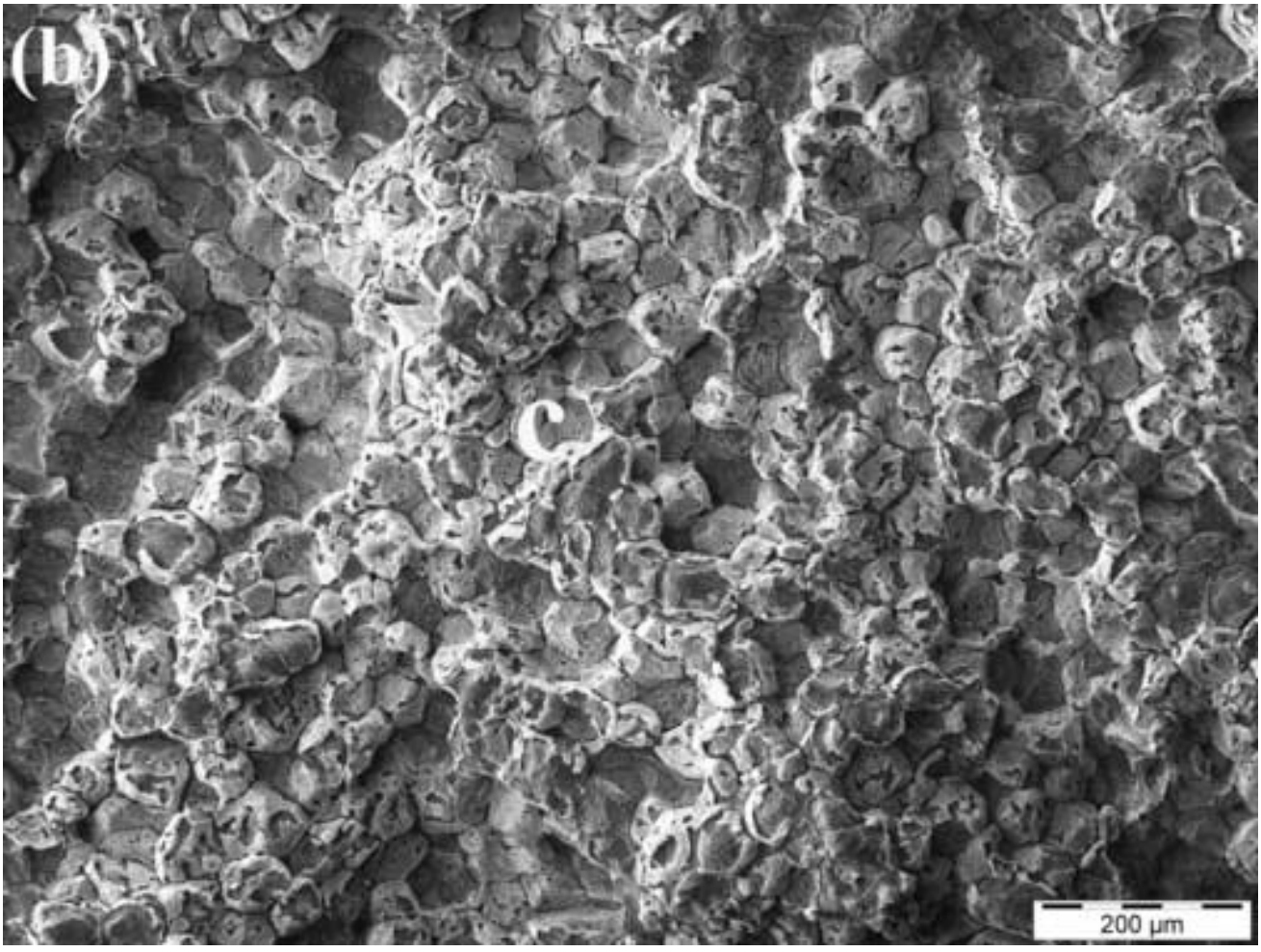

Figure 13c
Click here to download high resolution image

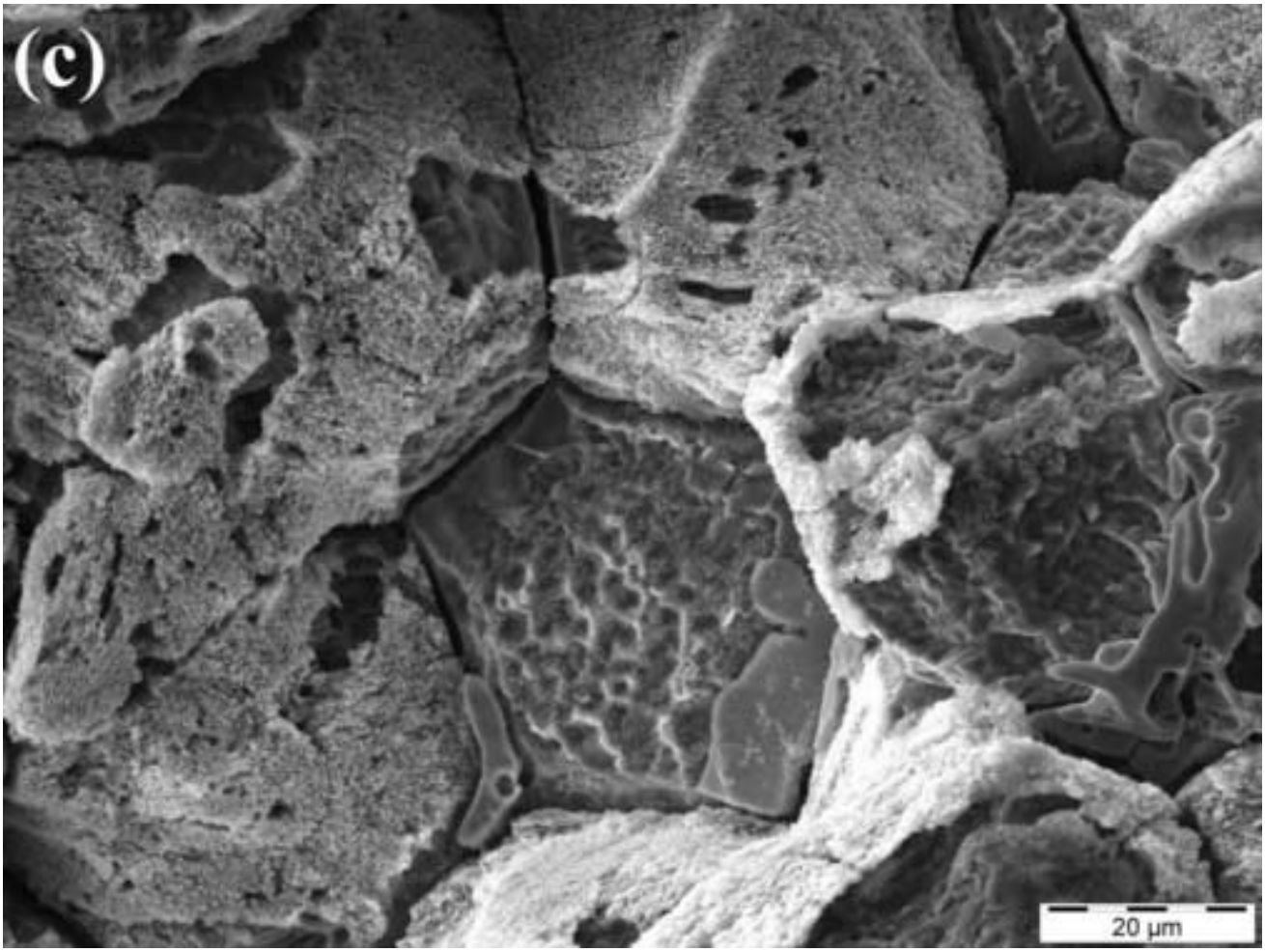

Figure 13d
Click here to download high resolution image

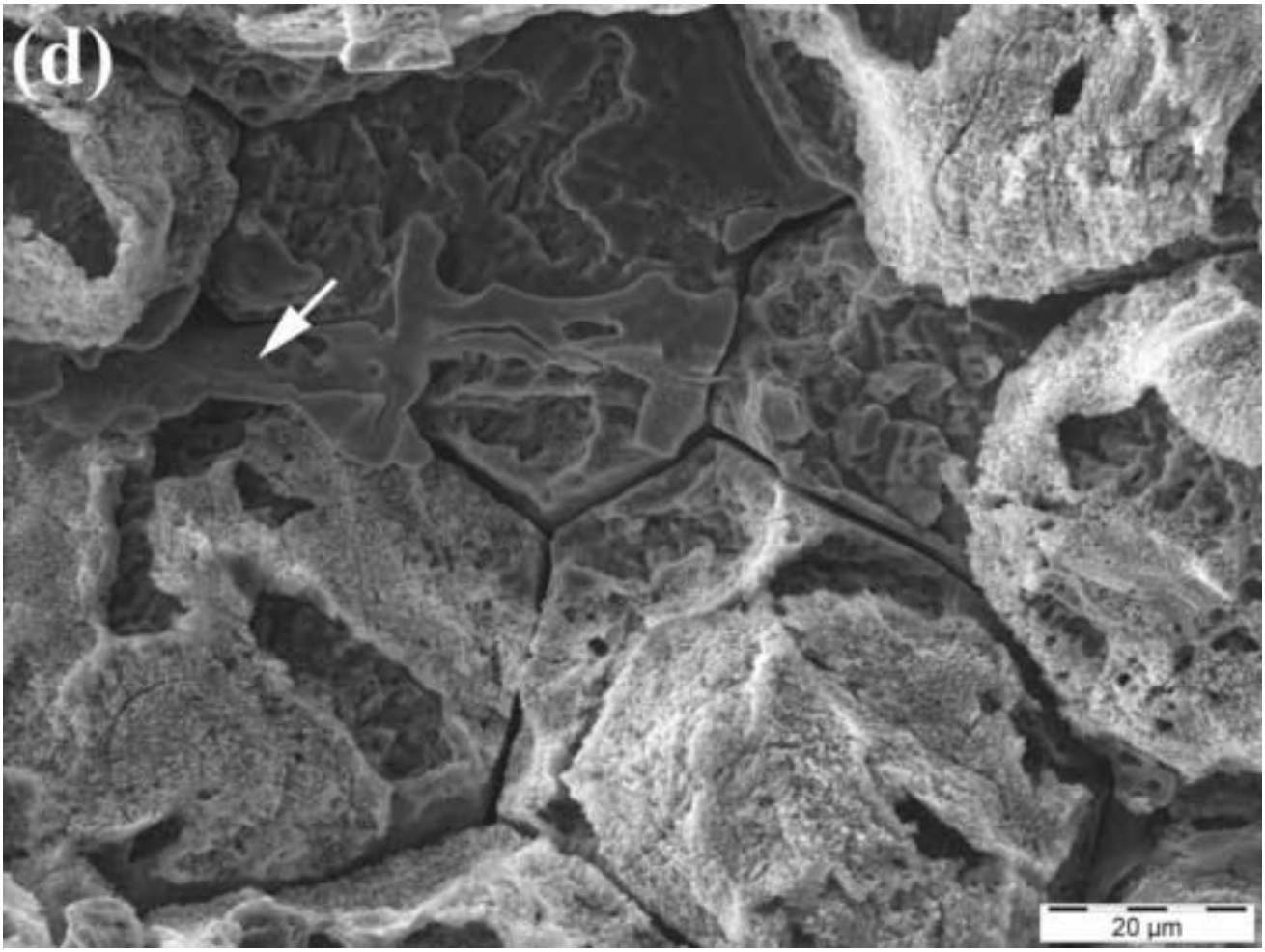

Figure 14a
Click here to download high resolution image

Figure 14b
Click here to download high resolution image

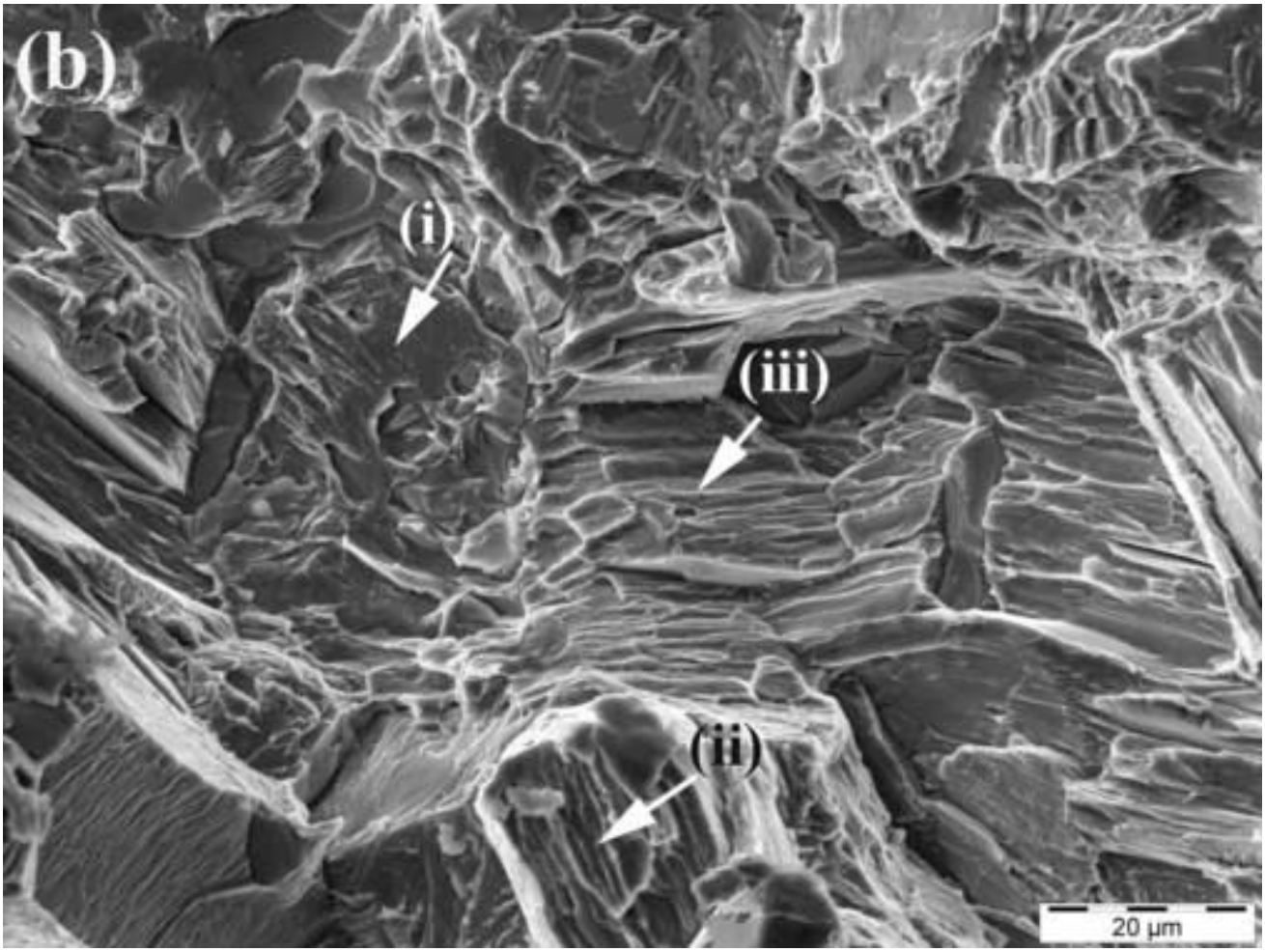

Figure 15a
Click here to download high resolution image

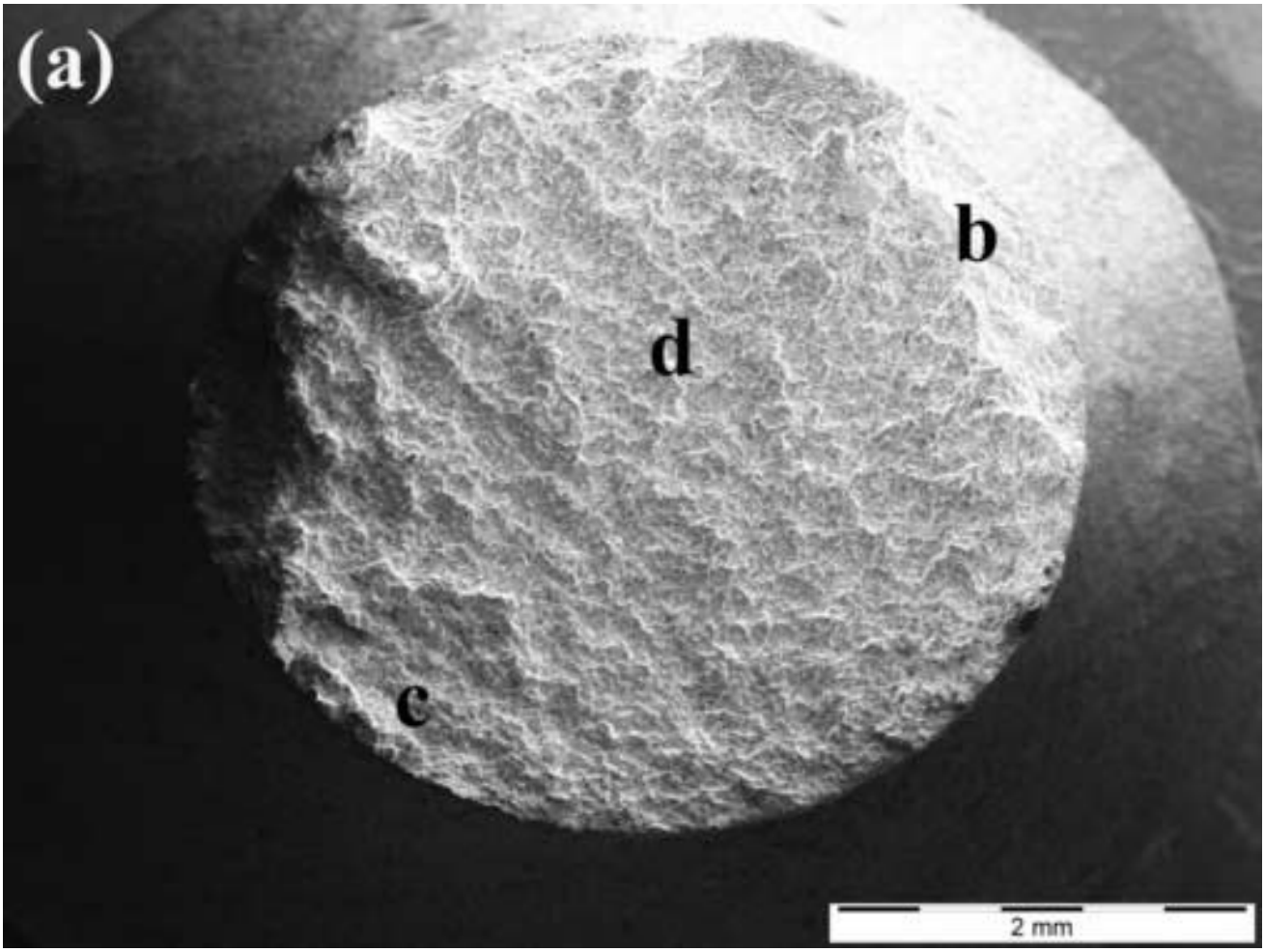

Figure 15b
Click here to download high resolution image

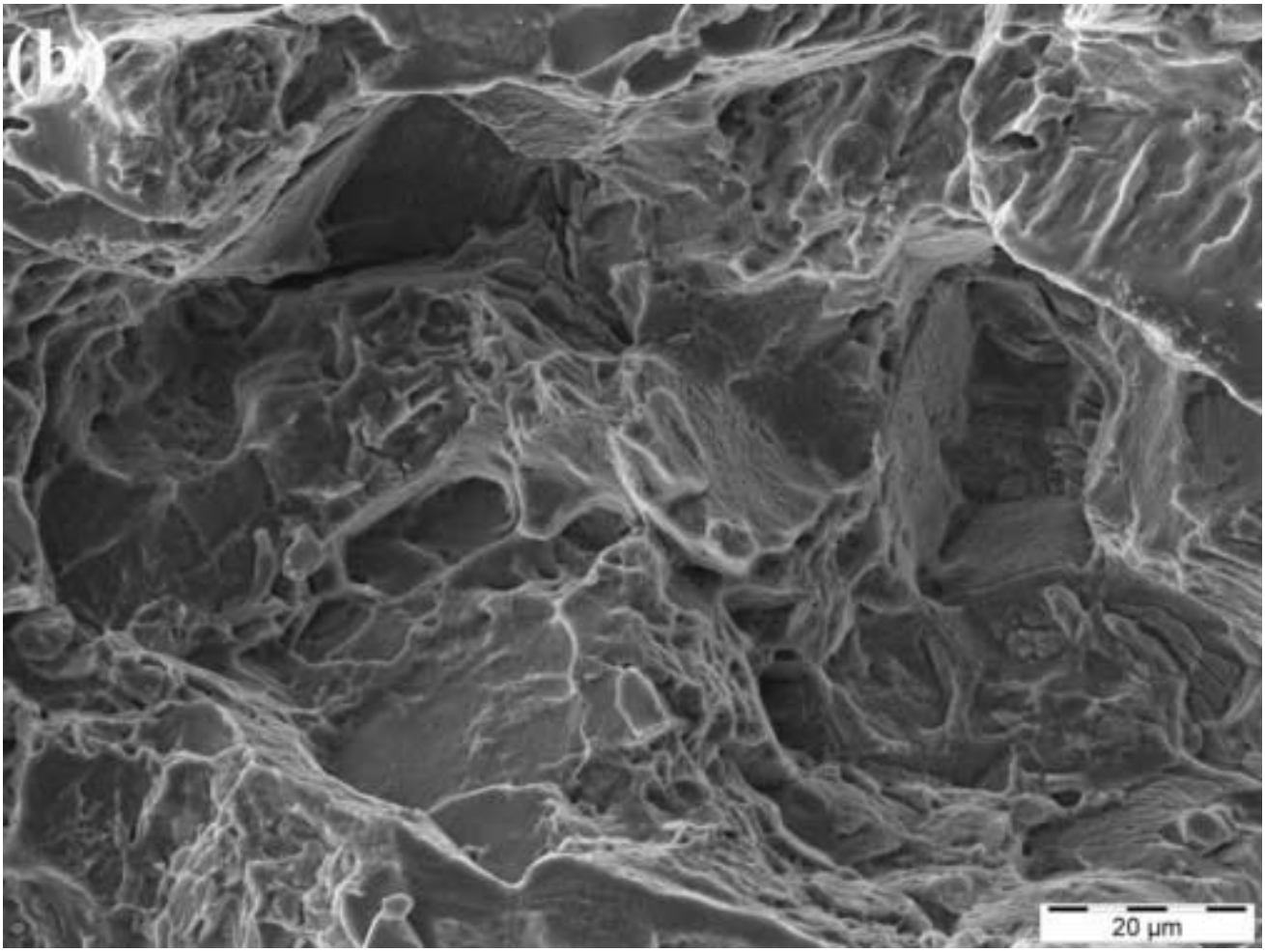

Figure 15c
Click here to download high resolution image

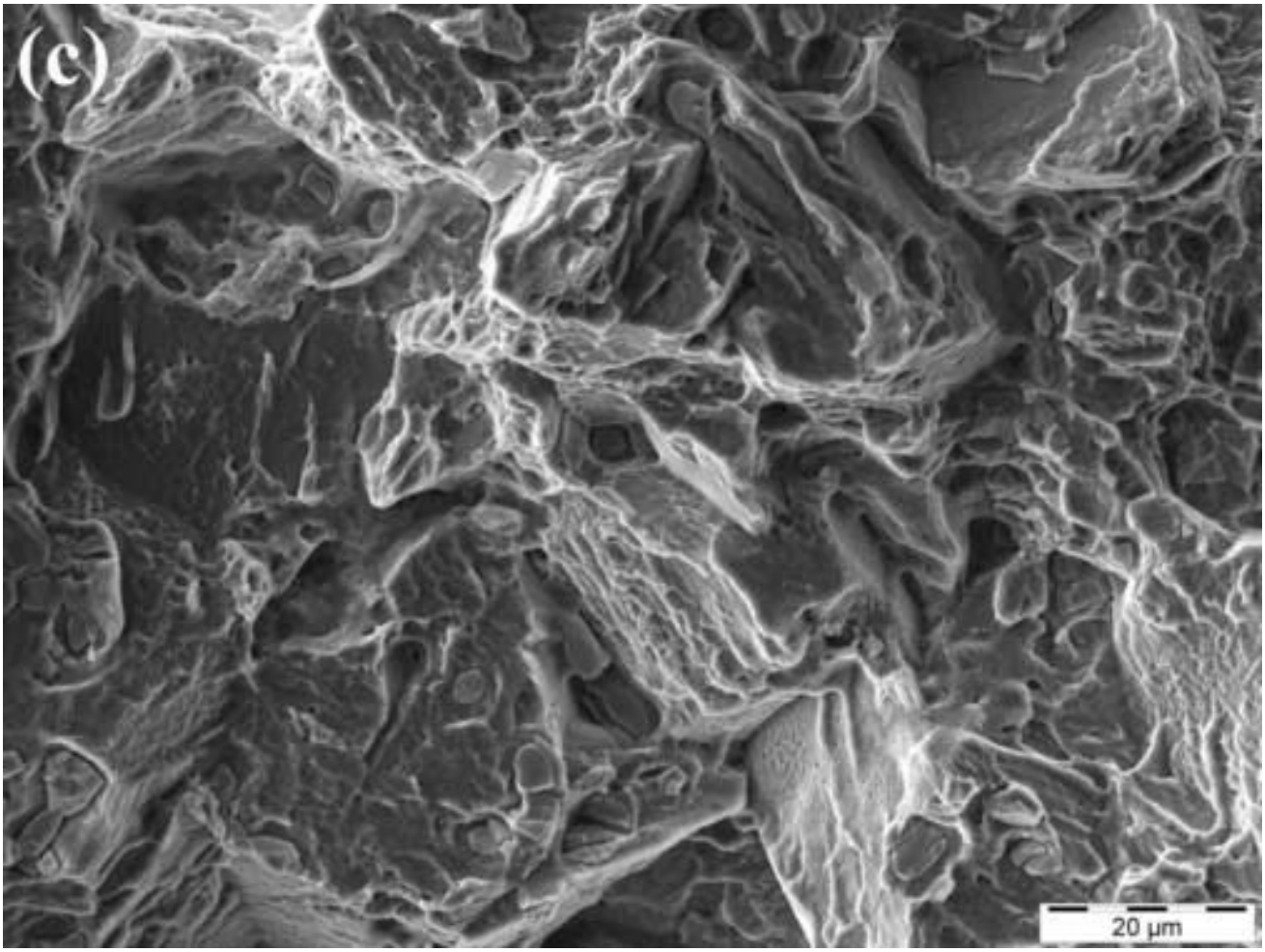

Figure 15d
Click here to download high resolution image

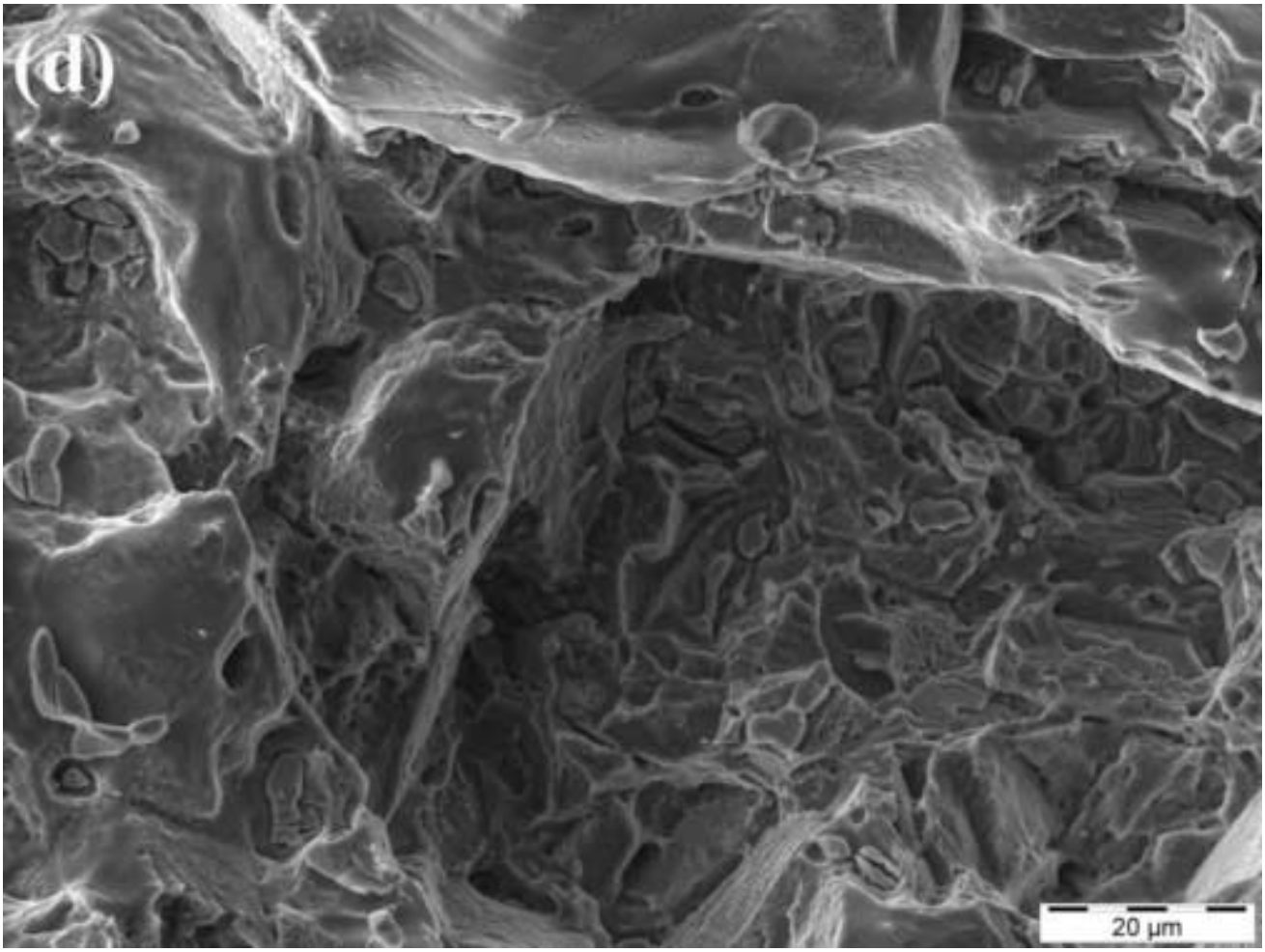

Figure 16a
Click here to download high resolution image

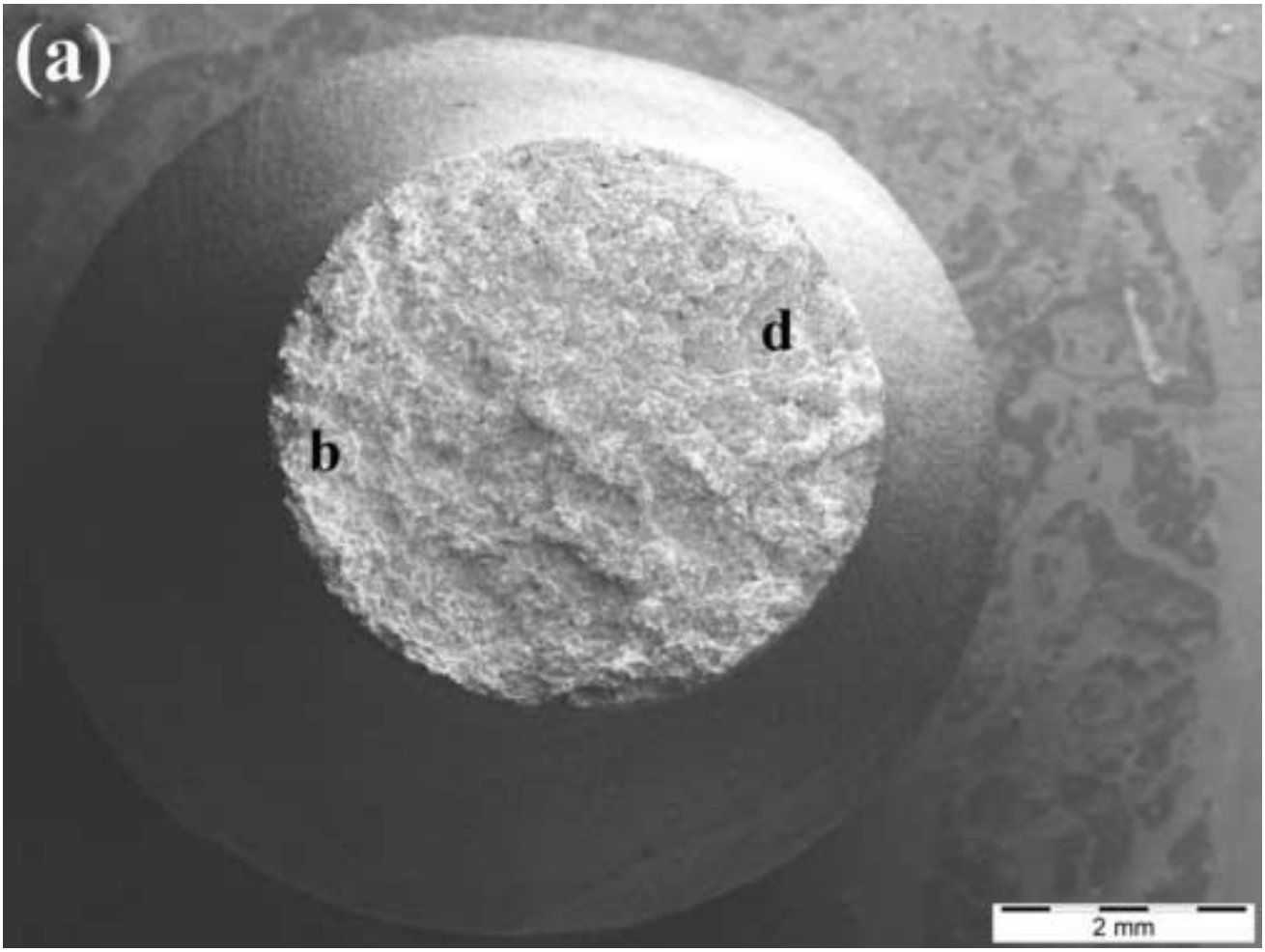

Figure 16b
Click here to download high resolution image

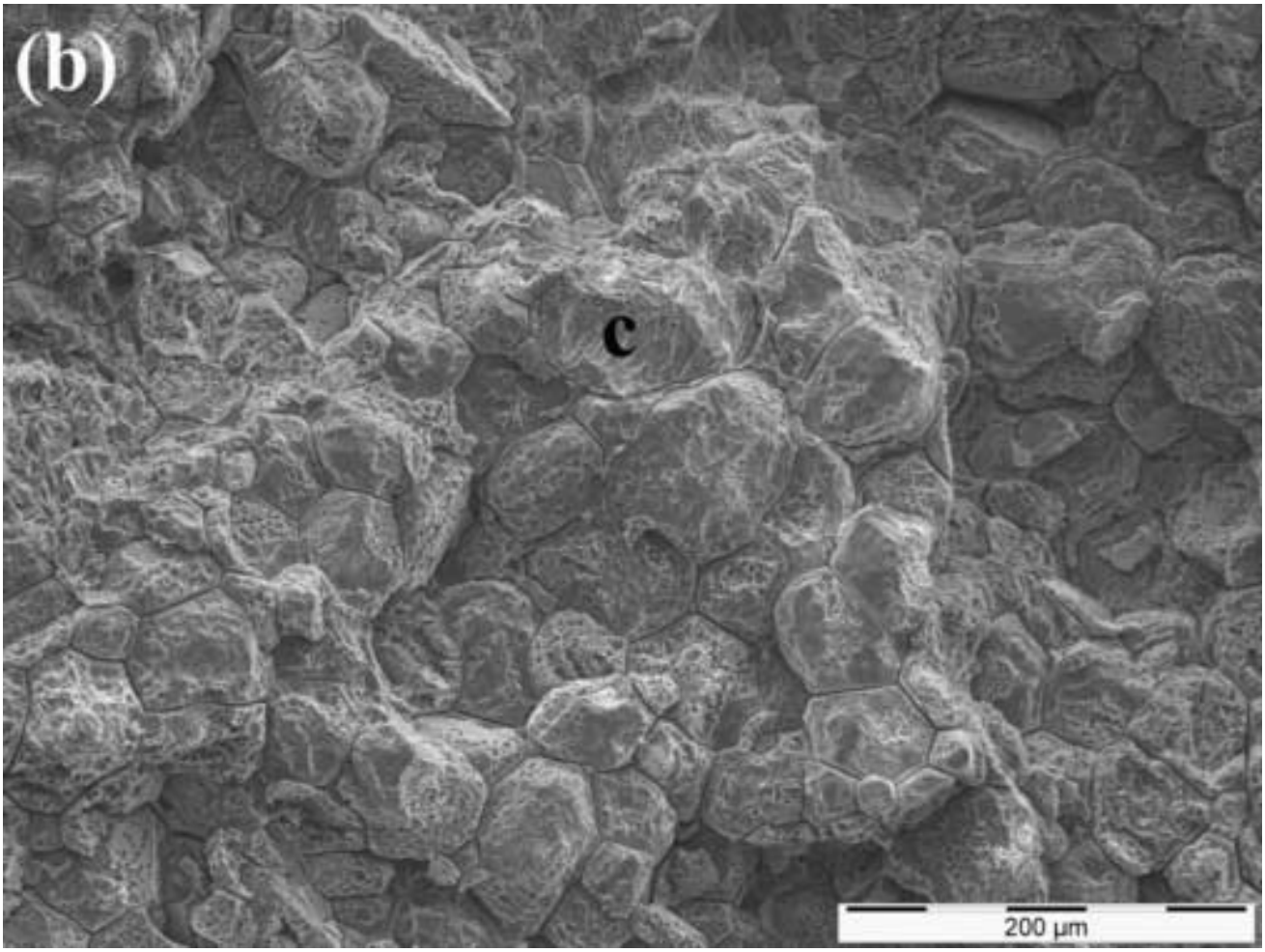

Figure 16c
Click here to download high resolution image

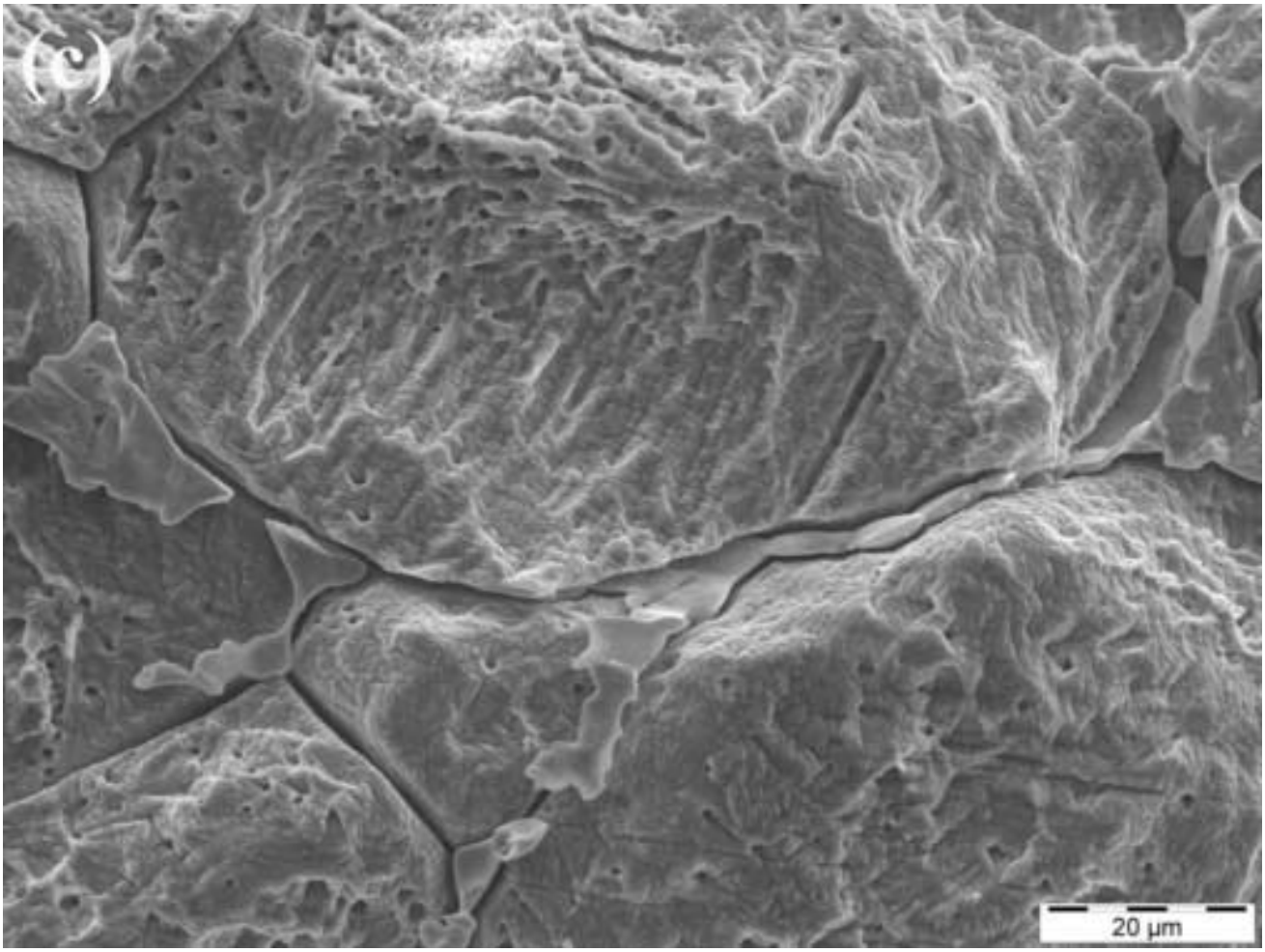

Figure 16d
Click here to download high resolution image